Czech Technical University in Prague
Faculty of Nuclear Sciences and Physical Engineering
Department of Physics

MASTER THESIS

The Development of Time-of-Flight Telescope for Elastic Recoil Detection Analysis

Jiří Bočan

Academic year: 2006/2007
Supervisor: RNDr. Anna Macková, Ph.D.
Consultant: RNDr. Vladimír Havránek, CSc.
Prague 2007

České vysoké učení technické v Praze
Fakulta jaderná a fyzikálně inženýrská

Katedra: fyziky Akademický rok: 2005/2006

ZADÁNÍ DIPLOMOVÉ PRÁCE

pro: **Jiří Bočan**

obor: Jaderné inženýrství

zaměření: Experimentální jaderná fyzika

Název práce: **The Development of Time of Flight Telescope for Elastic Recoil Detection Analysis**

(Vývoj Time of Flight (TOF) teleskopu pro měření jadernou analytickou metodou Elastic Recoil Detection Analysis (ERDA))

Osnova:

1. Přehled současného stavu jaderných analytických metod (TOF-ERDA, RBS, ERDA) na svazcích urychlených iontů.
2. Tandetron 4130MC jako zdroj urychlených iontů (možnosti urychlovače, popis iontových zdrojů, technické a provozní parametry).
3. Metoda TOF-ERDA
   - fyzikální principy
   - konstrukce TOF-ERDA trasy
   - zpracování TOF-ERDA spekter
   - kalibrace a testování trasy
4. Analýza konkrétních vzorků.

Diplomová práce bude vypracována v angličtině.
Součástí diplomové práce je její uložení na webovou stránku katedry fyziky ve formátu LATEX.

Doporučená literatura:

1. Backscattering Spectrometry, W. - K. Chu, J. W. Mayer and M. - A. Nicolet: Acad. Press, New York 1978.
2. Handbook of Modern Ion Beam Materials Analysis, Eds.: J. R. Tesmer, M. Nastasi, Contributing Editors J. Ch. Barbour, C. J. Maggiore, Material Research Society, Pittsburgh, Pennsylvania 1995.
3. Forward Recoil Spectrometry, Application to Hydrogen Determination in Solids, J. Tirira, Y. Serruys, P. Trocellier, Plenum Press, New York and London, 1996.

Jméno a pracoviště vedoucího práce:	RNDr. Anna Macková, Ph.D. ÚJF AV ČR, Řež
Konzultant:	RNDr. Vladimír Havránek, CSc. ÚJF AV ČR, Řež
Datum zadání diplomové práce:	21.10.2005
Termín odevzdání diplomové práce:	15.1.2007

J. Tolar
....
Vedoucí katedry

Havlíček
....
Děkan

V Praze, dne: 21.10.2005

ČESKÉ VYSOKÉ UČENÍ TECHNICKÉ V PRAZE
Fakulta jaderná a fyzikálně inženýrská
-1-

Název práce: **Vývoj Time-of-Flight (TOF) teleskopu pro měření jadernou analytickou metodou Elastic Recoil Detection Analysis (ERDA)**
Obor: Jaderné inženýrství
Druh práce: Diplomová práce
Vedoucí práce: RNDr. Anna Macková, Ph.D.
Ústav jaderné fyziky v.v.i., Akademie věd České republiky, Řež u Prahy
Konzultant: RNDr. Vladimír Havránek, Csc.
Ústav jaderné fyziky v.v.i., Akademie věd České republiky, Řež u Prahy

Abstrakt: Diplomová práce popisuje návrh a konstrukci Time-of-Flight (TOF) teleskopu pro jadernou analytickou metodu “Detekce pružně odražených atomů” (ERDA). TOF teleskop rozlišuje jednotlivé atomy vyražené ze zkoumaného vzorku bombardováním svazkem urychlených iontů pomocí současného měření jejich doby letu na definované dráze a jejich kinetické energie. Popsaná jednodušší verze teleskopu sestává z jednoho časového a jednoho energetického detektoru. Časový detektor, jehož koncept vychází z návrhů Bushe a Kreissiga, spolu s energetickým křemíkovým detektorem Ultra série firmy Ortec o aktivní ploše 300 mm^2 a tělesovém úhlu 1,697.10^{-4} sr definují dráhu pro měření doby letu o délce 740 mm. Elektronická trasa byla sestavena pro přímé měření doby letu (uspořádání start-stop). Teleskop byl testován pomocí analýzy tlustých vzorků skelného uhlíku a monokrystalu safíru, tenké vrstvy LiF na substrátu ze skelného uhlíku a tenké uhlíkové vrstvy na skleněném substrátu pomocí 15.4 MeV Cu iontů. Analýza spekter prokázala použitelnost představeného konceptu teleskopu pro analytickou metodu TOF-ERDA. Dosažené celkové hmotnostní rozlišení je přibližně 2 hmotnostní jednotky pro nejvíce zastoupené prvky. Praktické zkušenosti z výroby jednotlivých součástí teleskopu a z provozování teleskopu jsou důležitým podkladem pro výrobu druhého časového detektoru a pro zkompletování celého TOF teleskopu, které je plánováno na rok 2007. U plně vybaveného teleskopu je předpokládané řádové zlepšení hmotnostního rozlišení oproti současné předběžné verzi.

Klíčová slova: Analytické metody iontovými svazky, detekce pružně odražených atomů, TOF-ERDA, časový detektor.

Title: **The Development of Time-of-Flight Telescope for Elastic Recoil Detection Analysis**

Abstract: The design and construction of a Time-of-Flight (TOF) telescope for the nuclear analytical method Elastic Recoil Detection Analysis (ERDA) is presented in this master thesis. The TOF telescope distinguishes single ions arriving from the beam bombarded sample via simultaneous measurement of their flight time through a fixed distance and of their kinetic energy. The telescope preliminary version accommodates one time and one energy detectors. Time detector based on the concept of Bush and Kreissig, together with 300 mm^2 Ortec Ultra series silicon detector with the solid angle 1.697×10^{-4} sr define 740 mm TOF distance. The electronics line was designed for the direct time measurement (start-to-stop arrangement). The telescope testing was carried out with 15.4 MeV Cu ions and samples as bulk glassy carbon, bulk single-crystal sapphire, thin LiF layer on the glassy carbon substrate and thin carbon layer on the glass substrate. The spectra analysis proved usability of the telescope design for the TOF-ERDA analytical method. The total mass resolution is about 2 mass units for the most abundant elements. Practical experience with telescope components production and telescope operation gave important information for the production of the second time detector and completion of the whole TOF-ERDA system planned for the year 2007. The mass resolution of the fully equipped system will improve by an order of magnitude compared to the present version.

Key words: Ion beam analysis, elastic recoil detection, TOF-ERDA, time detector.

Preface

This master thesis is based on the experimental work carried out in the Laboratory of Nuclear Analytical Methods, Nuclear Physics Institute, Academy of Sciences, Řež, Czech Republic, in the year 2006. During this time, I had the unique opportunity to work with several persons to whom I would like to express my gratitude for their work, support and company.

My deepest gratitude goes to my supervisor Dr. Anna Macková for giving me the opportunity of working in the field of ion beam analytical methods, for her excellent guidance, support, encouragement and advice during this work.

I am indebted to Dr. Ulrich Kreissig from the Institute of Ion Beam Physics and Materials Research, Forschungszentrum Dresden-Rossendorf e.V., Germany, for sharing his experience of the TOF-ERDA method and the time detector design, for lending the fast timing amplifier, and for his valuable advice and help.

Particular thanks are due to Vladimír Semián who gave a great contribution to this work through physical construction of the time detector and equipment of the TOF telescope. I also thank him for his practical experience and support.

I am very grateful to Ing. Jiří Novotný for his useful help with electronics, Dr. Vladimír Havránek for his practical spectroscopy experience, and also to Dr. Václav Voseček for operating the Tandetron accelerator.

I am very thankful to Dr. Michal Šumbera for lending the fast oscilloscope and also to Ing. Jiří Vacík for providing me the α-source during testing of the device.

Special thanks go to Doc. Ing. Vladimír Hnatowicz for introducing me into the group of Nuclear Analytical Methods, for many inspirative ideas and also for attentive reading of the text.

I would like to thank the whole staff of the laboratory for the superb working atmosphere.

My very special thanks I owe to Prof. Ing. Zdeněk Janout from the Czech Technical University in Prague for his great support and help with finding a new direction in my experimental nuclear life.

Finally, I want to thank my parents, who have encouraged, supported, and believed in me all the time.

Řež, January 2007
J. B.

Contents

List of Figures

List of Tables

Introduction

Material research belongs to traditionally progressive fields of technology. Its products are used in the everyday life worldwide. However, due to the continuous miniaturization, the underlying structures are far beyond the analytical limits of the most of conventional methods. Nevertheless, nuclear analytical methods provide this possibility as they use probes of similar or much smaller dimensions (particles, radiation).

Nuclear Physics Institute AS CR (NPI) in Řež near Prague has the long tradition and experience with the nuclear analytical methods. Due to availability of particle accelerators and nuclear reactor whole spectrum of methods is provided. This master thesis was carried out in the Laboratory of Nuclear Analytical Methods where the charged-particle based methods pursue. The laboratory keeps at disposal two accelerators – a Van de Graaff accelerator, and from the end of the year 2005 also a new Tandetron accelerator. The Van de Graaff accelerator is used for nuclear analytical methods on the beams of protons and He ions, whereas the Tandetron is able to produce beams of almost any element of the periodic system which considerably extends its usability.

The topic of this thesis is devoted to development of the time-of-flight elastic recoil detection analysis (TOF-ERDA), concretely to development and construction of the time-of-flight (TOF) telescope (spectrometer). It is for the first time, when the TOF-ERDA method becomes available in the Czech Republic. TOF-ERDA is based on detection of ions which are recoiled from the examined sample due to bombardment by heavier beam ions. The TOF telescope measures the ion energy and time consumed by the ions to pass a given distance. On the basis of these information, single atoms are distinguished and details about the sample are obtained.

The main task of this work was the design of the optimal technical proposal of the TOF telescope which is determined by the performance of the Tandetron accelerator. The technical realization carried out at NPI Řež. The main goals of the work were design of the TOF-ERDA system, construction of its basic parts, tuning and calibration, and putting the whole system into operation.

The whole text contains five chapters. The first chapter presents a brief overview of the basic contemporary nuclear analytical methods. The following chapter describes the new Tandetron accelerator and its performance. The third chapter deals with theoretical principles the TOF-ERDA method is based on. The most extensive fourth chapter is concerned with the TOF telescope. It describes the telescope housing, design and construction of the time detector and also the telescope electronics. It is complemented with two appendices. The first appendix describes the basic operation principle of the time detector. The second appendix evaluates the time detector carbon foil influence on the detected ions. The results of testing of the present TOF-ERDA setup, obtained by measurement of real samples, are presented and discussed in the fifth chapter. The future development and usage of the system are presented in the conclusion.

Chapter 1

Present Status of Ion Beam Analytical Methods

Ion beam analytical (IBA) methods represent one of applied interdisciplinary branches of the contemporary physics whose importance increases with the developement of modern materials. Although some of them are known for more than 40 years, the progress in accelerator and detector technologies, and the continuous expansion of nuclear physics databases extend application of the IBA methods worldwide.

The charged particle IBA methods together with a neutron activation analysis as well as with many different branches of electron spectroscopy are used for analysis of thin films and layers of miscellaneous materials which cannot be investigated by conventional non-nuclear, chemical and physical analytical methods. These methods provide information about elemental composition of examined samples in the whole range of the periodic system regardless the elements of interest are bulk or trace. They further give information about elemental depth distribution or about surface properties of the investigated materials.

The IBA methods serve for investigation of materials coming from material research, industry, micro- and nanotechnology, electronics, optics and laser technology, chemical, biological and environmental investigation in general. The advantage of the IBA methods lies in minimal destruction of the sample, i.e. they leave the sample undamaged excepting the area of the beam impact. Furthermore, also the technical and methodical development of the IBA methods proceeds.

The IBA methods employ ion beams of various elements with kinetic energy ranging from hundreds of kiloelectronvolts (keV) up to tens of megaelectronvolts (MeV), beam currents are at most units of microamperes. For production of the probing ions different types of mostly electrostatic accelerators (single-ended Van de Graaf or Cockroft-Walton accelerator, Tandetron) are utilised. The information about investigated samples is provided via measurement of energy spectra of scattered ions, recoiled atoms or secondary radiation induced by ion bombardment.

One group of the IBA methods is based on the investigation of elastic collisions of projectiles with target atoms. Other group is based on inelastic processes (electronic excitation, nuclear reaction) whose products are detected. In the following sections the most important IBA methods are briefly described.

1.1 Rutherford Back-Scattering (RBS)

The analytical RBS method was used for the first time by Rubin *et al.* in 1957 [1]. It is based on detection of light projectiles which elastically scatter from heavier material atoms backwards with reference to the beam direction. Typical setup for RBS comprises an electrostatic accelerator which produces beams of projectiles (often protons and He ions) with kinetic energy of several units of MeV and beam currents of several hundreds of nanoamperes. The projectiles are guided via beamlines to a target chamber where they scatter from the sample tilted mostly perpendicularly to the beam. The remaining energy of the scattered projectiles is registered by a charged particle detector located in front of the sample at about 170° with reference to the beam direction. The resulting energy spectrum provides information about the sample.

Due to the kinematics of the elastic collision process, RBS may detect all elements of the periodic system which are heavier than the projectile ion with detection limits down to 10^{12} $\mathrm{at.cm^{-2}}$ [2]. It allows the depth profiling of target surface layers from units to tens of micrometers thick with a depth resolution of units of nanometers.

1.2 Elastic Recoil Detection Analysis (ERDA)

ERDA is a complementary analytical method to RBS. Its first successful application was carried out by L'Ecuyer *et al.* in 1976 [3]. It is based on the principle inverse to RBS. Heavy projectiles with energies up to several tens of MeV are used for depth profiling of light elements. The ion beam which collides with the sample, knocks out forwardly certain atoms. The experimental arrangement is similar with that of RBS but the particle detector measuring the energy of recoiled atoms is located forwards with reference to the beam direction. However, the acquisition and evaluation of energy spectra of recoiled atoms is complicated by the presence of elastically scattered primary ions.

To overcome this difficulty, several ERDA arrangements were constructed [4]. The scattered primary ions may simply be absorbed by a thin foil placed in front of the energy detector. Another possibility is simultaneous detection of both the scattered primary ions and recoiled atoms (possible in very thin samples) or usage of a ΔE-E telescope (semiconductor or gaseous detectors) to distinguish between the primary and recoiled ions. The TOF-ERDA method which was developed in 1983 by two independent groups [5, 6] becomes one of the very useful IBA methods in present. TOF-ERDA is the subject of this master thesis and is dealt in detail in the following chapters.

Generally, the ERDA method may detect all elements which are lighter than the projectile ion. It allows depth profiling up to depths of several micrometers with nanometer depth resolution. The detection limits are comparable to those o RBS [2].

1.3 Complementary IBA methods

The IBA methods complementary to RBS and ERDA are those based on the inelastic collision processes. A particle induced X-ray emission (PIXE) is based on an ionisation of atoms by MeV protons which results in emission of characteristic X-rays. The particle induced γ-ray emission (PIGE) makes use of γ-rays induced by interaction of MeV protons with atomic nuclei. Nuclear reaction analysis (NRA) denotes a broad spectrum of specific techniques based on nuclear reactions followed by emission of charged particle products. Some of them allow not only element determination but also depth profiling with various depth range and depth resolution. The overview of PIXE, PIGE and NRA characteristics is given in the Table 1.1.

Method	Detected particle	Process[a]	Reaction energy Q	Investigated elements	Probing depth range
PIXE	X-Rays	A(p,p'X)A	0	Na–U	(100–10,000) nm
PIGE	Nuclear reaction γ-rays	A(p,γ)B or A(p,p'γ)A	$\neq 0$	Li–Cu	(100–1,000) nm
NRA	Nuclear reaction light products	A(i,Cγ)B	$\neq 0$	H, Be, B, C, O, F, ...	(10–1,000) nm

---

[a] Notation: p – proton; i – projectile ion; A – target ion; B,C – nuclear reaction products; X – X-ray; γ – γ-quantum.

Table 1.1: The overview of the IBA methods based on the inelastic collision process. Ref. [2, 7].

Chapter 2

Tandetron 4130 MC

The Tandetron 4130 MC (see the Figure 2.1) is a compact, multipurpose electrostatic tandem accelerator system produced by High Voltage Engineering Europa B.V., The Netherlands (HVEE) [8]. It was installed at NPI in the November 2005 and from the beginning of the year 2006 the accelerator is fully operable.

The main purpose of the Tandetron is production of ion beams with energies in the range from 400 keV to 24 MeV of almost all elements of the periodic system for the trace element analysis by means of the nuclear analytical methods. It is the medium-current (MC) version with a terminal voltage varying from 200 kV to 3 MV. The device provides a high terminal voltage stability of at most ±300 V with a maximal ripple ±200 V [9]. Due to an effective suppression of the X-ray level, the accelerator can be operated in the typical laboratory conditions without a need of extra shielding.

Figure 2.1: The view of the Tandetron 4130 MC T-shaped tank. Ref. [8].

In the following sections, the principle of a tandem acceleration and operation principle of main parts of the Tandetron system, namely the ion sources and accelerator itself, are described.

2.1 Tandem acceleration principle

The tandem acceleration is based on a two-stage acceleration process (see the Figure 2.2). At the beginning, singly charged negative ions produced by one of two available ion sources enter a low-energy accelerator tube. Their initial kinetic energy at the low-energy tube entrance is adjusted by ion optics elements to be at most 80 keV. The negative ions are accelerated towards the positive high voltage (HV) terminal kept at the terminal voltage V_T one or two orders of magnitude higher. Ions gain the kinetic energy:

$$E_{LE} = eV_T\,. \tag{2.1}$$

Inside the HV terminal a gas stripper canal is located where ions lose their electrons due to a charge exchange during collisions with gas molecules, and become *n*-times positively charged. These positive ions are further accelerated towards the grounded high-energy accelerator tube base. This results in gaining an extra kinetic energy:

$$E_{HE} = neV_T\,. \tag{2.2}$$

When no kinetic energy losses through the whole accelerator system are taken into account, a total kinetic energy E_{TOT} of ions which reached the exit of the high-energy accelerator tube is:

$$E_{TOT} = (1+n)eV_T\,. \tag{2.3}$$

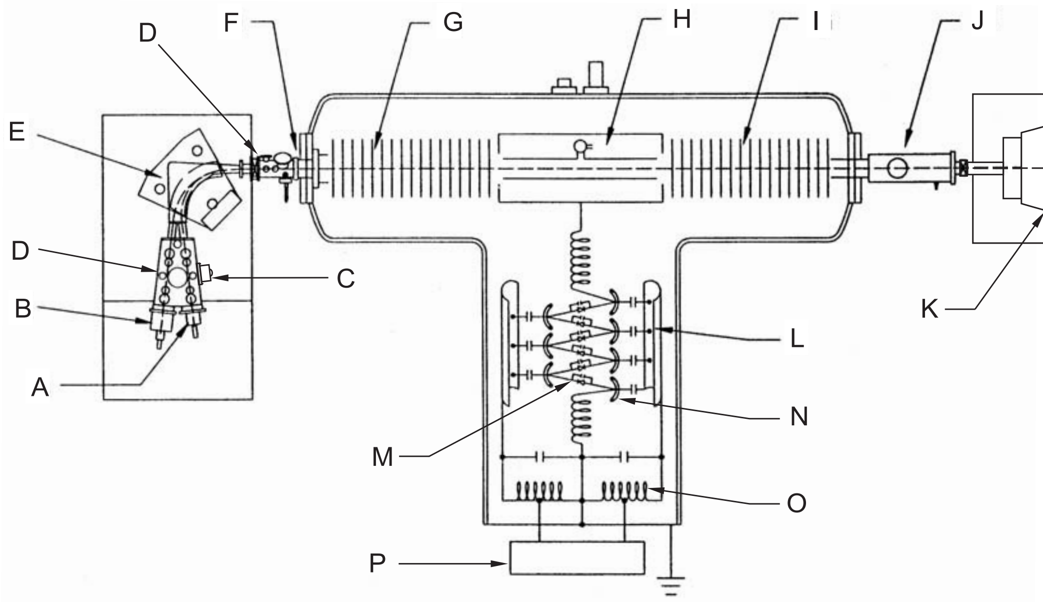

Figure 2.2: The scheme of the Tandetron 4130 MC. Labelled parts: Duoplasmatron ion source (A), Cs sputter ion source (B), Li charge exchange canal (C), Ion optics elements (D), 90° switching/analyzing magnet (E), Q-snout lens (F), Low-energy accelerator tube (G), HV terminal with gas stripper (H), High-energy accelerator tube (I), Electrostatic quadrupole triplet lens (J), High-energy switching/analyzing magnet (K), Rf driver electrode (L), Rectifier stack (M), Capacitor coupling ring (N), Rf oscillator coil (O), Rf driver (P). Ref. [9].

2.2 Dual-source injector system

On the low-energy side, the Tandetron is equipped with a dual-source injector system (DSIS) [9]. It comprises two ion sources – a duoplasmatron and a Cs sputter ion source, a Li charge-exchange canal, ion optics elements, a 90° switching/analyzing magnet, and a vacuum system.

The duoplasmatron ion source Model 358 [9] is the upgraded version of the Von Ardene's gas-fed ion source (see the Figure 2.3). It serves for obtaining of beams of H and He ions from appropriate gases. Although H^{-} ions are generated directly, due to a slight yield of He^{-} ions, duoplasmatron primarily produces He^{+} ions which are consequently converted to negative ones inside a gaseous Li charge exchange canal (see the Figure 2.4) located directly after the duoplasmatron source. The maximal output currents obtained from the duoplasmatron source are 4 eμA[1] for $^{1}\mathrm{H}^{+}$ beams and 0.7 eμA for $^{4}\mathrm{He}^{2+}$ beams (measured at maximum terminal voltage in a Faraday cup after a high-energy switching/analyzing magnet) [9].

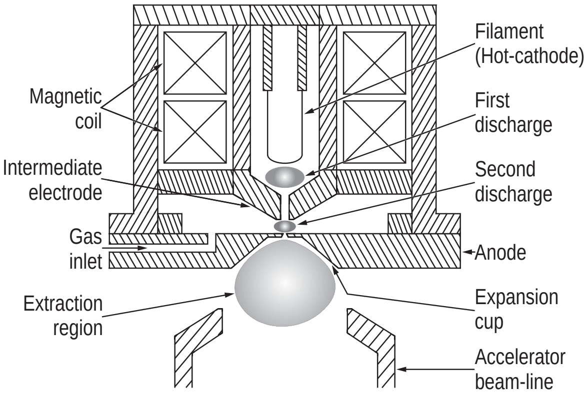

Figure 2.3: The scheme of the duoplasmatron ion source. Created on the basis of Ref. [10].

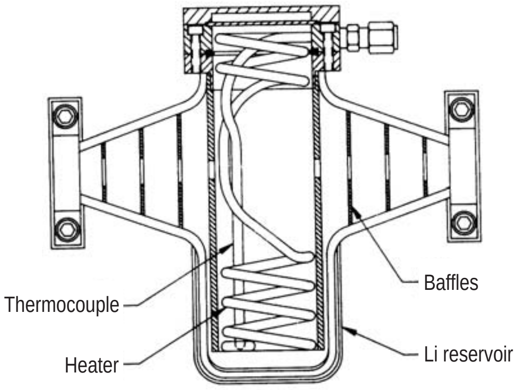

Figure 2.4: The scheme of the Li charge-exchange canal. Ref. [11].

The Cs sputter ion source Model 860A [9] is based on the Middleton's heavy-ion sputter source [12] (see the Figure 2.5). It produces beams of negative atomic or molecular ions of almost all elements of the periodic system from solid targets. The ion source operation is based on the sputtering of the target material by Cs^{+} ions which further act as electron donors for the sputtered atoms or ions to become negatively charged. HVEE guarantees output beam currents of 3 eμA for $^{58}\mathrm{Ni}^{3+}$ and $^{63}\mathrm{Cu}^{2+}$, 5 eμA for $^{11}\mathrm{B}^{3+}$, 10 eμA for $^{31}\mathrm{P}^{3+}$ and $^{197}\mathrm{Au}^{2+}$, and 20 eμA for $^{16}\mathrm{O}^{3+}$ and $^{28}\mathrm{Si}^{3+}$ (measured at maximum terminal voltage in a Faraday cup after a high-energy switching/analyzing magnet) [9].

Each ion source has its own power supply and beamline equipped with a set of ion optics elements which pre-shape and guide primary ion beams. The both beamlines enter the 90° switching/analyzing magnet (mass resolution $m/\Delta m \approx 80$) at different locations which guides the entering beam to a common exit location where a mass-defining aperture is placed.

The vacuum conditions in the whole DSIS are ensured by the turbo-molecular pump. Thanks to the design of the DSIS individual components, no HV protection cage, X-ray shielding or extra pre-accelerating elements are necessary.

---

[1] The current value given in eμA is independent of the ion charge state.

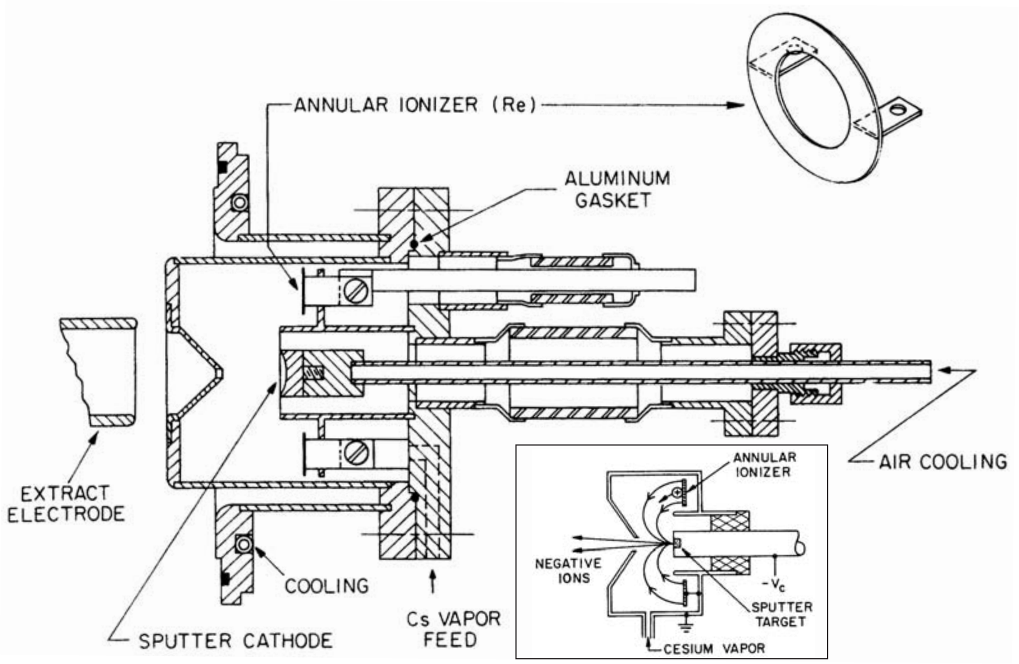

Figure 2.5: The scheme of the original Middleton's Cs sputter ion source. Ref. [13].

2.3 Accelerator system

The Tandetron accelerator system can be divided into three main sections – a pre-accelerating section located between the DSIS and the low-energy accelerator tube, an accelerating section presented by the Tandetron itself, and a post-accelerating section which provides ion beam transport to a proper beamline [9].

The pre-accelerating section consists of the mass-defining aperture, a beam profile monitor, a pneumatic retractable Faraday cup and a so-called Q-snout lens. The mass-defining slit together with the DSIS magnet lets through the desired ion species which will be further accelerated. The beam-profile monitor located directly after the mass-defining aperture maps a transversal beam profile and provides feedback for proper tuning of the DSIS components. The Faraday cup measures the beam current. The Q-snout lens is the metal cylinder device located in the accelerator low-energy tube entrance which matches completely the proper energy and spatial characteristics of the incoming ion beam through the next accelerating section. On the one hand, depending on the terminal HV value, it pre-accelerates ions from approximately 30 keV (ion sources extraction voltage) up to 80 keV. On the other hand, it ensures the optimal beam cross-section at the entrance to the terminal gas stripper which results in the high efficiency of the charge exchange process.

The accelerating section – the Tandetron accelerator – consists of a T-shaped pressure tank accommodating the low- and high-energy accelerator tubes, the terminal gas stripper, a HV power supply, and the vacuum system [9]. The low- and high-energy accelerator tubes are located within the cross bar of the pressure tank. They are made of glass insulators and Ti electrodes and are further equipped with the secondary electrons internal magnetic suppression system. Secondary electrons originate during collisions of the beam ions with beamline walls. Their suppresion results in the significant decrease of X-ray level during the accelerator operation. The terminal gas stripper connects both accelerator tubes and the HV power supply. It includes a large diameter stripper canal to ensure the high beam transmission, and a stripper gas inlet. The stripper gas – nitrogen – is continuously supplied into the stripper canal and immediately pumped out through the beamlines without recirculating. The beamline vacuum system guarantees pressures of the order of 10^{-5} Pa inside all beamlines.

The HV power supply is a gas-insulated all solid state power supply. It consists of three main parts – a HV multiplier with rectifier stack, a radiofrequency (rf) driver and a HV control and stabilization system. The HV multiplier and rectifier stack is provided by a parallel-fed Cockroft-Walton type power supply made of series of solid state HV rectifiers and capacitive coupling rings. The rf driver operates at resonance frequency of approximately 40 kHz and provides the power supply feeding via a capacitive couple by two semi-cylindrical electrodes surrounding the capacitor coupling rings. The HV multiplier and rectifier stack and the rf oscillator coils are located inside the pressure tank perpendicularly to the accelerator tubes. As an isolation gas SF_6 pressurized up to approximately 0.7 MPa is used. The rf driver itself is located in a separate air-insulated cabined beside the tank.

The whole pressure tank contains no moving parts inside which results in the high stability and low ripple of the generated HV. It is further equipped with the detectors of sparks and coronas. A spark detector is located on the top of the pressure tank near the HV terminal. The corona and other light occurrence is detected by a photomultiplier located nearby.

The post-accelerating section includes an electrostatic quadrupole triplet and a high-energy switching/analyzing magnet. The switching/analyzing magnet provides both the mass and charge state selection of incoming ions and their deflection to a proper beamline. It operates five exit ports at the deflection angles 0°, ±10°, and ±30°. The magnet and its vacuum chamber is water-cooled while its power supply is air-cooled.

Whole accelerator system is remotely controlled via fiber optics links by a computer which is located in the same laboratory as the accelerator. The control hardware and software monitor all the parameters several times per second and provide full control of the system.

Chapter 3

Theoretical Principles of TOF-ERDA Method

3.1 Introduction

The elastic-recoil detection analysis (ERDA) is one of the IBA methods suited for the non-destructive depth profiling of light elements in bulk samples. It is based on the detection of atoms which are knocked out from the sample by incoming heavy ions. When only kinetic energy is measured, ions of different elements coming from various depth within the sample can produce the same signal in the energy detector. In addition, also elastically scattered primary ions can be detected which further complicate the acquisition and evaluation of the energy spectra. To overcome this difficulty, several types of ERDA developed (see the Section 1.2). One of them is Time-of-Flight ERDA (TOF-ERDA).

The TOF-ERDA method is performed with the TOF telescope (see the Figure 3.1). It is mounted on a target chamber which houses a sample holder with a positioning system for setting a correct tilt angle of the sample with reference to the beam direction. The TOF telescope usually accommodates time start and stop detectors and an energy detector. The time detectors are located in a fixed mutual distance and measure the time spent by an incoming ion to fly through this distance. The energy detector placed behind measures ion kinetic energy. On the basis of both the ion flight time and energy (E), a 2D coincident E-TOF spectrum is collected which contains information about the sample composition and the elemental depth profiles.

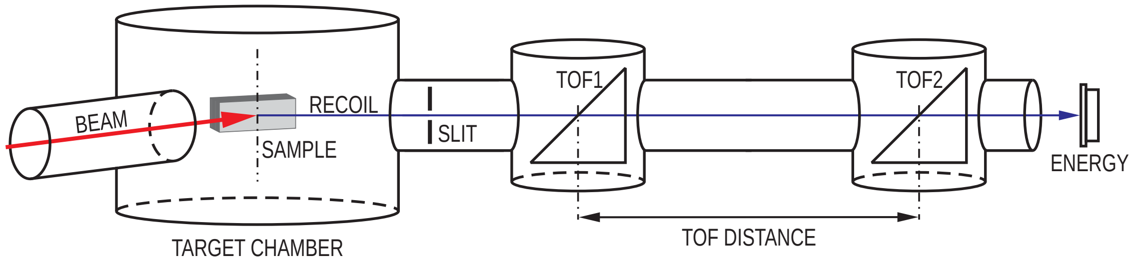

Figure 3.1: The principle scheme of TOF-ERDA.

Although the general principle of the TOF-ERDA method is quite simple, numerous factors affect both the acquisition and analysis of the E-TOF spectra and bring different kinds of errors and uncertainties which influence the TOF-ERDA performance (see the

Section 5.2). On the one hand, there are uncertainties connected with TOF-ERDA setup which are generally eliminable or their contributions are evaluable with a satisfactory precision:

- accurate geometry of beamlines;
- beam composition, transversal profile and energy stability during experiment;
- accurate sample position;
- accurate knowledge of the TOF distance;
- accurate knowledge of the ion flight direction through the TOF telescope;
- TOF telescope detectors time and energy resolutions;
- accurate tuning, performance and properties of data acquisition electronics, and so on.

On the other hand, much more significant uncertainties are connected with the sample itself whose contributions are not so easily determinable, which affect spectra analysis:

- sample material stopping power for used ions;
- scattering process cross-section;
- sample profile and surface morphology;
- straggling and multiple scattering of projectiles and recoils within the sample;
- sample degradation caused by heavy ion bombardment, and so forth.

All these effects contribute to the resulting TOF-ERDA spectra and necessarily have to be treated during the data analysis. In the following sections, the main principles and aspects of the ERDA and TOF-ERDA methods will be presented in more detail.

3.2 Kinematics

The ERDA method is based on the non-relativistic two-body elastic collision process schematically shown in the Figure 3.2. A heavier projectile ion of the mass M, atomic number Z and kinetic energy E_0 elastically scatters from a target atom (being initially at rest) of the mass $m < M$ and atomic number $z < Z$ under the scattering angle θ, having kinetic energy E_s. Consequently, the recoiled atom escapes under the recoil angle φ with kinetic energy E_r. Both the scattering and recoil angles are taken with reference to the initial projectile direction.

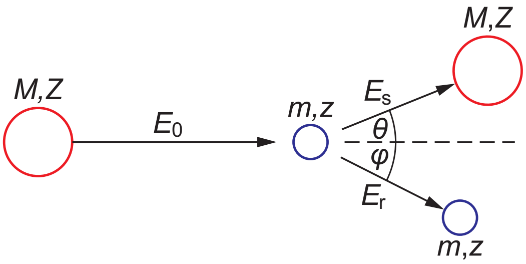

Figure 3.2: The elastic collision scheme in the laboratory frame. The heavier projectile of mass M scatters on the lighter target atom of mass $m < M$.

From the conservation laws for the total kinetic energy and total momentum, kinetic energies E_s and E_r equal:

$$E_s = \left(\frac{M \cos\theta + \sqrt{m^2 - M^2 \sin^2\theta}}{M+m} \right)^2 E_0 = KE_0, \tag{3.1}$$

$$E_r = \frac{4Mm\cos^2\varphi}{(M+m)^2} E_0 = (1-K)E_0 = K'E_0. \tag{3.2}$$

Here K and K' denote scattering and recoil kinematic factors, respectively. These factors completely determine kinetic energy distribution between the colliding atoms. The collision kinematics also gives possible ranges for scattering and recoil angle:

$$\theta \in \langle 0, \theta_{\max} \rangle,\, \theta_{\max} = \arcsin(m/M);\;\; \varphi \in \langle 0, \pi/2 \rangle.$$

Consequently, in the case when the heavier projectile collides with lighter target atom, the upper limit for the scattering angle, $\theta_{\max}$, exists. Considering the geometrical arrangement of the TOF telescope and the location of detectors in the target chamber, this fact can further be utilized for effective shielding of the detectors against the beam ions which are unwanted in the most ERDA types.

3.3 Cross-section

The cross-section expresses the probability with which the elastic scattering occurs. It is determined by the type of interaction potential $V(r)$. For ion energies usual for ERDA, the Coulomb potential is assumed:

$$V(r) = \frac{1}{4\pi\varepsilon_0} \frac{Zze^2}{r}, \tag{3.3}$$

where, in addition, r is a mutual distance of the colliding particle centres, e is the elementary charge, and ε_0 denotes the permitivity of vacuum. The resulting form of the classical Rutherford's differential cross-section formula for the elastic scattering process in the laboratory frame, which is expressed as a function of the recoil angle φ, equals:

$$\left(\frac{\mathrm{d}\sigma_r}{\mathrm{d}\Omega} \right)_{\mathrm{lab}} = \left(\frac{1}{4\pi\varepsilon_0} \right)^2 \left(\frac{Zze^2}{2E_0} \right)^2 \left(1 + \frac{M}{m} \right)^2 \frac{1}{\cos^3\varphi}. \tag{3.4}$$

3.4 Yield

Forward recoil yield Y is the measured signal which carries the information about the investigated sample. Omitting the sample properties (multi-elemental composition, surface properties) and all dispersion phenomena (straggling, multiple scattering) which complicate its expression, the yield is described by the following formula:

$$Y = qn_0 S\Omega_{\mathrm{det}} \left(\frac{\mathrm{d}\sigma_r}{\mathrm{d}\Omega} \right)_{\mathrm{lab}} \frac{x}{\sin\alpha} \tag{3.5}$$

where q denotes a projectile fluence, n_0 is a target atomic density, S represents the cross-section of the beam impacting on the sample surface, Ω_{det} is a detector solid angle, and $(\mathrm{d}\sigma_r/\mathrm{d}\Omega)_{\mathrm{lab}}$ is the differential cross-section given by equation (3.4). The last term expresses the length of the projectile path in an analyzed surface layer with thickness x, when the projectile approached the sample under the angle of incidence α; see the Figure 3.3.

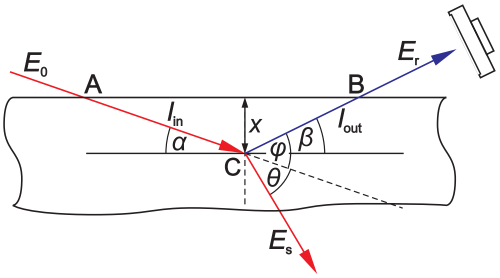

Figure 3.3: The principle of the sample depth profiling.

3.5 Ion energy losses

When ions pass through the sample, they lose their kinetic energy. An amount of the dissipated kinetic energy depends on both the ion and material characteristics: the projectile ion velocity V, mass M and nuclear charge Z, and the target atoms masses m_i, nuclear charges z_i (i denotes different elements) and stoichiometry. Ion slowing down is characterized either by a stopping power S defined as an amount of energy $\mathrm{d}E$ lost per unit path length $\mathrm{d}x$, or by a stopping cross-section ε defined as the stopping power per unit material density:

$$S \equiv \left(-\frac{\mathrm{d}E}{\mathrm{d}x}\right), [S] = \frac{\mathrm{eV}}{\mathrm{nm}}; \quad \varepsilon \equiv \frac{1}{\rho}\left(-\frac{\mathrm{d}E}{\mathrm{d}x}\right), [\varepsilon] = \frac{\mathrm{eV}}{10^{15}\,\mathrm{at.\,cm^{-2}}}.$$

The ion stopping includes various ion-target interactions. Depending on the ion kinetic energy, either nuclear or electronic stopping dominates. The nuclear stopping contributes mainly at ion energies below 200 keV, whereas the electronic stopping prevails at higher energies which are of TOF-ERDA interest.

Ions with energies below units of keV collide with material atoms as elastic spheres. At velocities much lower than the Bohr's electron velocity[1] v_{B}, ions tend to neutralize via target electrons capture. At energies one or two orders of magnitude higher, the screened Coulomb potential acts. In all these processes ions lose their energy in discrete collisions being deflected through large angles. In the MeV region, ions collide also with the target electrons which results in narrower paths within the target material. Ions then lose their energy continuously via electronic excitation, atomic ionization and δ-electron generation.

Within the ion velocity range $(0.1 - 2\pi Z^{2/3})v_{\mathrm{B}}$, electron stopping scales as $E^{1/2}$ (Lindhard-Scharff-Shiott theory) [14]. At the velocities of approximately $2\pi Z^{2/3}v_{\mathrm{B}}$, energy losses reach their maximum and begin decrease as Z^2E^{-1} (Anderson-Ziegler theory) [14]. This region together with the following relativistic and ultra-relativistic regions is described by Bethe-Bloch theory which is valid up to approximately 10 GeV/amu. For IBA applications, the following non-relativistic Bethe-Bloch formula suffices [15]:

$$S_{\mathrm{el}} = \left(\frac{1}{4\pi\varepsilon_0}\right)^2 \frac{4\pi Z^2 e^4 n_{\mathrm{e}}}{m_{\mathrm{e}}V^2} \ln\frac{2m_{\mathrm{e}}V^2}{\langle I\rangle} + \mathcal{K}. \tag{3.6}$$

Here, in addition, n_{e} represents a target electron density, and m_{e} is the electron mass. $\langle I\rangle$ denotes the mean ionization potential of the target atom which corrects for the quantum

---

[1] Bohr's electron velocity: $v_{\mathrm{B}} = e^2/(4\pi\varepsilon_0\hbar) = \alpha c \approx 2188\ \mathrm{km\ s^{-1}}$; here additionally $\hbar$, α and c are the reduced Planck constant, fine-structure constant and speed of light in vacuum, respectively.

mechanical energy levels available for transfer of energy to the target electrons. The last term $\mathcal{K}$ includes other corrections out of the IBA region of interest.

For evaluation of ion stopping in a sample made of a mixture or compound of different elements on the assumption that the interaction processes between projectiles and target atoms are independent, approximate Bragg-Kleeman's rule for the stopping cross-section holds [2]. For the compound or mixture $\mathrm{M}_\mu\mathrm{N}_\nu$ where M and N are two different elements and μ and ν are their stoichiometric coefficients normalized to unity, the total stopping cross-section $\varepsilon_{\mathrm{MN}}$ is given by:

$$\varepsilon_{\mathrm{MN}} = \mu\varepsilon_{\mathrm{M}} + \nu\varepsilon_{\mathrm{N}}, \tag{3.7}$$

where ε_{M} and ε_{N} are the stopping cross-sections within samples made of the pure elements M and N, respectively.

Example of electronic and nuclear stopping powers computed by the SRIM 2003 code [16] for ions with Z between 1 and 17 within the carbon foil which is utilized in the time detector (see the Subsection 4.2.2) is shown in the Figure 3.4. The TOF-ERDA energy region of interest is highlighted.

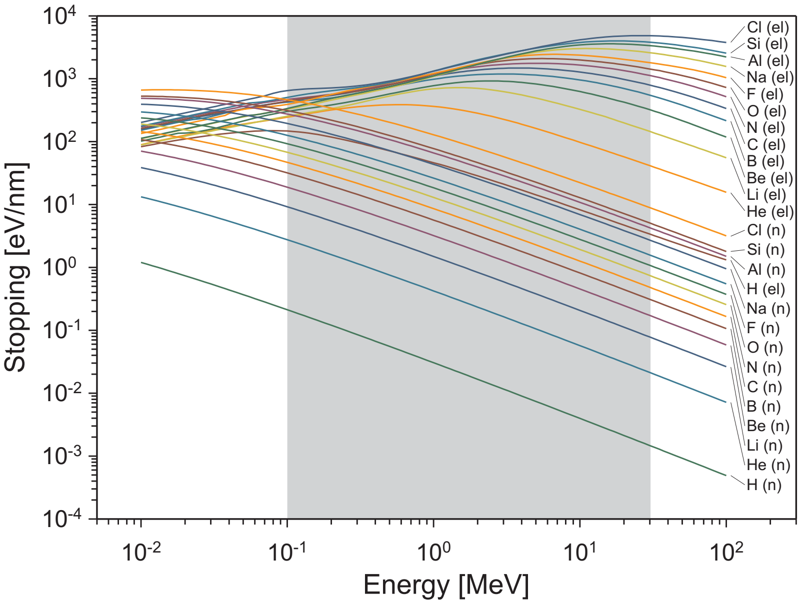

Figure 3.4: SRIM 2003 nuclear (n) and electronic (el) stopping powers of projectiles with Z between 1 and 17 within the time detector carbon foil (see the Subsection 4.2.2) in the energy range from 10 keV to 100 MeV. The grey region highlights energies of TOF-ERDA interest.

3.6 Energy straggling and multiple scattering

When ions penetrate the target medium, they undergo large number of collisions with target electrons and nuclei. As a consequence of the statistical nature of this process, the number of collisions varies for each ion. Originally monoenergetic and monodirectional beam projectiles lose different portion of energy and change their direction of motion. Both the resulting energy and directional distributions change with the distance travelled by projectiles within the target. The full width at half maximum (FWHM) of these distributions represents a measure of the energy and directional straggling.

Collisions of heavy ions with electrons entail mainly the energy straggling while the direction of motion remains almost the same. On the contrary, subsequent collisions with target nuclei, a so-called multiple scattering, lead to both the energy and directional straggling. The resulting distributions are roughly Gaussian. Especially for the energy straggling variance Ω_B^2 the approximate Bohr's formula, which is valid for target thickness $N\Delta R[\mathrm{at.\,cm^{-2}}] \gtrsim \dfrac{2\times10^{20}}{z}\left(\dfrac{E[\mathrm{MeV}]}{ZM[\mathrm{u}]}\right)^2$, holds [17]:

$$\Omega_B^2[\mathrm{MeV}^2] = 4\pi z Z^2 e^4 N\Delta R. \tag{3.8}$$

Here E, Z and M denote the projectile kinetic energy, atomic number and mass in the atomic mass units, and z, N, and ΔR are the target atomic number, atomic density and thickness, respectively. However, mainly in extreme cases of the very thin (Vavilov distribution [18]) or very thick (Tschalär distribution [19]) targets, the original Gaussian curve gains a tail which changes its shape.

Both the energy straggling [17] and multiple scattering [14, 20] are included in IBA software tools available for the data analysis. An example of SRIM 2003 [16] simulation of the energy and directional distributions for Cu projectiles with the kinetic energy 10 MeV after passing through Ni target of increasing thickness t is shown in Figures 3.5 and 3.6, respectively.

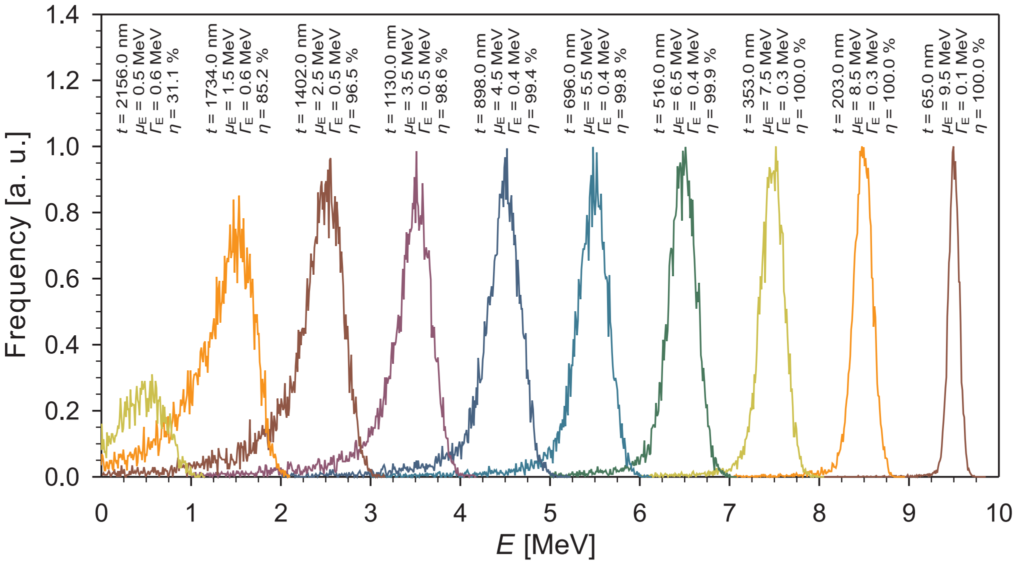

Figure 3.5: SRIM 2003 simulation of the energy straggling evolution. Cu projectiles pass through Ni target of different thickness t.

The directional deviation from the initial ion direction is treated as a radial distance r between the real point where the projectile escaped and the point where the projectile would escape maintaining its initial direction in reference to the known target thickness t (see the Figure B.1). Variables μ_E and Γ_E are the mean value and FWHM of the remaining energy distributions, and μ_r and Γ_r represent the mean value and FWHM of the directional distributions of Cu ions, respectively. η denotes a fraction of Cu ions which transmitted through the Ni target. Elements Cu and Ni were selected because of their high electron density, where the significant straggling is expected. The simulation input parameters are: Cu and Ni atomic and mass numbers: $Z(\mathrm{Cu}) = 29$, $A(\mathrm{Cu}) = 63.546$,

$Z(\mathrm{Ni}) = 28$, $A(\mathrm{Ni}) = 58.693$; Ni density: $\rho(\mathrm{Ni}) = 8.896\ \mathrm{g\,cm^{-3}}$; initial projectile kinetic energy: $E_{\mathrm{ini}} = 10.0$ MeV; initial number of projectiles per run: 10,000.

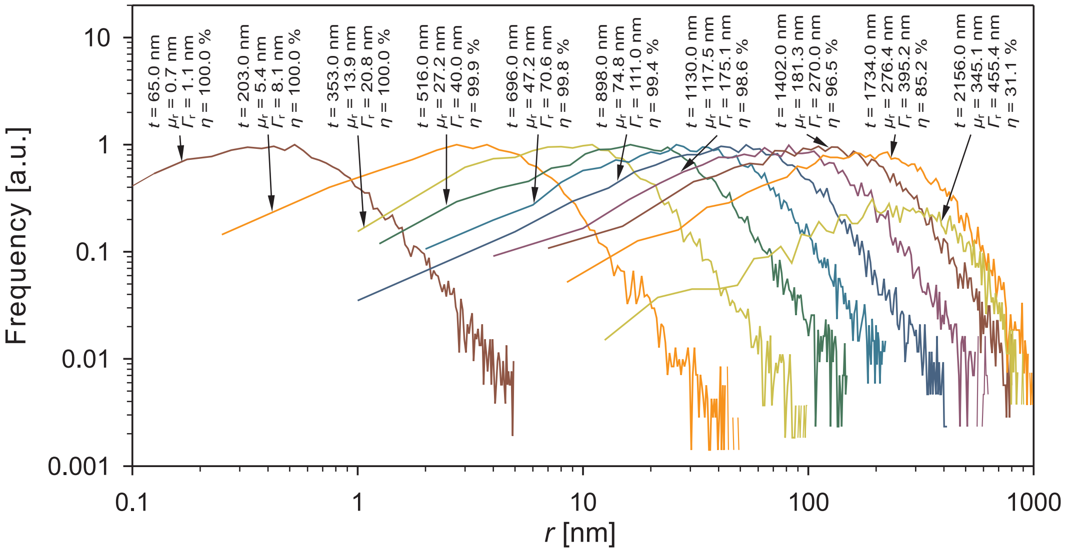

Figure 3.6: SRIM 2003 simulation of the directional straggling evolution. Cu projectiles pass through Ni target of different thickness t.

3.7 Depth profiling

During the projectile approach towards the collision centre inside the sample, and also during the recoil pass outwards, both ions lose a specific portion of energy. Its magnitude depends of the projectile-target combination, projectile kinetic energy and also on the depth under the sample surface where the collision centre lies; see the Figure 3.3.

On the basis of knowledge of both the projectile and recoil stopping power within the sample, the depth of the collision centre location can be determined from the measured recoil kinetic energy. This provides possibility of depth profiling of the sample atoms. Omitting all the dispersion phenomena, the simple relation for the depth x under the ideally flat surface in which the sample atom is located holds:

$$E_{\mathrm{det}} = K'[E_0 - S_{\mathrm{p}}(E_0)l_{\mathrm{in}}] - S_{\mathrm{r}}(E_{\mathrm{r}})l_{\mathrm{out}} - \mathcal{E}_{\mathrm{r}} \quad \Rightarrow \quad x = \frac{K'E_0 - E_{\mathrm{det}} - \mathcal{E}_{\mathrm{r}}}{\dfrac{K'S_{\mathrm{p}}(E_0)}{\sin\alpha} + \dfrac{S_{\mathrm{r}}(E_{\mathrm{r}})}{\sin\beta}} \tag{3.9}$$

Here E_0, $S_{\mathrm{p}}(E_0)$ and $l_{\mathrm{in}} = |AC| = x/\sin\alpha$ denote the initial projectile energy, stopping power and path-length between the surface point of incidence and collision centre within the target, respectively. K' and E_{r} are the kinematic factor and recoil kinetic energy given by the equation (3.2). $S_{\mathrm{r}}(E_{\mathrm{r}})$ and $l_{\mathrm{out}} = |BC| = x/\sin\beta$ represent the recoil stopping power and path-length between the collision centre and surface point of escape, respectively. A term $\mathcal{E}_{\mathrm{r}}$ includes additional energy losses within inactive or dead layers of detector system elements through which ions pass to be detected (e.g. time detector carbon foil, energy detector entrance window), which are also taken into account during the spectra analysis, see the Chapter 5.

3.8 Time-of-flight measurement

Measurement of the time of flight of ions through the TOF telescope serves for distinguishing the outgoing ions and recoiled atoms according to their mass. The time of flight t_{TOF} is given by the non-relativistic formula:

$$t_{\mathrm{TOF}} = l_{\mathrm{TOF}} \sqrt{\frac{m}{2E_{\mathrm{TOF}}}} \tag{3.10}$$

where l_{TOF} is the fixed TOF distance (see the Figure 3.1) along which the TOF is measured (distance between the time start and stop detectors) and m is the ion mass. E_{TOF} is the kinetic energy of the ion reduced by an extra energy loss within the first time detector carbon foil (see the Subsection 4.2.2 and Appendix B).

Chapter 4

Development and Construction of TOF telescope

This chapter describes the design and construction of the preliminary setup of the TOF telescope for the TOF-ERDA method practised at NPI. Because of the limited time available and no experience with construction and operation of the time detectors, it was decided to construct a simplified version of the TOF-ERDA device comprising only TOF start and energy detectors. In this configuration the energy detector substitutes the TOF stop detector. The TOF telescope is shown in the Figure 4.1. Its detailed scheme together with the telescope detectors location and mutual distances are depicted in the Figures 3.1 and 4.2.

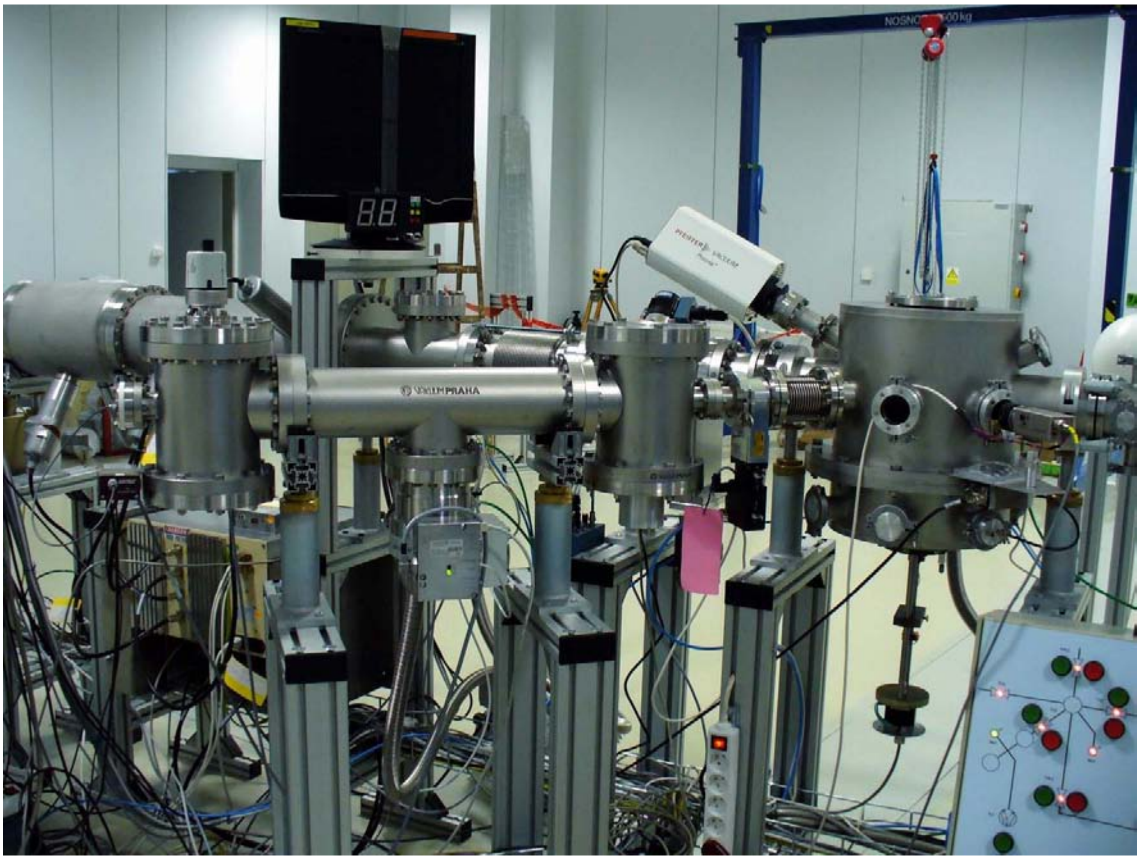

Figure 4.1: The view of the TOF-ERDA telescope and target chamber.

This chapter is devoted to the proposal, development and construction of the main parts which constitute the TOF telescope. Those are the TOF telescope housing together with the vacuum system, the time detector and its components, the energy detector, electronics and data acquisition system for TOF-ERDA.

4.1 TOF telescope housing

The TOF telescope housing was designed to fulfill the optimal geometrical conditions for the TOF-ERDA method. Its scheme is shown in the Figure 4.2 and the dimensions of its main parts are summarized in the Table 4.1. Stainless steel parts were produced by Vakuum Praha spol. s r.o., Prague, Czech Republic [21]. The whole telescope is mounted on the target chamber at 45° with reference to the beam direction (see the Figures 4.1 and 4.3). The connection is provided by a bellows and a vacuum valve. The target chamber is a part of the beamline located at the high-energy magnet exit port at −10° (see the Figure 2.2).

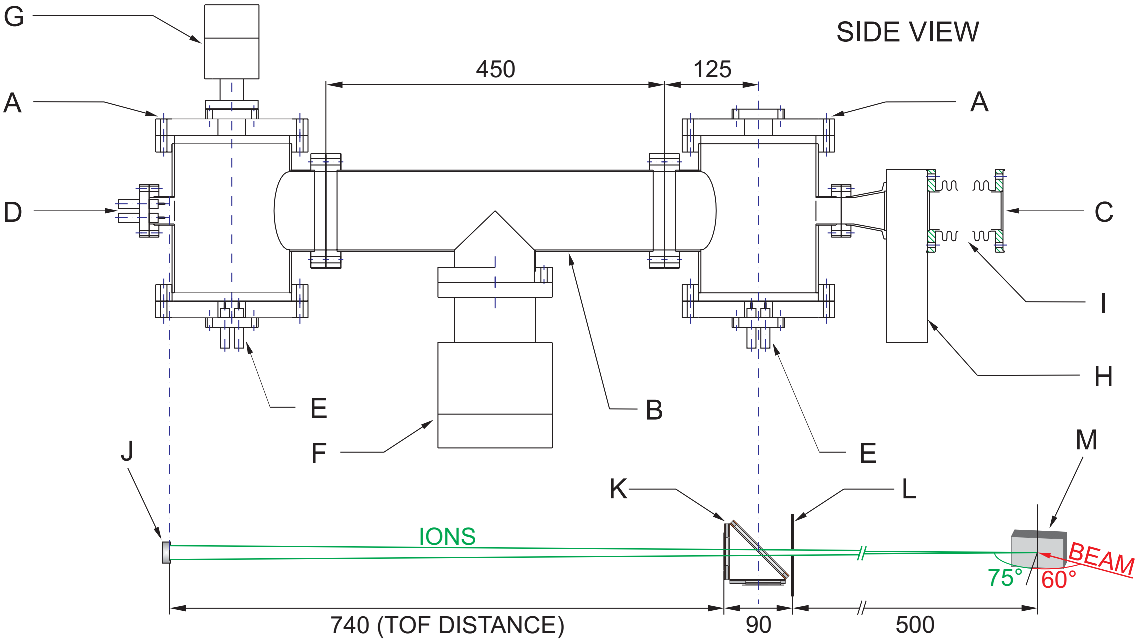

Figure 4.2: The present version of the TOF telescope. Labelled parts: Time detector chamber (A), Interconnecting tube (B), Telescope entrance from the target chamber (C), Back flange accommodating the energy detector (D), HV and signal cable feedthrough (E), Turbo-molecular pump (F), Vacuum gauge (G), Vacuum valve (H), Bellows (I), Energy detector (J), Time detector (K), Slit (L), Target (M). All dimensions in mm. Ref. [22].

	Time detector chamber	Interconnecting tube	Target chamber
Inner diameter	160 mm	100 mm	318 mm
Height/Length	220 mm	450 mm	360 mm
Upper/Lower flange	DN160 ISO CF	DN100 ISO CF	DN100 ISO CF
Input/Output flange	DN40 ISO CF/DN100 ISO CF	DN100 ISO CF	DN100 ISO CF

Table 4.1: The dimensions of the TOF telescope housing and target chamber. Ref. [22].

The telescope housing consists of three main parts – two chambers for time detectors and one interconnecting tube which can be replaced by another one of different length to vary the TOF distance. Bottom flanges of the time detector chambers are used for fixing the

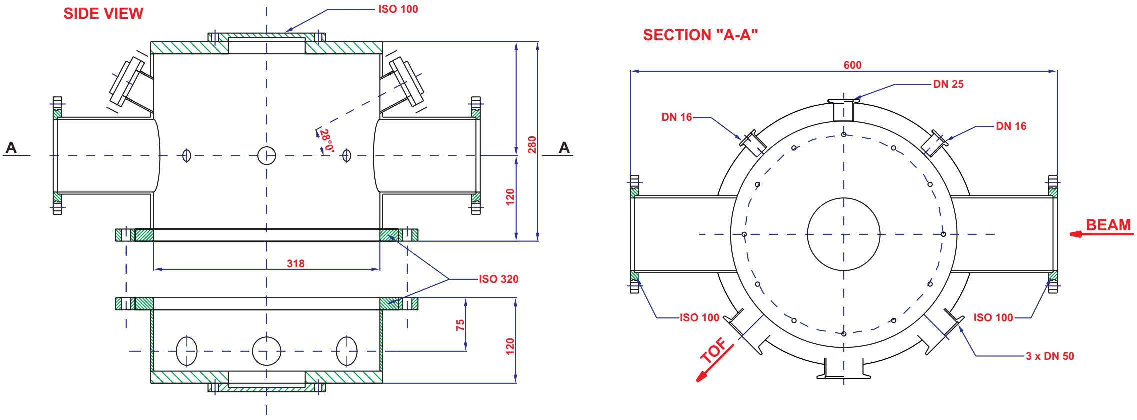

Figure 4.3: The design of the target chamber. Ref. [22].

time detectors inside the chambers. They also contain HV and signal cable feedthroughs. The upper flange of the TOF stop detector chamber accommodates a vacuum gauge. The back flange of this chamber is used for the energy detector fixation.

The TOF telescope is permanently evacuated and kept at the pressure of the order of 10^{-5} Pa. The permanent high vacuum is necessary because an electron-multiplying microchannel plate (MCP) detector utilized in the time detector needs a dust and humidity free environment. For this purpose, a turbo-molecular pump is used. It is mounted on the interconnecting tube bottom and is connected to a roughing rotary pump.

As the TOF telescope houses the time detector equipped with an ultra-thin carbon foil used as a secondary electron (SE) emitter (see below), a gas flow which occurs during pumping and venting of the telescope has to be reduced as much as possible. For this purpose, there is a pumping restriction made of an aluminium plate with a hole of a millimeter in diameter located between the interconnecting tube and the turbo-molecular pump. Further pumping restriction is provided by a manual valve mounted on the turbo-molecular pump output flange, which reduces the pumping speed of the turbo-molecular pump during initial pumping, and the gas flow between both pumps during venting the telescope.

The target chamber pressure is maintained below 5×10^{-4} Pa via two pumps mounted on the main beamline at $-10°$. Thus when the telescope and the target chamber is interconnected, it is assumed that no strong flow of the remaining gas evolves around the time detector, which could damage the carbon foil. In the present status, whole chamber has to be vented to change samples. To minimize the target chamber contamination and to save a time necessary for pumping and venting the target chamber, a load-lock system was designed and is now manufactured at Vakuum Praha [21], as well.

4.2 Time detector

During past decades of the successful utilization of the TOF-ERDA method worldwide, various types of time detectors were developed which provide different timing performance. Although these detectors differ in their geometrical arrangement, while the fundamental principle of operation remains unchanged, they are mostly based on the successful concept of Bush [23]. This detector type is utilized in many laboratories [24–28] but different designs are also used [29, 30]. The advantage of the Bush's design lies in its simple construction, dimension and shape variability and excellent timing performance.

Basic components of the time detector are the carbon foil, the SE transport system composed of electrostatic accelerating and mirror equipotential harps, and finally the MCP detector which further serves as a powerful SE signal multiplier.

The time detector design presented in this work derives from the Bush's original idea. Furthermore, it draws from the experience of Dr. U. Kreissig from the Institute of Ion Beam Physics and Materials Research at Forschungszentrum Dresden-Rossendorf e.V., Germany [31], where the TOF-ERDA method utilizing such type of the time detector is practised successfully for more than ten years. The view of the time detector constructed at NPI is shown in the Figure 4.4. In this section the time detector operation principle, and the design and construction of its parts are described.

4.2.1 Time detector operation principle

The time detector principle scheme is shown in the Figure 4.5a; its orientation agrees with that used in the TOF telescope. When ions have enough energy and a correct direction to leave the target chamber and enter the TOF telescope, after passing through the slit located inside of the first time detector chamber, right in front of the time detector, they enter the time detector interior. Passing the electrostatic mirror, a field-free region and an accelerating harp, ions traverse the carbon foil. This results in ionization of the carbon atoms along the ion path and in consequent emission of numerous SEs which eject from the surface layers of the foil in both the forward and backward directions with reference to the ion direction of motion.

Whilst the ions continue deeper into the TOF telescope, the backwardly emitted SEs are attracted and accelerated by the accelerating harp which is kept at more positive potential than the carbon foil. Gaining certain portion of the kinetic energy and significant momentum in the direction opposite to an electric field, electrons pass isochronously through the field-free region. Finally, they are bended by the electrostatic mirror tilted 45° to the accelerating wall, and directed towards the MCP detector. These SEs which reached the active area of the MCP are multiplied several orders of magnitude. The bunch of electrons exiting the MCP stack is collected by the MCP detector anode, and a negative time signal indicating the ion passage through the time detector occurs. This signal is further processed. The operation principle of the time detector electron optics together with relations describing the electron path within the mirror interior are summarized in the Appendix A.

4.2.2 Time detector design

As apparent in the Figures 4.4 and 4.5, the time detector is made from three function walls providing the SE generation, optics and detection – the front wall with the carbon foil and accelerating harp – the Figure 4.6, the back wall creating the electrostatic mirror for SEs – the Figure 4.7, and the bottom wall which fixes the MCP detector and also a part of a voltage divider serving for voltage supply of the time detector – the Figure 4.8. These walls are mounted together by two sidewalls. The sidewalls also create the field-free region and further serve for fixing and positioning the time detector inside the chamber. Finally, in front of the back wall, the aluminium plate with a circular hole is located.

Time detector construction materials were selected with respect to both the high voltage requirements (dielectric strength) and vacuum conditions (material degassing) inside the telescope. For the conductive equipotential walls 1.5 mm thick cuprextite was

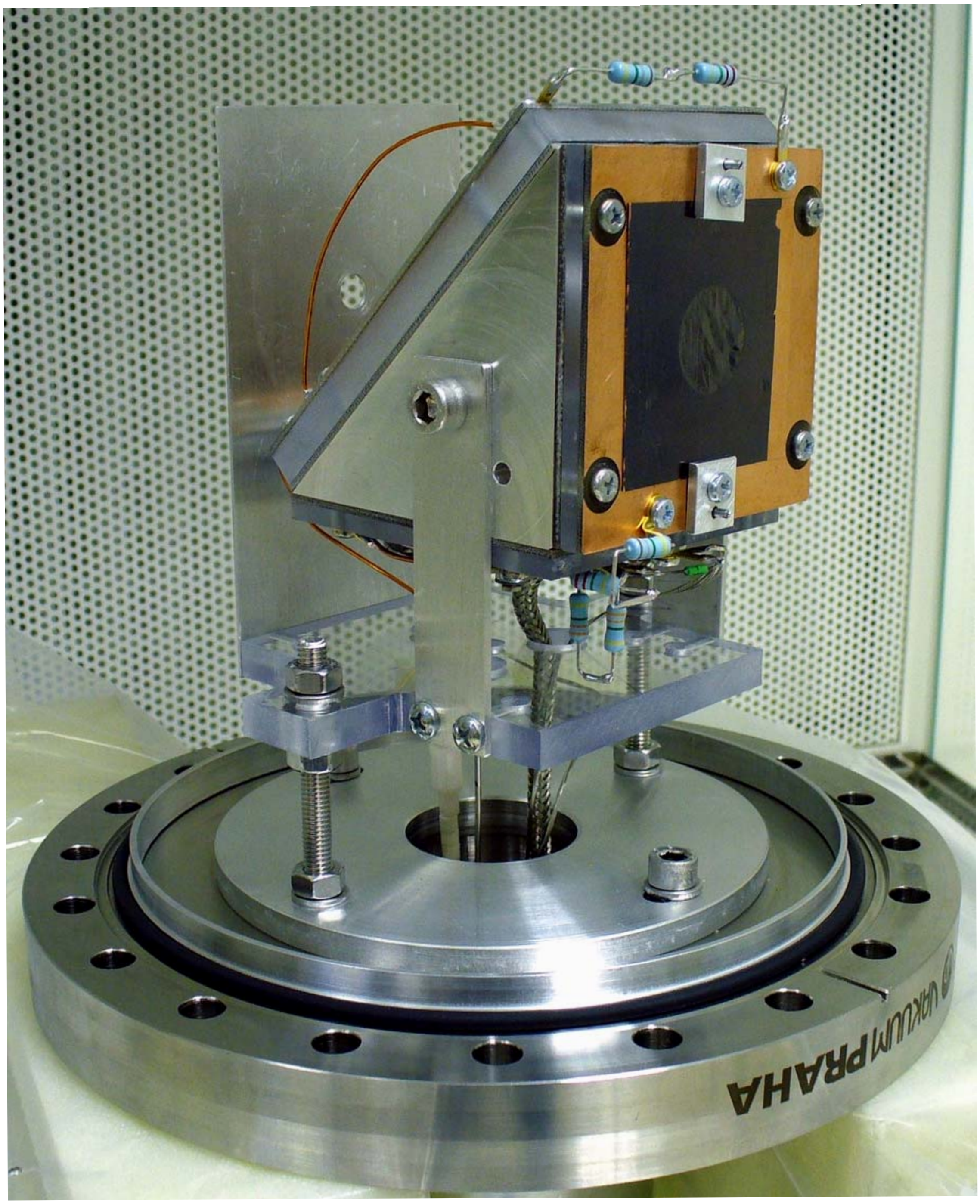

Figure 4.4: The view of the TOF-ERDA time detector.

chosen. The distance insets between the equipotential walls are made of polycarbonate 4 mm and 8 mm thick. The sidewalls are made of aluminium. Before the complete mounting together, every time detector component was cleaned in an ultrasound bath.

In the following text the basic time detector components – the carbon foil, equipotential harps, and MCP detector, followed by the detector function walls made of those parts are described in detail.

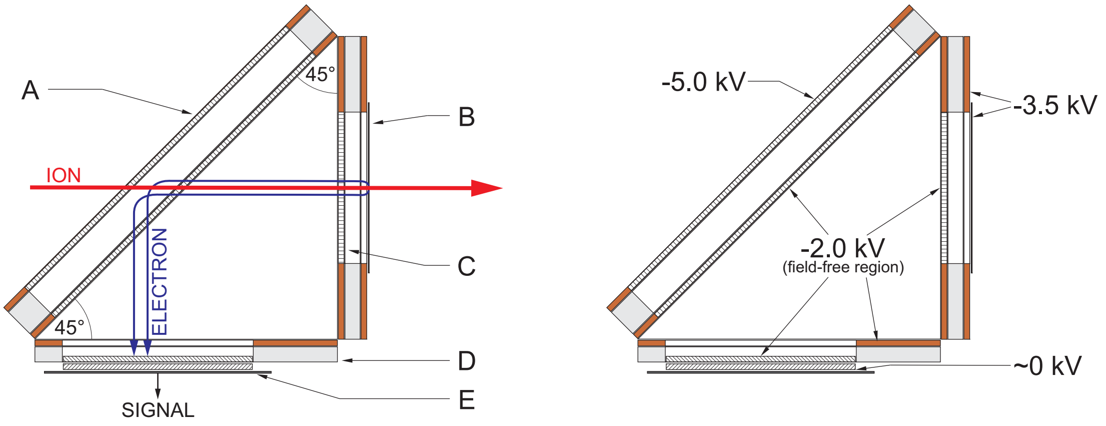

a) b)

Figure 4.5: a) The time detector operation principle scheme. b) The time detector potential distribution scheme (voltage values are approximate only). Labelled parts: Electrostatic mirror (A), Carbon foil (B), Accelerating harp (C), Base with MCP detector and voltage divider (D), MCP detector – two MCPs in the Chevron stack and anode (E).

Carbon foil

The time detector carbon foils are produced by ACF-Metals, Arizona, U.S.A [32]. The freestanding foils without supporting grids are made by a vacuum arc evaporation onto a glass substrate. The foils conventional size is 25 mm × 70 mm, their density is $(2.01 \pm 0.02)\,\mathrm{g\,cm^{-3}}$. The thickness of ordered foil pieces is $(20 \pm 2)\,\mu\mathrm{g\,cm^{-2}}$, the thickness of the one contemporarily used is $22\ \mu\mathrm{g\,cm^{-2}}$. The foils are composed of the natural isotopic carbon with minor impurities of H (3–5 at. %), O (1 at. %), Na (0.1 at. %), and traces of Fe, Mg, Al and Si (< 1 wgt. ppm each) which originate from the production process or from a starting material.

Carbon foils serve as the SE emitters. This feature and related measurement of a SE yield and a SE energy spectrum was studied with carbon foils of various thicknesses in detail in [33, 34]. It was shown that depending on the kinetic energy, charge state and atomic number of ions, from tens to hundreds of SEs with kinetic energies from tens of eV to several units of keV are ejected from the foil in both the forward and backward directions. Since the electrons come from surface layer only approximately 2 nm thick the proper thickness of the selected carbon foil is limited only by the energy loss of ions which pass through, but not by the SE yield magnitude. However, the used carbon foils are still satisfactory.

The total yield of forward and backward SEs is of the same order of magnitude but the low-energy (≤ 200 eV) forward SE yield is a factor 2 higher than the backward one. The high-energy (> 200 eV) forward SE yield is a factor $(2-5)$ lower than the low-energy forward yield, but a factor 10 greater than the backward high-energy SE yield [33]. In contrast to the backward yield, the forward yield depends on the ion energy [35]. The forward SEs are thus less favorable for timing due to the presence of both the low- and high-energy components which may worsen the time resolution of the time detector. The high-energy electrons are also less effectively bended by the electrostatic mirror and more easily escape the time detector. For that reason the backward SEs are exclusively used in the present arrangement.

Since the carbon foil has thickness approximately 100 nm, ions lose a nonnegligible

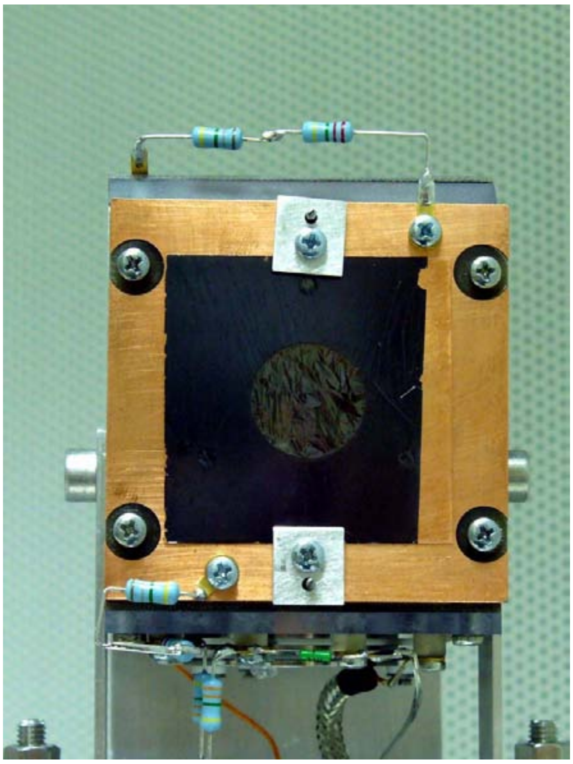

Figure 4.6: The time detector front wall.

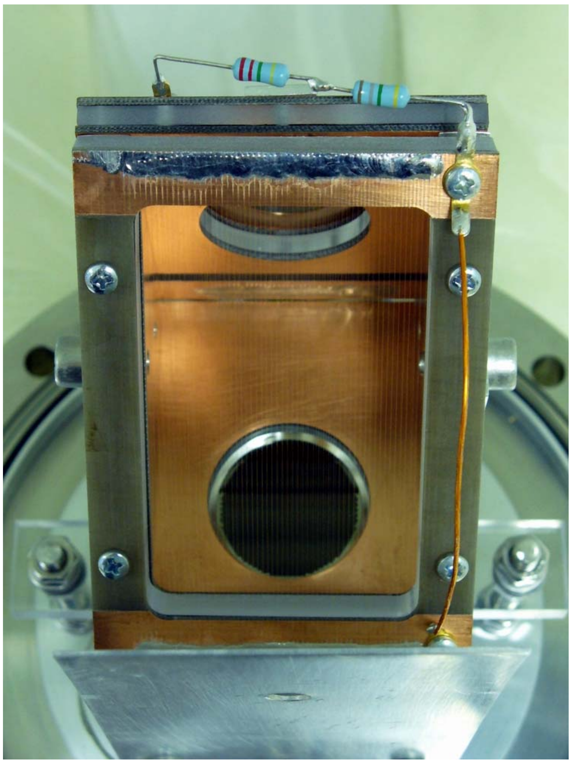

Figure 4.7: The time detector back wall.

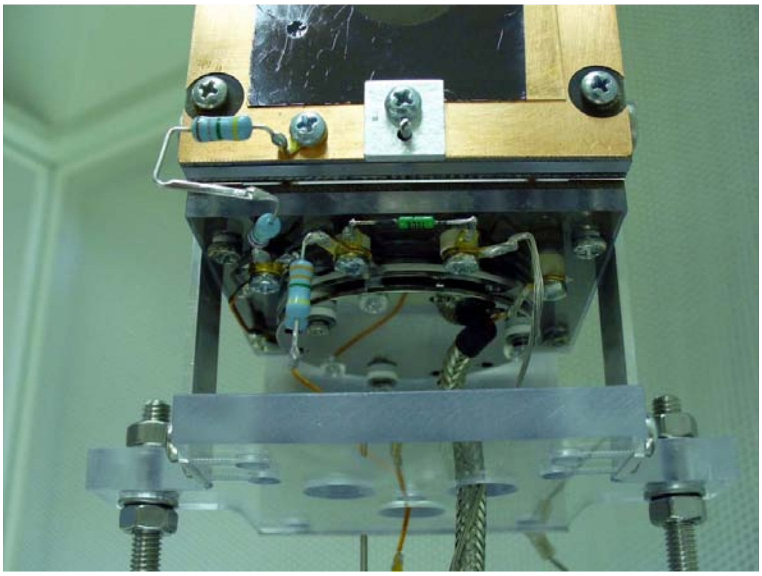

Figure 4.8: The time detector bottom wall.

portion of their kinetic energy within it. Furthermore, the foil increases the energy and directional straggling of ions and influences adversely the total resolution and performance of the TOF telescope. The energy and directional straggling in the carbon foil were studied with a help of SRIM 2003 code [16]. The results are summarized in detail in the Appendix B.

The carbon foil is fixed on a 0.2 mm thick copper frame 50 mm × 50 mm with a central hole 20 mm in diameter (see the Figures 4.6 and 4.13). The frame is mounted on the conductive side of the cuprextite plate and forms together with the cuprextite the outer potential face of the time detector front wall. To carry the thin carbon foil onto the copper frame, a so called floating method described in [32] was used. A piece of the carbon foil of dimensions 25 mm × 35 mm was scraped around with a razor blade on the glass substrate without any touching the foil. The glass substrate with the foil was placed in a dish and fixed at about 45° to the horizontal. To avoid possible problems during foil manipulation, the ultrasound cleaned planar burr-free copper frame was lied on the dish bottom, too.

The dish was carefully filled with a distilled water up to the height of the upper foil edge. As the water level raised, the foil gradually separated from the substrate, and finally, it completely floated on the water surface. Then the frame was picked up with a forceps, oriented almost 90° to the water surface, approached to the foil and aligned with one straight edge of the foil. The frame was slowly lifted up until the foil completely draped on it. The excess of water was blot off from the frame, and the frame with the foil were left to dry. During whole process no adhesives were necessary; the foil is fixed on the frame due to a self-adhesion. For this purpose, the appropriate copper frame surface was gently sanded to create a hydrophilic surface.

Wire harps

The time detector accommodates three wire harps (see the Figures 4.13 and 4.14). They are designed with an intent to create effective and sufficiently homogeneous equipotential walls, and also to be as transparent as possible to minimally hinder the ions and electrons which pass through them.

For the harp production a 20 μm gold-plated tungsten wire produced by Goodfellow Cambridge Limited, England [36], was selected. The wire is made of 99.95 % pure tungsten. The gold plating is provided by 99.99 % pure gold of approximately 4 % by weight with reference to the tungsten core, which means approximately 200 nm thick gold cover layer. This type of wire was selected due to an extreme strength of tungsten which results in possibility of utilizing the wire so thin. The gold cover layer ensures absence of burrs which can occur during the wire fabrication and which can cause problems when the HV is applied to them.

The harp wires are stretched over the conductive side of the cuprextite frame and are fixed by a tin solder towards the frame. The distance between two neighbouring wires is 0.9 mm regularly along all frames. The active area of the accelerating harp contains 36 wires of the total length 895 mm. The active area of each mirror harp is composed of 55 wires of the total length 4343 mm. The geometrical transparency of the harps due to wires is approximately 97.73 % for the accelerating harp, and approximately 97.75 % for the mirror harp.

Micro-Channel Plate Detector

For the SE signal multiplication and following collection, long life micro-channel plates pre-mounted together with an anode were selected (see the Figure 4.9). This MCP detector is produced by Burle Industries, Inc., Philadelphia, U.S.A. [37], which also tested its performance.

The detection quality MCPs are arranged in a high gain Chevron configuration (see the Figure 4.10). They have a quality diameter 25 mm with the active area (fraction of the total channel cross-section area with reference to the active area of MCP) about 58 %. The

MCP channels have a diameter 10 μm with 12 μm centre-to-centre pitch, their aspect ratio (channel length-to-diameter ratio) equals 60:1. To further increase the gain, the channels are tilted 8° with reference to a surface normal. The total Chevron MCP detector gain for electrons is approximately 2.6×10^7 at 2200 V applied to the detector. A dark count rate is 0.8 $\text{s}^{-1}\text{cm}^{-2}$. The detector total resistance is approximately 260 MΩ [37].

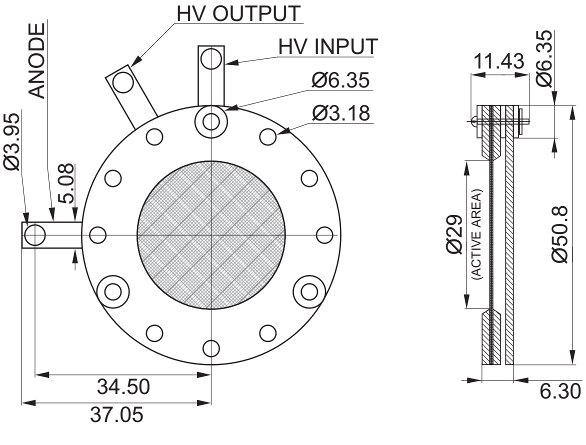

a) b)

Figure 4.9: The design of the pre-mounted MCP detector. a) The bottom view. The first MCP is located in the centre, the support conductive ring defines the MCP active area. b) The side view with the Chevron MCP located on the left with reference to the anode. All dimensions in mm. Ref. [37].

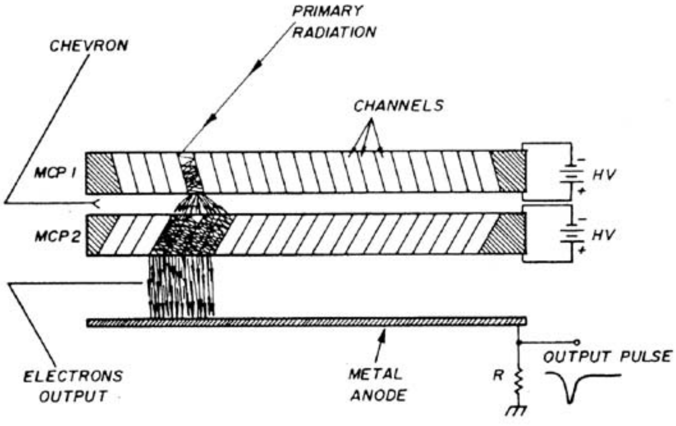

Figure 4.10: The operation scheme of the MCP Chevron assembly. Typical inter-plate distance is approximately 100 μm. Ref. [38].

The MCPs are produced from solid glass fibers [38]. The fibers are made of two components – a soluble core, and a lead glass cladding non-soluble in a core glass etchant which forms the MCP matrix structure. Single fibers when drawn are packed together to a hexagonal array. This array is drawn again to form a multi-fiber. Further drawing is done with many multi-fibers to reach the required diameter of the MCP plate. After that, the final multi-fiber is sliced at a certain angle with reference to the MCP channel axis. Surfaces of the resulting wafers are mechanically and chemically modified. The soluble cores are dissolved by the etchant, and several further chemical treatments of the MCP plate and inner surfaces of the channels follow to produce the complete MCP.

The MCP operation is based on a process when the incoming electron produces SEs by hitting the channel wall (see the Figure 4.11b). Due to a voltage applied to the both MCP surfaces, such electrons are accelerated when approaching towards the opposite wall and produce further SEs. When all electrons escape the single MCP, the reached gain G is of the order 10^4. The single MCP gain can be further expressed in the following way [38]:

$$G = \delta^n \approx \left(0.1\frac{V}{2\alpha\sqrt{\epsilon}}\right)^{4\epsilon\alpha^2/V} \tag{4.1}$$

where δ represents a number of the first generation SEs and n a number of the SE generations. V denotes the applied voltage to the MCP, ϵ an initial primary electron energy, and α is the channel aspect ratio.

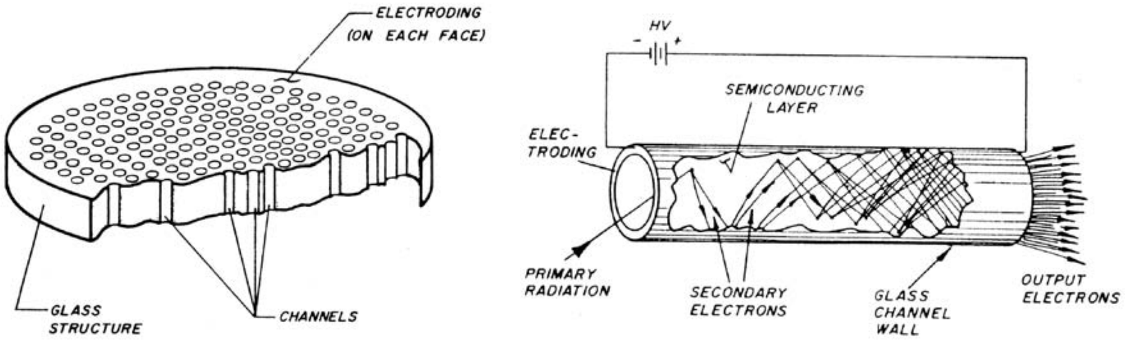

a) b)

Figure 4.11: a) The MCP scheme. b) Operation principle of single MCP channel. Ref. [38].

Voltage divider

To supply the MCP and the electron optics elements, various potentials are necessary. During the HV supply design, different requirements were taken into account:

- HV supply maximal negative voltage available;
- HV dielectric strength of the time detector construction materials within the detector chamber environment;
- keeping number of wires and connectors as low as possible;
- vacuum feedthrough limitations;
- optimal electron optics conditions;
- optimal voltage for MCP operation;
- maximal allowed applicable voltage to the Chevron MCP;
- power and thermal load of both the HV components and time detector parts because of minimal vacuum heat sink;
- spatial limitations given by both the detector and chamber dimensions.

For feeding the time detector, one channel of a 5 kV dual stabilized HV supply is used. To ensure the HV dielectric strength, minimal distance between the wires and components at different potentials was kept as 1 mm per kV. Furthermore, vacuum significantly increases the dielectric strength of all materials. In total, only three main wires are necessary – HV and ground wire, and MCP anode signal wire. The electron optics elements are designed in a way that the mirror voltage is twice the accelerating voltage, with minimal accelerating voltage between (1.0–1.5) kV [31], see also the Figure 4.5b.

The maximal voltage per Chevron MCP is 2.4 kV in total, i.e. 1.2 kV per one MCP [37]. During the first measurement with the MCP detector it was observed, that the MCP detector becomes active from approximately 950 V per one MCP. The optimal operation voltage lies between (1.0–1.1) kV per MCP. It is recommended by the producer to operate the MCPs at voltages as low as possible with respect to the detection performance to extend their lifetime [37]. Further request concerning the HV supply is not to exceed the maximal allowed voltage applied to the Chevron MCP when the maximal voltage at the HV supply is set. This is treated by the design of the detector HV supply. Not to exceed the power and thermal load, special HV components are selected.

The easiest way how to comply all the requirements including the possible solutions mentioned above is the series voltage divider. For its construction HV high-ohmic resistors produced by RS Components Ltd. [39] were selected which sustain voltages up to 3.5 kV per resistor and power load up to 0.5 W per resistor. The voltage divider electrical scheme is shown in the Figure 4.12. The divider parts are apparent in the Figures 4.4, and 4.6–4.8. The resistances R_1, R_2 and R_3 are created from two series resistors, thus 7 resistors were used in total. During designing the voltage divider, also the MCP detector resistance, which is connected in parallel with R_3, was taken into account.

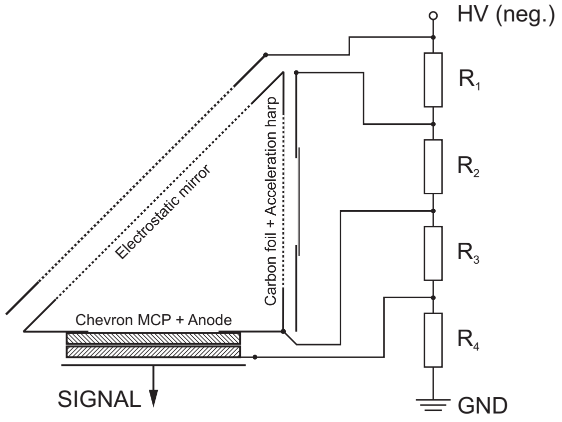

HV= −5.0 kV (max.)

$R_1 = R_2 = (2.2 + 1.8)\ \mathrm{M\Omega} = 4.0\ \mathrm{M\Omega}$
$R_3 = 2 \times 3.3\ \mathrm{M\Omega} = 6.6\ \mathrm{M\Omega}$
$R_4 = 100.0\ \mathrm{k\Omega}$
$R_{\mathrm{TOT}} = 14.7\ \mathrm{M\Omega}$

Figure 4.12: The electrical scheme of the time detector voltage divider. The correspondence between the resistance values given by producer and those measured is better than 1 %.

The voltage divider, carbon foil, and the MCP detector heretofore stored in vacuum, were mounted together to build the time detector. The complete time detector (see the Figure 4.4), which was fixed to a support structure constructed on the time detector bottom flange, was mounted on the TOF telescope chamber. The completely equipped telescope was evacuated for several days to ensure the time detector construction materials degassing. After that period, the MCP detector was prepared for operation via a special start-up process of slow gradual increase of the applied HV [37]. During this warm-up procedure also MCPs degassed partly due to heating caused by their operation. It was apparent that with increasing voltage applied to the MCP detector, the pressure inside the TOF telescope increased, as well, and the total divider current decreased because of the parallelly connected MCP resistance.

After more than one month of time detector operation, the voltage divider current which is measured directly by the HV supply, remains almost constant in the long term. However, the divider current and thus the total resistance change in the order of tenths of percent during the warming up period compared to the values at the end of time detector operation. This effect can be caused by the changes of the MCP properties with its temperature. Also the dark current caused by thermoemitted electrons from the channels walls contributes. Finally, impurities which remained inside the telescope housing after interconnecting of the telescope with target chamber could probably get stuck on the MCPs during the time when the MCP detector is out of operation. However, this deviation seems to be natural without a negative impact on the MCP detector operation.

Time detector front wall

The front wall accommodates the carbon foil and the accelerating harp (see the Figures 4.6 and 4.13). It is made from two 1.5 mm thick cuprextite plates and 4 mm thick polycarbonate distance inset. Both cuprextite plates are oriented in a way that the conductive sides face outwards the front wall. The wall includes a central hole 32 mm in diameter for letting the ions through. It further fixes a part of the voltage divider. The carbon foil frame is mounted on the outer conductive cuprextite side. On an inner conductive cuprextite side the wire harp is stretched.

The front wall provides production of backward SEs. The electrons originate mostly with energy of several tens of eV. They are attracted towards the accelerating harp plane by the electric potential gradient between the walls. As a consequence, these electrons gain significant momentum in the direction opposite to the electric field and all electrons produced by one ion move along isochronous trajectories through the inner field-free region.

Time detector back wall

The back wall creates the electrostatic mirror for deflection of SEs arriving from the time detector front wall (see the Figures 4.7 and 4.14). It composes from two wire harps of the type mentioned above stretched on 1.5 mm thick cuprextite. The polycarbonate distance inset is 8 mm thick. The mirror wall is tilted 45° with respect to the front wall.

Electrons which reach the mirror region move along parabolic trajectories within the mirror interior. When entering back to the time detector field-free region, they move perpendicularly to their initial direction of motion being directed towards the MCP detector.

Time detector bottom wall

The bottom wall of the time detector is made of 1.5 mm thick cuprextite and 4 mm thick polycarbonate (see the Figures 4.8 and 4.15). The conductive cuprextite side is oriented inwards the time detector. Together with the accelerating harp, inner electrostatic mirror harp and both sidewalls it creates the field-free region. The polycarbonate plate serves for fixing the MCP detector and the greater part of the voltage divider.

Entrance slit

In front of the time detector (see the Figures 4.2 and 4.4), the aluminium plate with the circular slit of the diameter 7.35 mm is located. Such plate is fixed to the time detector support structure. This slit limits the rate of the incoming ions into the TOF telescope and also partly shields the time detector body. Its solid angle is almost the same as that of the energy detector, i.e. 1.697×10^{-4} sr with respect to the sample position.

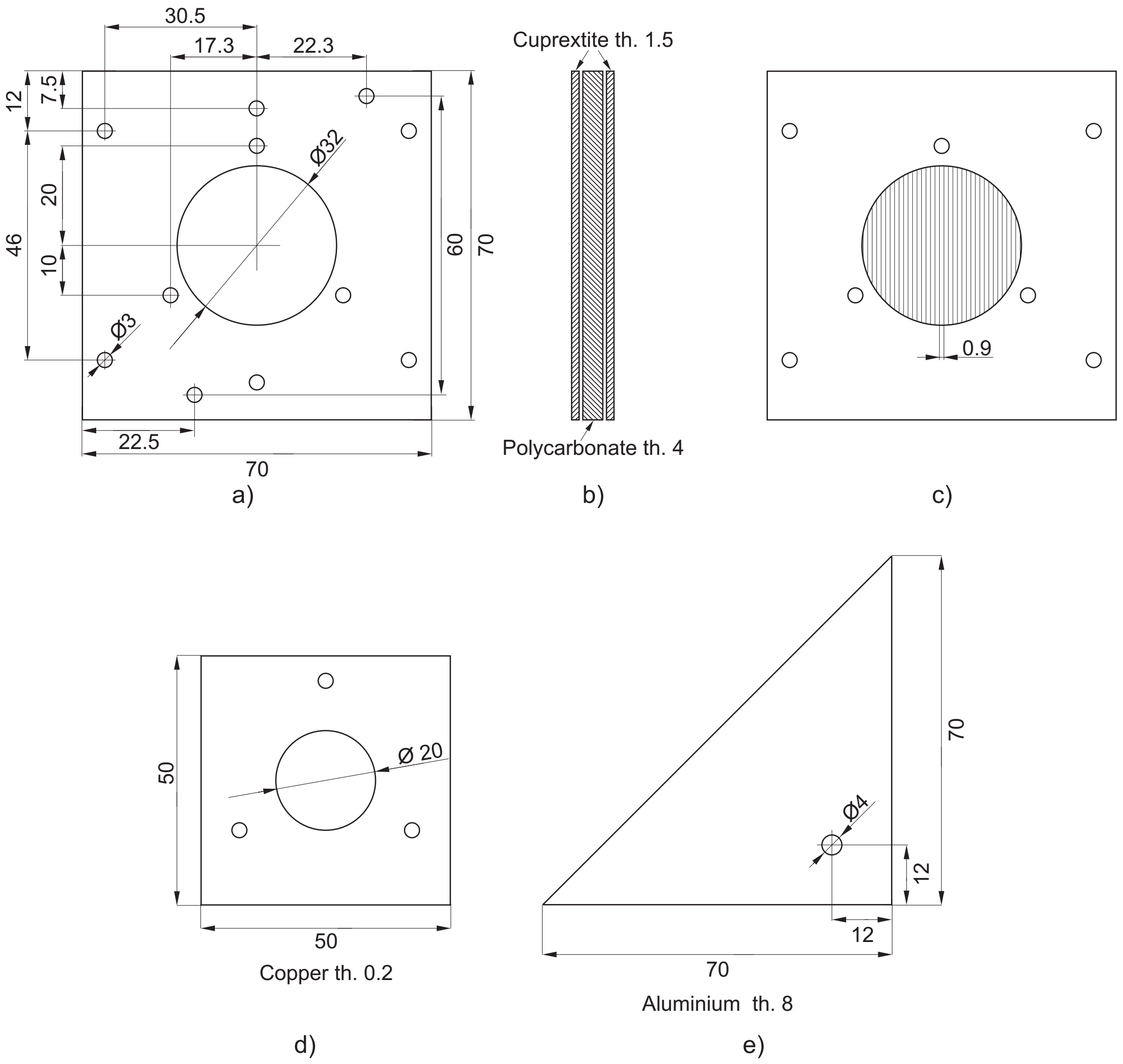

Figure 4.13: The design of the time detector front wall. a) Front view of the front wall. b) Side view of the front wall. c) Accelerating harp. d) Copper frame for fixation of the carbon foil. e) Time detector sidewall. All dimensions in mm. Created in cooperation with V. Semián [22].

4.3 Energy detector

The energy detector used in the TOF telescope is Ortec Model BU-015-300-300 [40]. This is the ion-implanted partially depleted detector of Ultra series with the active area 300 mm^2 (diameter 19.5 mm) and the minimum depletion depth of 300 μm. The guaranteed energy resolution for ^{241}Am 5.486 MeV α-particles is 15 keV FWHM. However, for heavier ions the resolution is assumed to be significantly worser, especially when the carbon foil adds extra straggling. The background in the α-particle energy region (3–8) MeV is better than 30 counts per day [40].

The energy detector is located in the back flange of the second time detector chamber. Because of absence of the second time detector, the energy detector serves to both the energy and TOF measurement of ions passing through the whole telescope. The detector impulse rise time is no more than 10 ns [41].

The energy detector and entrance slit define the solid angle of the TOF telescope.

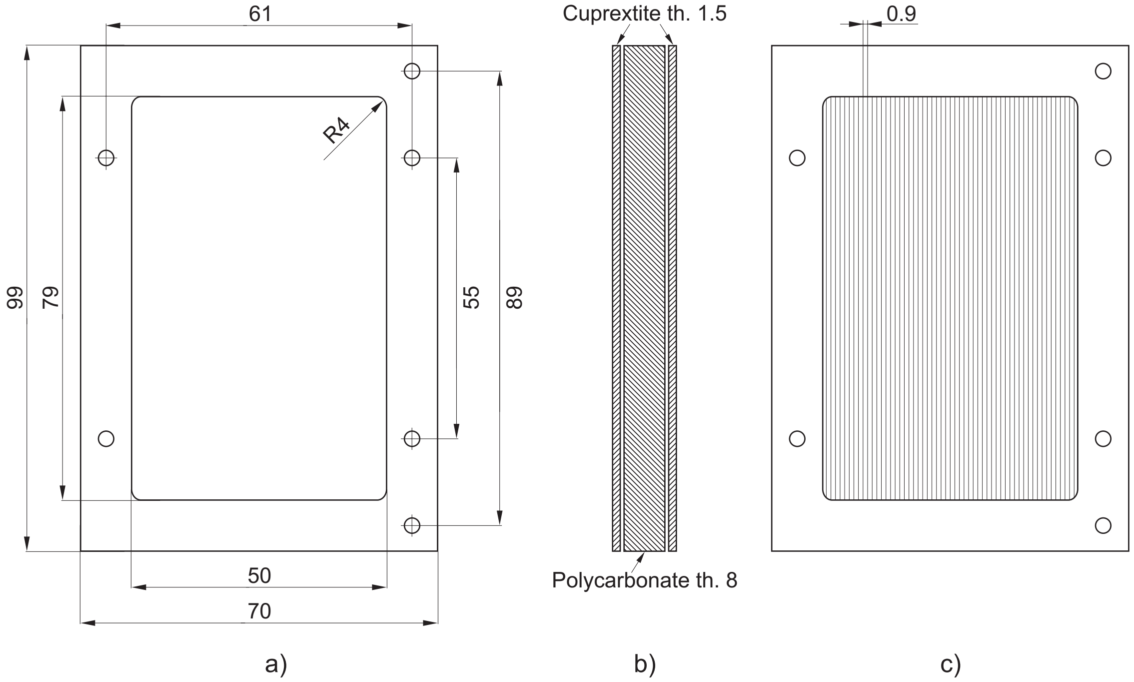

Figure 4.14: The design of the time detector back wall. a) Front view of the back wall frame. b) Side view of the back wall. c) Electrostatic mirror wire harp. All dimensions in mm. Created in cooperation with V. Semián [22].

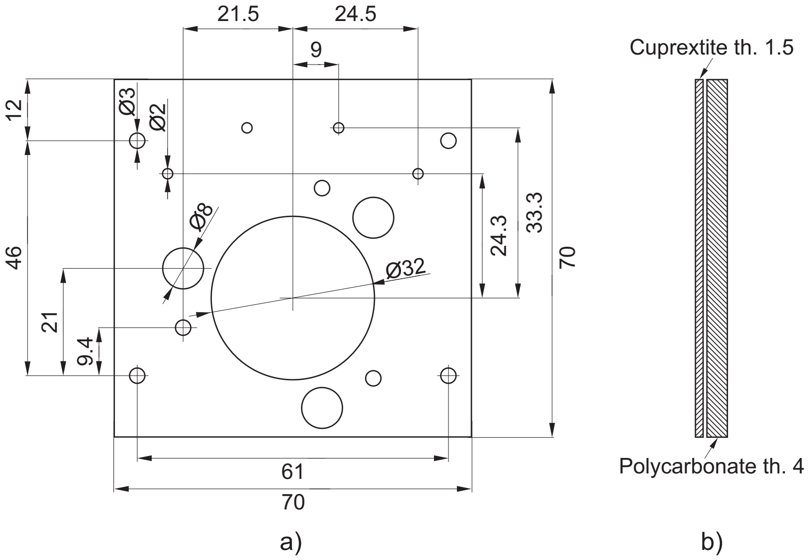

Figure 4.15: The design of the time detector bottom wall. a) Front view of the bottom wall. b) Side view of the bottom wall. All dimensions in mm. Created in cooperation with V. Semián [22].

The distance between the sample inside the target chamber and the energy detector is approximately 1330 mm and the solid angle of the whole setup is 1.696×10^{-4} sr (see the Figure 4.2). Furthermore, the position of the start time detector and the energy detector defines the ion TOF distance of 740 mm. For fast computation of the flight time of any ion, the simplified relation (3.10) holds ($l_{\mathrm{TOF}} = 740$ mm):

$$t_{\mathrm{TOF}}[\mathrm{ns}] = 53.27\sqrt{\frac{m[\mathrm{u}]}{E_{\mathrm{TOF}}[\mathrm{MeV}]}}, \tag{4.2}$$

where m denotes the mass in the atomic mass units (values of constants taken from [14]), and E_{TOF} is the ion kinetic energy in MeV.

4.4 TOF telescope electronics

4.4.1 TOF telescope electronics design

The TOF telescope electronics is designed to accept and process signals from both the time and energy detectors in coincidence. During the selection of appropriate electronics modules, the following signal characteristics were taken into account:

1. Timing signals from MCP detector – see the Figure 4.18
   - fast negative impulse;
   - rise time about 3 ns;
   - impulse base-to-base width about 6 ns, approximate Gaussian shape;
   - impulse FWHM about 3 ns;
   - impulse amplitude from tenths to units of volts, dependent on the HV applied to the MCP detector;
   - output impedance 50 Ω.
2. Energy signals from Si detector preamplifier – see the Figure 4.19
   - positive impulse;
   - rise time about 40 ns;
   - exponential decay time nominally 1 μs;
   - sensitivity of approximately 20 mV/MeV (Si equivalent);
   - output impedance 93 Ω.
3. Timing signals from Si detector preamplifier – see the Figure 4.19
   - negative impulse, transformer derived from the energy impulse;
   - rise time about 40 ns;
   - impulse base-to-base width about 80 ns, approximate Gaussian shape;
   - impulse FWHM about 40 ns;
   - sensitivity of approximately 4 mV/MeV (Si equivalent);
   - output impedance 50 Ω.

With regard to other special requirements on the detector voltage supply (two voltage supplies – up to 100 V and up to 5 kV) and on the computer data acquisition system used, the resulting concept is shown in the Figure 4.16.

4.4.2 Electronics overview and tuning

This section presents the electronics modules belonging to the TOF telescope (see the Figure 4.17) and results of their tuning and testing. Imaging of the electronics signals was performed with the fast 500 MHz Hewlett-Packard Model 54520A Oscilloscope with the maximum sample rate 1 GSa/s.

All the modules were tested with the ^{241}Am α-source of activity approximately 10 kBq. The α-source measurement is further summarized in the Section 5.1. The basic characteristics of the ^{241}Am α-particles are listed in the Table 4.2. The source was located

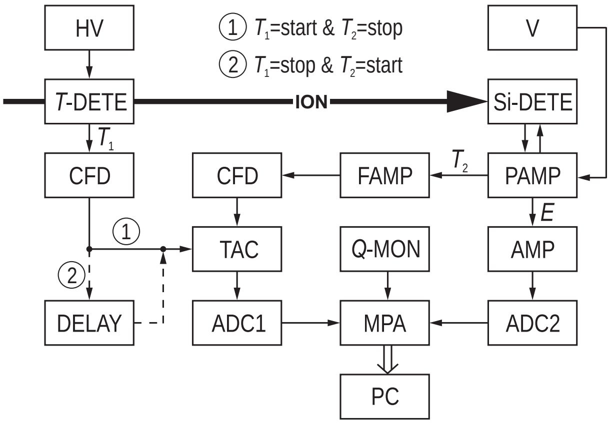

HV	... Time detector high-voltage supply
V	... Energy detector voltage supply
T-DETE	... Time detector
Si-DETE	... Energy detector
CFD	... Constant-fraction discriminator
FAMP	... Fast timing amplifier
PAMP	... Preamplifier
TAC	... Time-to-amplitude converter
Q-MON	... Accumulated charge monitor
AMP	... Amplifier
DELAY	... Delay box
ADC	... Analog-to-digital converter
MPA	... Multi-parameter data acquisition system
PC	... Personal computer

Figure 4.16: The block diagram of the electronics modules for signal processing in the TOF telescope.

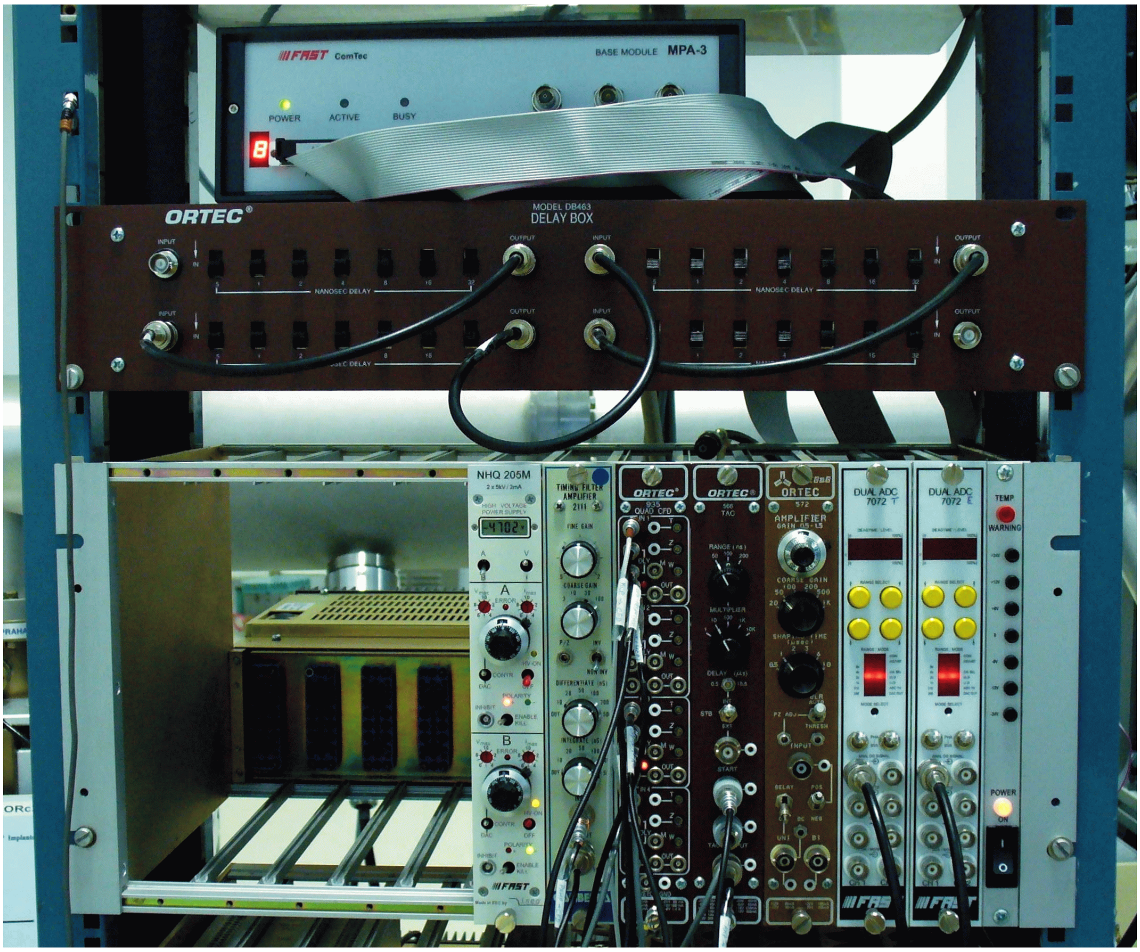

Figure 4.17: The electronics modules used for TOF-ERDA. Top: Multi-parameter data acquisition system. Midst: Delay box. Bottom from the left: Dual HV supply, Fast timing amplifier, Constant-fraction discriminator, Time-to-amplitude converter, Amplifier, two Analog-to-digital converters.

inside the target chamber close to the tube connecting the target chamber with the TOF telescope, faced inwards the telescope.

The basic testing was accomplished with simple test systems constructed from NIM modules available in the laboratory and those from the TOF telescope electronics modules

Decay process	${}^{241}_{95}\mathrm{Am} \rightarrow {}^{237}_{93}\mathrm{Np} + {}^{4}_{2}\alpha$
Decay half-life	432.2(7) yr
Q-value	5637.81(12) keV
Decay mode	α: 100 %
Most intensive α-particles	5388.23(13) [1.6(2) %]
	5442.80(13) [13.0(6) %]
	5485.56(12) [84.5(1) %]

Table 4.2: The properties of ${}^{241}_{95}\mathrm{Am}$ α-decay. Ref. [42].

which were already tested. Otherwise, the test procedures mentioned in the module operating and service manuals were used if necessary.

Voltage supply

The voltage supply for both the time and energy detectors is provided by the Iseg Model NHQ 205M "Precision NIM HV supply" [43]. It is the dual voltage supply with the maximal output voltage ±5 kV and maximal output current 2 mA. Such HV supply provides a high precision output voltage together with the very low noise and ripple. It can be controlled manually by 10-turn potentiometer or remotely via RS232 interface. The PC control allows advanced setting of the module. Due to the LCD display, the direct control and reading of the voltage and current at the proper output is allowed with the resolution of the voltage 1 V and of the current 1 μA. The HV output is provided with the standard SHV connector. Both the SHV and RS232 connectors are located on the rear side of the module chassis.

Time detector

The time detector described in the Section 4.2 is supplied by one unit of the dual HV supply via the SHV connector mounted on the feedthrough on the bottom flange of the time detector chamber. It utilizes the full range of the voltage supply up to -5 kV. The time detector gives fast negative timing pulses. The MCP detector anode is connected to the LEMO connector located beside the SHV one. The MCP output signals are guided directly to the CFD unit without a need of extra amplification. Depending on the applied voltage, the Chevron MCP gives impulses from hundreds of millivolts to units of volts. The noise amplitude during operation was measured to be at most ±7.5 mV which is well bellow the threshold of CFD which first processes the timing signal.

The MCP detector timing signals are shown in the Figure 4.18. Their rise time is (3.2 ± 0.4) ns, the duration determined as a time between the impulse baseline crossings is at most 6 ns. The impulse shape is approximately Gaussian having FWHM 58 % at 2200 V.

Energy detector

The energy detector presented in the Section 4.3 is fed from another unit of HV supply via SHV bias input connector on the rear side of its preamplifier (Ortec Model 142B). The bias voltage +55 V is applied to a detector central electrode. The detector is connected via a Microdot connector to the LEMO output connector located on the back flange of the second time detector chamber. The detector produces a negative output signal with rise time less than 10 ns [41]. However, further output impulse timing properties depend on the preamplifier.

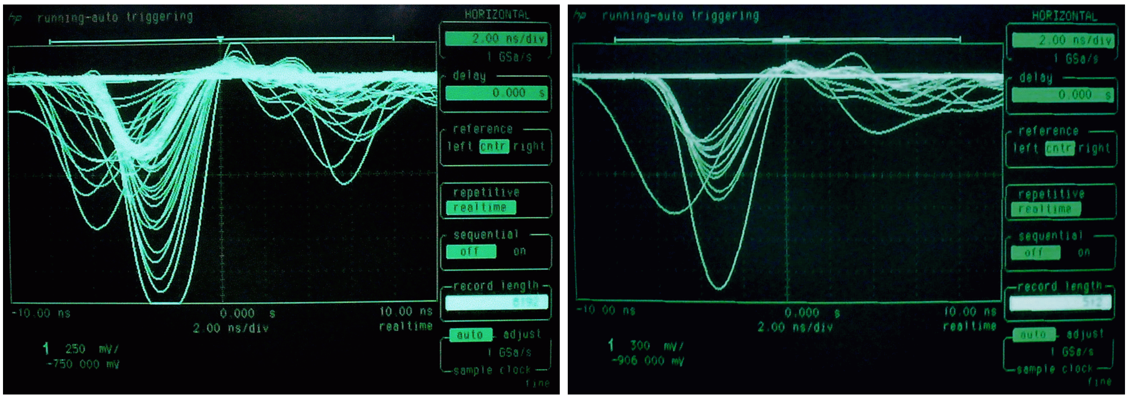

Figure 4.18: The ^{241}Am α-particle time detector signals generated by Chevron MCP. The HV supply voltage set to 4.60 kV, i.e. 2.07 kV per Chevron MCP (left), and to 4.70 kV, i.e. 2.11 kV per Chevron MCP (right).

Energy detector preamplifier

The preamplification of the energy detector signal is provided by the Ortec Model 142B "Preamplifier" [40]. The detector is connected via a short cable to the BNC input connector (93 Ω input impedance). The preamplifier gain is greater than 80,000. It also provides the energy detector bias supply.

The preamplifier furnishes time (50 Ω output impedance) and energy (93 Ω output impedance) output signals, see the Figure 4.19. The energy output signal is of the positive polarity and its charge sensitivity is nominally 20 mV/MeV (Si equivalent). Its rise time is approximately 40 ns and the decay time is nominally 1 μs.

The time signal is transformer derived from the energy signal. It has the negative polarity. Its rise time is also approximately 40 ns, the duration of the whole impulse between the baseline crossings is approximately 80 ns. Due to transformation, the time signal has the charge sensitivity only about (3–4) mV/MeV (Si equivalent). As the kinetic energy of ions detected in TOF-ERDA varies from several hundreds of keV up to units of MeV, the time signal sensitivity is insufficient for further signal processing as it is much lower than the CFD lowest threshold value. Thus the fast amplifier which accepts and furnishes negative signals is necessary for the preliminary version of the TOF telescope. The final version with the both time detectors will definitely fix this problem.

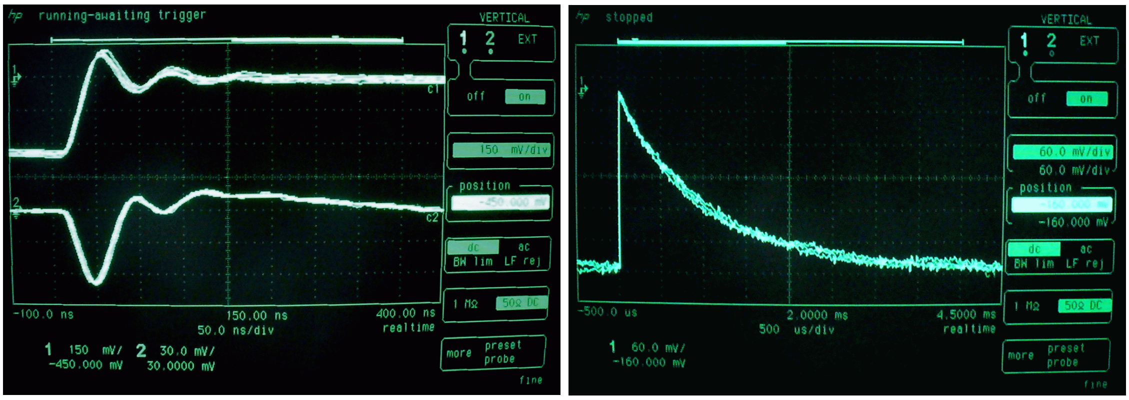

Figure 4.19: The energy detector preamplifier signals. Left: The upper signal is the energy output signal and the lower one is the time output signal. Right: The preamplifier energy output signal.

Fast timing amplifier

The amplification of the timing signal from the energy detector preamplifier is provided by the Canberra Model 2111 “Timing filter amplifier” [44]. It accepts and furnishes both the positive and negative signals (50 Ω input and output impedance). Its gain is finely tuned between 1.5× and 200×. The amplifier further provides pole-zero cancellation adjustment and independent setting of the signal RC integration and differentiation for further enhancement of the detection performance via the rise time normalization and the pile-up minimization for all impulses. This module introduces an extra transmission delay of 13 ns. Thus the total TOF measurement delay caused by electronics and interconnecting cables after the final tuning is 53 ns.

Constant-fraction discriminator

To improve the TOF measurement as much as possible, the Ortec Model 935 “Quad constant fraction 200 MHz discriminator” is used [40]. This module contains four independent channels. All four CFDs accept fast negative signals from 0 to −10 V and furnish −800 mV logic pulses. The connections are made via the LEMO connectors (50 Ω input and output impedance). Each CFD unit allows setting of the input signal threshold in the range from −20 mV to −1000 mV, the fine-tuning walk adjustment, and also the output logic pulse width.

The pulse constant fraction is nominally 20 %. The CFD is connected in the blocking mode via internal jumper setting, which means that until the first pulse is processed no further is accepted. The pulse pair resolution is better than 7 ns and the input/output rate is lowered to more than 150 MHz. In the blocking mode, the output signal gains a modified tail as evident in the Figures 4.20 (left) and 4.21.

Figure 4.20: The CFD signals. Left: The CFD bipolar and associated output signal converted from the input time detector signal. Right: The CFD bipolar and associated output signal converted from the input energy detector preamplifier timing signal.

After proper tuning of all CFD controls and external cable delays, both CFD output signals were displayed together with the help of the fast oscilloscope, see the Figure 4.21 (right). The energy detector signal is not amplified by the Canberra 2111 timing amplifier, yet. The channel 2 shows the time detector signal used as a start signal while the channel 1 shows the energy detector signal serving as a stop signal.

As evident from the Table 4.2, the dominant ^{241}Am α-particles have the kinetic energy 5.486 MeV. From the equation (4.2) the α-particle flight time equals approximately 45.5 ns. The Figure 4.21 (right) shows that the measured time is longer, approximately 86 ns. The

source x1, y1: Channel 2
x1 position: -8.900 ns
y1 position: -9.37500 mV
source x2, y2: Channel 2
x2 position: -6.100 ns
y2 position: -900.000 mV

y2(2) -900.000 mV
y1(2) -9.37500 mV
delta y -890.625 mV
x2(2) -6.100 ns
x1(2) -8.900 ns
delta x 2.800 ns
1/delta x 357.143 MHz

source x1, y1: Channel 1
x1 position: 77.20 ns
y1 position: 609.375 mV
source x2, y2: Channel 2
x2 position: -8.800 ns
y2 position: 5.46875 mV

y2(2) 5.46875 mV
y1(1) 609.375 mV
delta y -603.906 mV
x2(2) -8.800 ns
x1(1) 77.200 ns
delta x -86.000 ns
1/delta x 11.6279 MHz

Figure 4.21: The coincidence CFD timing. Left: The CFD logic output signal characteristics. Right: The coincidence CFD output signals of ^{241}Am α-particle passage through the TOF telescope. The left signal is generated by the time detector while the right signal is converted from the energy detector (vertical scale given by the channel 2).

40 ns difference is due to the complicated time signal production by the energy detector, where the pulse generation time in the Si together with the transmission delays through the appropriate electronics modules and also through the interconnecting cables play a role. However, this delay is assumed to be almost the same for all measured ions. Alternatively, a possible shift will be of the order of units of nanoseconds which is small compared to the ion TOF values. Thus this will result in a constant shift in the time spectrum without any significant impact on the E-TOF coincidence spectrum.

Amplifier

As an energy detector signal amplifier the Ortec Model 572 “Spectroscopy amplifier and pile-up rejector” is used [40]. It accepts both the positive and negative impulses with rise time from 10 ns to 650 ns and the decay time from 40 to 2000 μs with maximal amplitude 1 V. The amplifier provides continuous setting of the gain in the range from 1× to 1500×. The Gaussian pulse shaping with shaping times from 0.5 μs up to 10 μs, the pole-zero cancellation and baseline restoration are available.

The output signals are positive unipolar or positive lobe leading bipolar prompt or 2 μs-delayed active filter shaped impulses. The input and output connectors are located on both the front and rear sides of the chassis. They differ by the impedance – the front panel connector impedance is 0.1 Ω, while the rear side connectors include 93 Ω impedance. The 93 Ω impedance connectors are thus prefered.

The amplifier was properly tuned. The shaping time is selected to be 2 μs. Thanks to relatively low countrates prefered for analysis and to the fact that signals are produced by the Si detector, these shaping times are sufficient. The baseline restoration is tuned manually but the auto option also provides very good performance. As the output the rear side unipolar signals are further used, see the Figure 4.22.

Delay box

As apparent from the electronics block diagram in the Figure 4.16, two different timing arrangements are used for the TOF measurement. There are two timing signals indicating the passage of the ion through the TOF telescope, one is always treated as the starting signal and the other as the stopping one. Regardless the intensity of the beam, almost

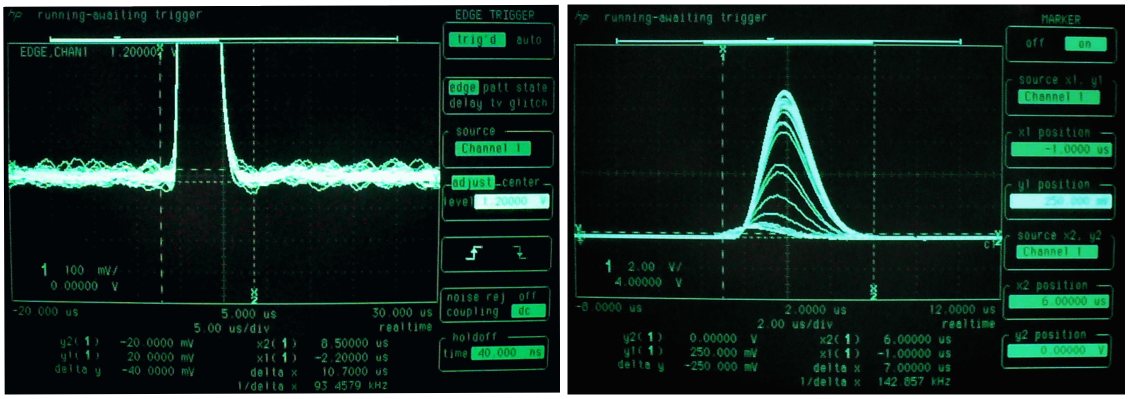

Figure 4.22: The energy detector amplifier tuning. Left: The proper pole-zero cancellation adjustment. Right: The ^{241}Am α-particle energy unipolar output signals (shaping time 2 μs).

all ions which enter the telescope and pass through the slit are registered by the first time detector, but only a part of them will reach the energy detector. If the first timing detector is equipped with MCPs, its dead time is extremely short and millions of events per second can be registered. This results in overloading of the TAC unit and in worsening of its performance.

However, not every ion registered by the time detector is registered also by the energy detector – the so called start-to-stop arrangement, option "①" in the Figure 4.16. The opposite arrangement, when the start signal is provided by the second energy detector and the stop signal by the time detector, affords another possibility – the so called stop-to-start arrangement, option "②" in the Figure 4.16. Then, the tunable delay is necessary for delaying the time detector signal to arrive after the energy detector impulse. For the presented preliminary setup, optimal beam currents for TOF-ERDA are of the order of units of nA, which induce coincidence countrates up to some tens of events per second. Thus the start-to-stop arrangement suffices and is further used for the TOF telescope testing. In the final arrangement with the both time detectors the countrates will increase which implies the stop-to-start arrangement advantage.

For the delay purposes, the Ortec Model DB463 "Delay box" is used. It contains four independent delay units equipped by a calibrated 50 Ω coaxial cable[1]. One unit provides the maximal delay of 63.5 ns tunable in 0.5 ns steps. If all the units are interconnected, the total delay is fourfold, i.e. 254 ns, plus an extra delay given by the interconnection cables. Inputs and outputs are provided via the BNC connectors.

Time-to-Amplitude converter

Measurement of the flight time of ions is provided by the Ortec Model 566 "Time-to-amplitude converter" [40]. It accepts negative impulses with the threshold −400 mV, the input impedance is 50 Ω. The full-scale time interval between the accepted input impulses ranges from 50 ns to 2 ms with the resolution of 10^{-4} of the proper full-scale time. For the TOF-ERDA purpose, intervals up to 1 μs are sufficient. The output signal amplitude varies from 0 V to +10 V linearly proportional to the start-stop input signal time difference (output impedance less than 1 Ω) . The converter further allows delaying the output pulse up to 10.5 μs with reference to the input signal. This possibility is used to make the TAC

---

[1] 1 meter long 50 Ω coaxial cable corresponds to 4.8 ns delay.

output signal and the amplifier energy output signal arriving to the ADCs with a small mutual time difference because of their coincidence measurement, see the Figure 4.23.

off on
source x1, y1: Channel 1
x1 position: 2.00000 us
y1 position: 8.90625 V
source x2, y2: Channel 1
x2 position: 2.04000 us
y2 position: 9.09375 V

y2(1) 9.09375 V
y1(1) 8.90625 V
delta y 187.500 mV
x2(1) 2.04000 us
x1(1) 2.00000 us
delta x 40.000 ns
1/delta x 25.0000 MHz

Figure 4.23: The TAC and the amplifier output signal matching. The time difference between the signals arrival to ADCs is minimized by setting the TAC output delay.

Analog-to-Digital converter

The pulse-height analysis of both the TAC and amplifier output signals is provided by the FAST Model 7072 “Dual 500 ns analog-to-digital converter” [45]. It accepts both the positive and negative uni- or bipolar impulses with maximal amplitude from ±25 mV to ±10 V (input impedance 1 kΩ). The signals are optimized for Gaussian shaping with internal circuit selected shaping times ranging from 250 ns to 25 μs. The conversion time is fixed to be 500 ns.

The ADC allows setting of the input signal threshold, the low and high discrimination level, and also the output signal voltage. It operates in both the coincidence or anticoincidence modes. Typical dead-time for fast impulses is less than 2 μs. The conversion range varies from 256 to 8192 channels. The output signals are transferred via 25 pin D-SUB connector located on the rear side of the ADC into the final part of the electronics line – the FAST Multi-parameter system.

Multi-parameter data acquisition system

For spectra acquisition, the unique high-performance FAST Model MPA-3 “Multi-parameter multichannel analyzer system” is used [45]. It consists of two main parts – ADC port modules and a PC card. Each ADC port module contains four parameter systems. The whole port system can be extended up to four modules, i.e. 16 parameter systems operable simultaneously.

Each parameter subunit contains 16-bit ADC and allows the integral throughput greater than 300,000 single or coincidence events per second. Each ADC input provides livetime correction. The PCI-bus interface card controls completely all parameters. It allows the full remote control of the experiment, the data storage in the PC and also simple analysis. It accepts ADC inputs and control lines via the 25-pin D-SUB connector. The FAST multi-parameter bus is provided by the 50-pin Centronics connector. The FAST high-speed link for the MPA-3/PC communication is provided by the 37-pin D-SUB cable.

The MPA-3 system is controled via a graphical interface MPANT. It is the MS Windows based software, which controls the data acquisition from MPA-3 single parameter systems. It allows various setting of criteria applied to incoming signals, creates different types of spectra and provides also a basic analysis. The spectra obtained with MPANT are shown in the Section 5.2.

Accumulated charge monitor

A number of ions which impacted on the sample (their accumulated charge) is measured by the manually controlled Faraday cup. It is located between the accelerator high-energy magnet and the target chamber. Due to the additional circular slit in front of the sample (2 mm in diameter), which defines the beam diameter and cross-section, the real value of the ion current impacting on the sample is assumed to be attenuated by a factor 10.

This method is only temporary. It will be replaced by a propeller rotating in the beam, which is located near the target chamber entrance. Its surface facing outwards the target chamber will be covered by Au layer several micrometers thick and the energy detector faced towards the propeller gold-plated surface will record the RBS spectra of the scattered projectiles. This can serve for both the relative and absolute measurement of the accumulated charge.

Chapter 5

TOF Telescope Testing

This chapter describes testing of the simple TOF-ERDA device constructed at NPI. Preliminary results were obtained with the ^{241}Am α-source. Then a set of real samples was measured with an ion beam from the Tandetron accelerator. The results are discussed.

5.1 Measurement with ^{241}Am α-source

As mentioned in the Subsection 4.4.2, the TOF telescope electronics modules were first tested with the ^{241}Am α-source. The source was fixed in a polycarbonate holder made for this purpose. It was placed inside the target chamber at the entrance of the tube which connects the target chamber and telescope, and was faced inwards the telescope. After tunning all modules, it was used also for the first test of the whole TOF telescope, see the Figure 5.1.

The α-particles were registered in coincidence by both the time and energy detectors arranged in the start-to-stop geometry, i.e. the time start signal was furnished by the time detector while the time stop and energy signals by the energy detector. The HV applied to the MCP detector was 2.11 kV which corresponds to 4.7 kV on the HV supply output. The TAC full-scale time interval between the accepted input impulses was 200 ns. Because this measurement carried out before the fast timing amplifier was available (low count statistics), and also before thorough tuning of electronics, the obtained results are only informational and do not serve for further calibration purposes. Due to the low sensitivity of the TOF measurement (see the Subsection 4.4.1), only α-particles with maximal energy were registered (almost monoenergetic α-particles).

Both the energy and TOF spectra were fitted by Gaussian functions (see Table B.1) to find positions of the dominant α-peaks. The energy spectrum was fitted by the sum of three Gaussian functions. The TOF spectrum was fitted by only one Gaussian function because in this temporary arrangement the resolution of the time measurement was low to obtain corresponding three separable time peaks.

For completeness, energy losses of the ^{241}Am α-particles detected within the telescope were evaluated with the help of SRIM 2003 code [16]. The α-particles lose their energy twice – within the 110 nm (1140×10^{15} at. cm^{-2}) thick time detector carbon foil ($\Delta E_{\mathrm{foil}} \approx 17$ keV) and also within the 50 nm (250×10^{15} at. cm^{-2}) thick entrance window of the energy detector ($\Delta E_{\mathrm{det}} \approx 7$ keV) [32, 40]. The energy spectrum fit parameters together with corrected energies $E_{\alpha}^{corr} = E_{\alpha} - \Delta E_{\mathrm{foil}} - \Delta E_{\mathrm{det}}$ of α-particles, and the corresponding TOF spectrum fit parameters are listed in the Table 5.1.

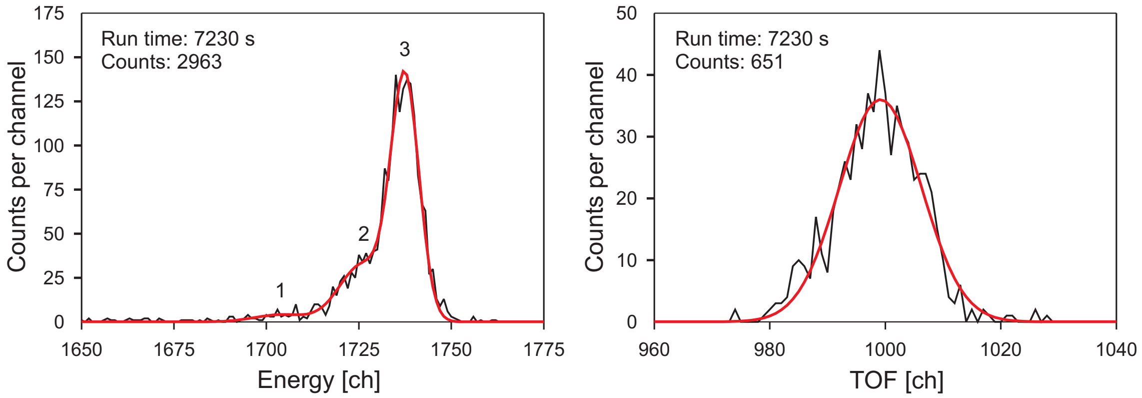

Figure 5.1: The first energy and TOF spectra of the ^{241}Am α-particles.

Peak number	E_{α}^{corr} [keV]	μ [ch]	σ [ch]	FWHM [ch]
Energy spectrum				
1.	5364.47	1703.41 ± 5.88	8.85 ± 3.78	20.84 ± 8.90
2.	5419.21	1726.49 ± 0.53	6.88 ± 0.41	16.20 ± 0.97
3.	5462.10	1737.49 ± 0.09	4.04 ± 0.08	9.51 ± 0.19
TOF spectrum				
1.	–	999.17 ± 0.18	7.10 ± 0.19	16.72 ± 1.67

Table 5.1: The list of parameters of the ^{241}Am α-particle energy and TOF spectra fit. μ and σ denote the peak position and its standard deviation in channels, respectively.

The Table 5.1 shows that the energy resolution of the TOF spectrometer energy detector is about 30 keV FWHM for 5486 keV α-particles (mean conversion factor for energy scale: 3.14 keV/ch). This value is caused mainly due to the additional straggling within the carbon foil. The TOF spectrum fit shows a peak located at 97.6 ns (999 ch; conversion factor for time scale: 9.77×10^{-2} ns/ch). It is shifted for 52 ns relative to the real ^{241}Am α-particle TOF through the telescope which is approximately 45.6 ns. This effect is caused by the electronics transmission delays (see the Subsection 4.4.2). The resulting TOF telescope time resolution for the detected α-particles is about 1.6 ns (16.7 ch) FWHM, see the Table 5.1.

5.2 TOF-ERDA analysis of real samples

The first measurements with the completely equiped TOF telescope were carried out under the following conditions:

- Cu^{6+} projectiles with the kinetic energy 15.4 MeV (terminal voltage 2.2 MV);
- 3.3 nA full beam current during the whole experiment (measured by the manual Faraday cup located between the high energy magnet and target chamber);
- 2 mm beam cross-section (defined by the slit located inside the target chamber in front of the target);
- experimental geometry: incident beam angle 60°, exit recoil angle 75°, and scattering angle 45° with reference to the sample surface normal;
- 2.11 kV applied to the MCP detector (4.7 kV on HV supply output);
- 500 ns TAC full-scale time interval between the accepted input time impulses;

- 2048 ch ADC conversion range for all spectra;
- 300 ns coincidence time interval between TOF and energy signals from ADCs (defined by MPANT software).

The examined samples were the following (sample properties taken from [14, 16, 36]):

- bulk glassy carbon (pure amorphous non-graphitizing C, density 1.50 $\mathrm{g\,cm^{-3}}$);
- bulk single-crystal sapphire (Al_2O_3, density 3.98 $\mathrm{g\,cm^{-3}}$);
- evaporated LiF layer (density 2.64 $\mathrm{g\,cm^{-3}}$, thickness 2452×10^{15} $\mathrm{at.\,cm^{-2}}$, i.e. 200 nm) on the glassy carbon substrate;
- ACF carbon foil (density 2.01 $\mathrm{g\,cm^{-3}}$, thickness 1140×10^{15} $\mathrm{at.\,cm^{-2}}$, i.e. 22 $\mu\mathrm{g\,cm^{-2}}$ or 109.5 nm) on an unknown glass substrate which was treated as a soda-lime glass[1] (density 2.40 $\mathrm{g\,cm^{-3}}$).

The measured carbon foil is the same and thus has the same properties as that contemporarily used in the time detector.

The measured spectra together with the results of their preliminary analysis are shown in the Figure 5.2 for the glassy carbon sample, in the Figure 5.3 for the sapphire sample, in the Figure 5.4 for the LiF layer on the glassy carbon substrate and in the Figure 5.5 for the carbon foil on the glass substrate. Following spectra are shown:

- top left spectrum is a single spectrum of the ion remaining energy which was recorded by the energy detector itself (pure ERDA spectrum). It includes maximal number of events from all spectra because of almost 100% ion registration efficiency, i.e. every ion which reached the energy detector entrance window was registered.
- top right spectrum is a single TOF spectrum, which contains the measured flight times of ions detected by time and energy detectors simultaneously. Due to the time detector operation principle the detection efficiency is little lower than in the case of the energy detector itself.
- middle spectrum is the 2D coincident E-TOF spectrum. It contains events registered by the time and energy detectors in coincidence, with associated both the ion TOF and energy values.
- bottom spectrum is the energy spectrum obtained as the sum of projections of the single-elemental spectra on the energy axis (only elements which are dominant or expected with respect to the appropriate sample (Li, C, O, F, Na, Al, Si) were taken into account). Full lines show the results of simulations by SIMNRA 6.03 code [46].

Because of the factual absence of a suitable analysis software for the complete analysis of the TOF-ERDA spectra, and because of the provisional low time resolution of the TOF spectrometer preliminary setup, only the above mentioned TOF-ERDA energy spectra were analyzed. For this purpose SIMNRA 6.03 code [46] was successfully utilized. The sample characteristics extracted from the spectra are the energy calibration, accumulated charge within the sample surface layer, and elemental composition, thickness and roughness of the examined sample surface (sub)layers. During the analysis of all spectra both the time detector carbon foil and energy detector entrance window and corresponding energy losses and straggling were taken into account by SIMNRA 6.03.

---

[1] Soda-lime glass composition: SiO_2 73 %, Na_2O 14 %, CaO 7 %, MgO 4 %, Al_2O_3 2 %; corresponding elemental stoichiometry: O 60.04 at. %, Si 24.33 at. %, Na 9.33 at. %, Ca 3.50 at. %, Mg 2.00 at. %, Al 0.80 at. %.

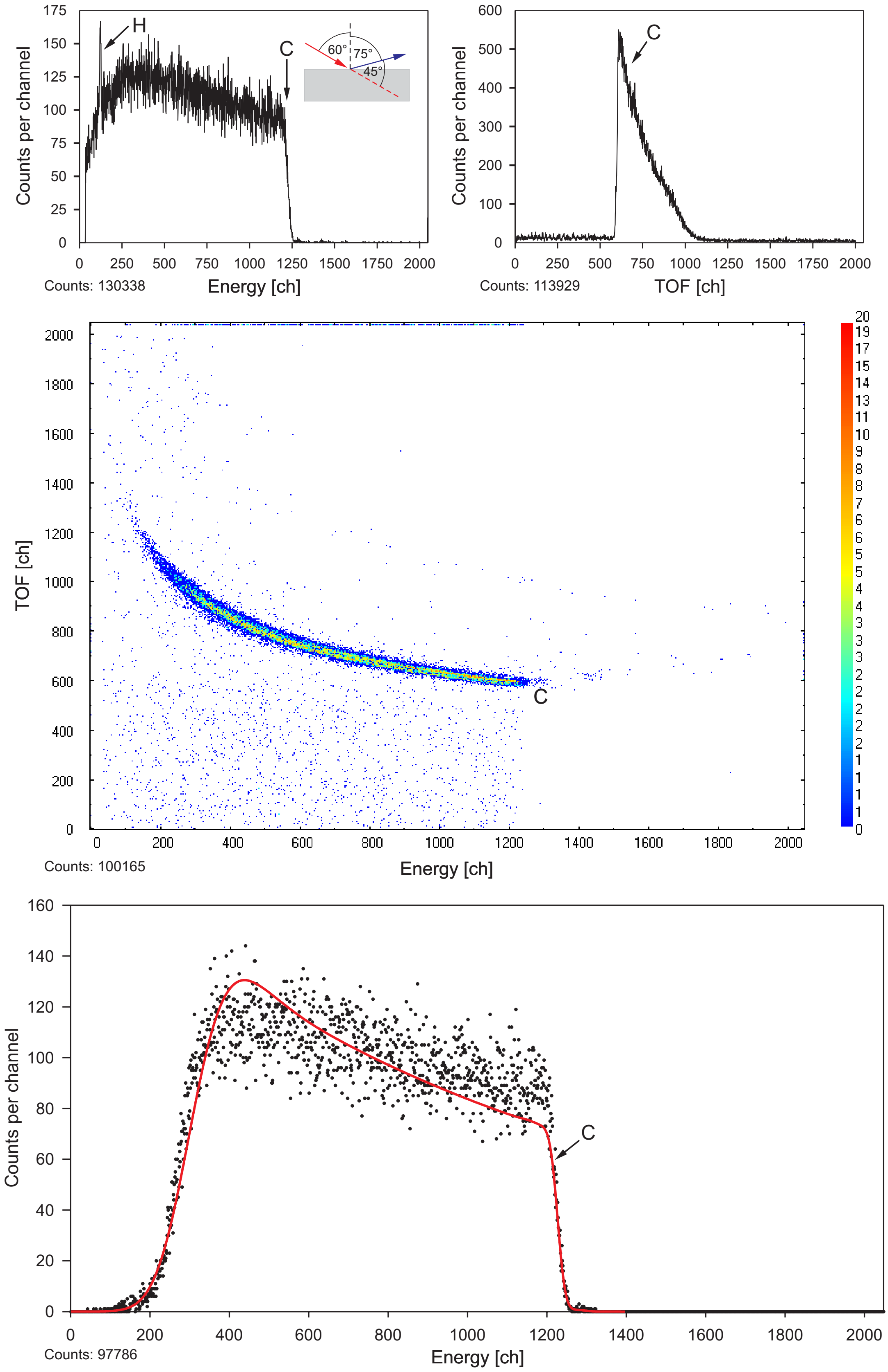

Figure 5.2: The TOF-ERD analysis of the glassy carbon sample with Cu ions. The high-energy edges of dominant elements are shown in the upper spectra.

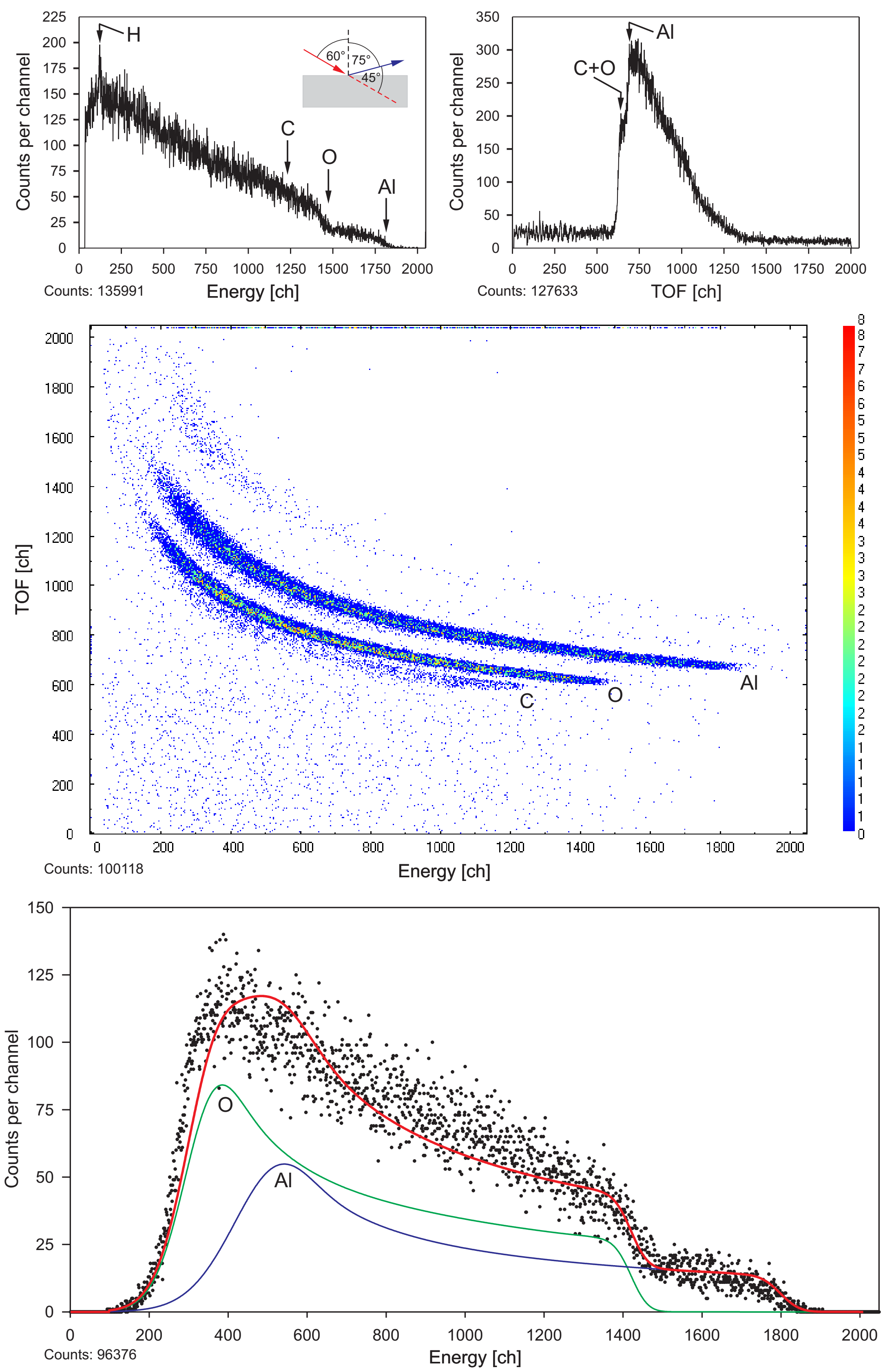

Figure 5.3: The TOF-ERD analysis of the sapphire (Al_2O_3) sample with Cu ions. The high-energy edges of dominant elements are shown in the upper spectra.

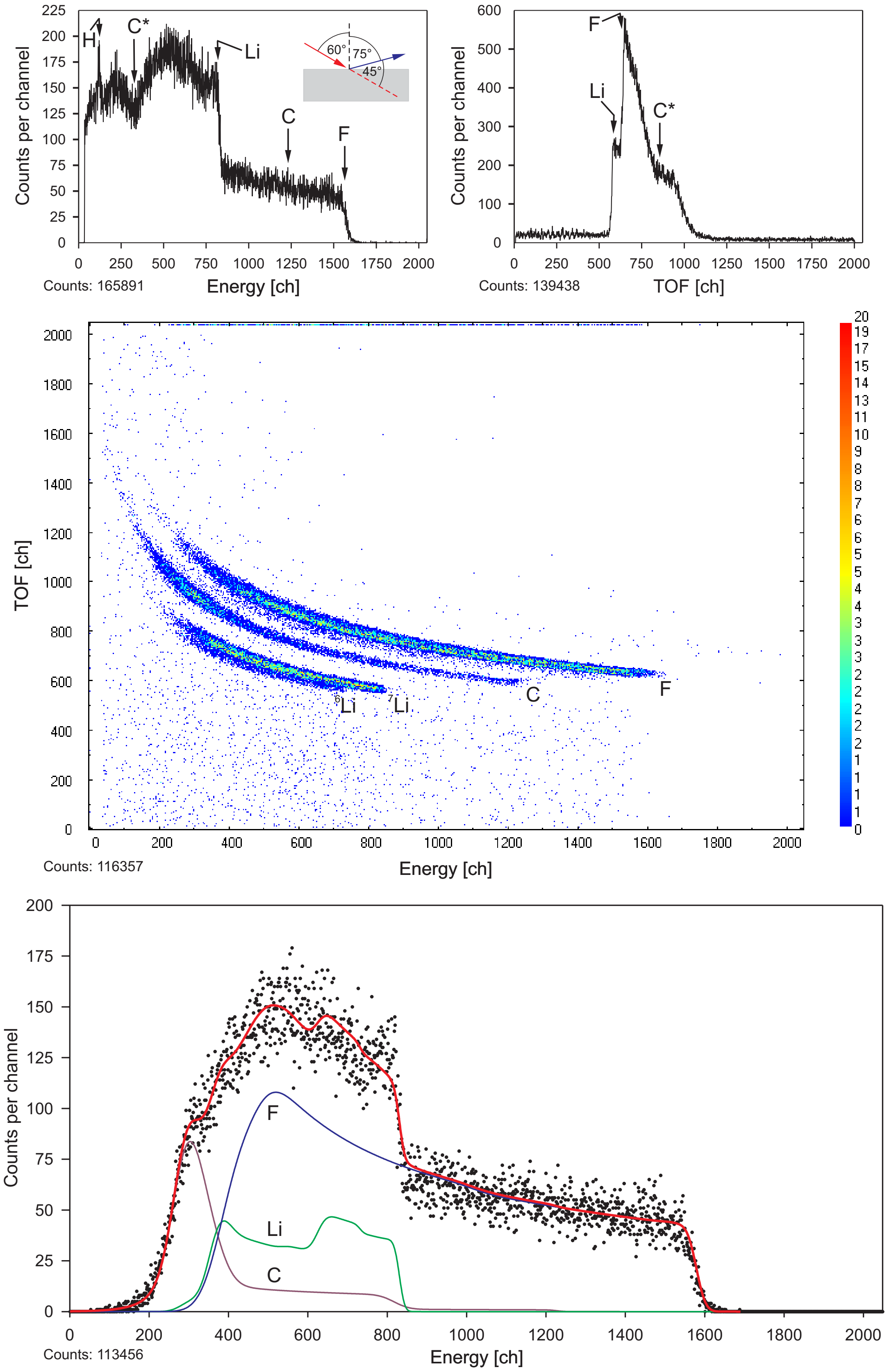

Figure 5.4: The TOF-ERD analysis of the LiF layer on the glassy carbon substrate with Cu ions. The high-energy edges of dominant elements are shown in the upper spectra. The asterisk in the upper right index denotes the substrate element.

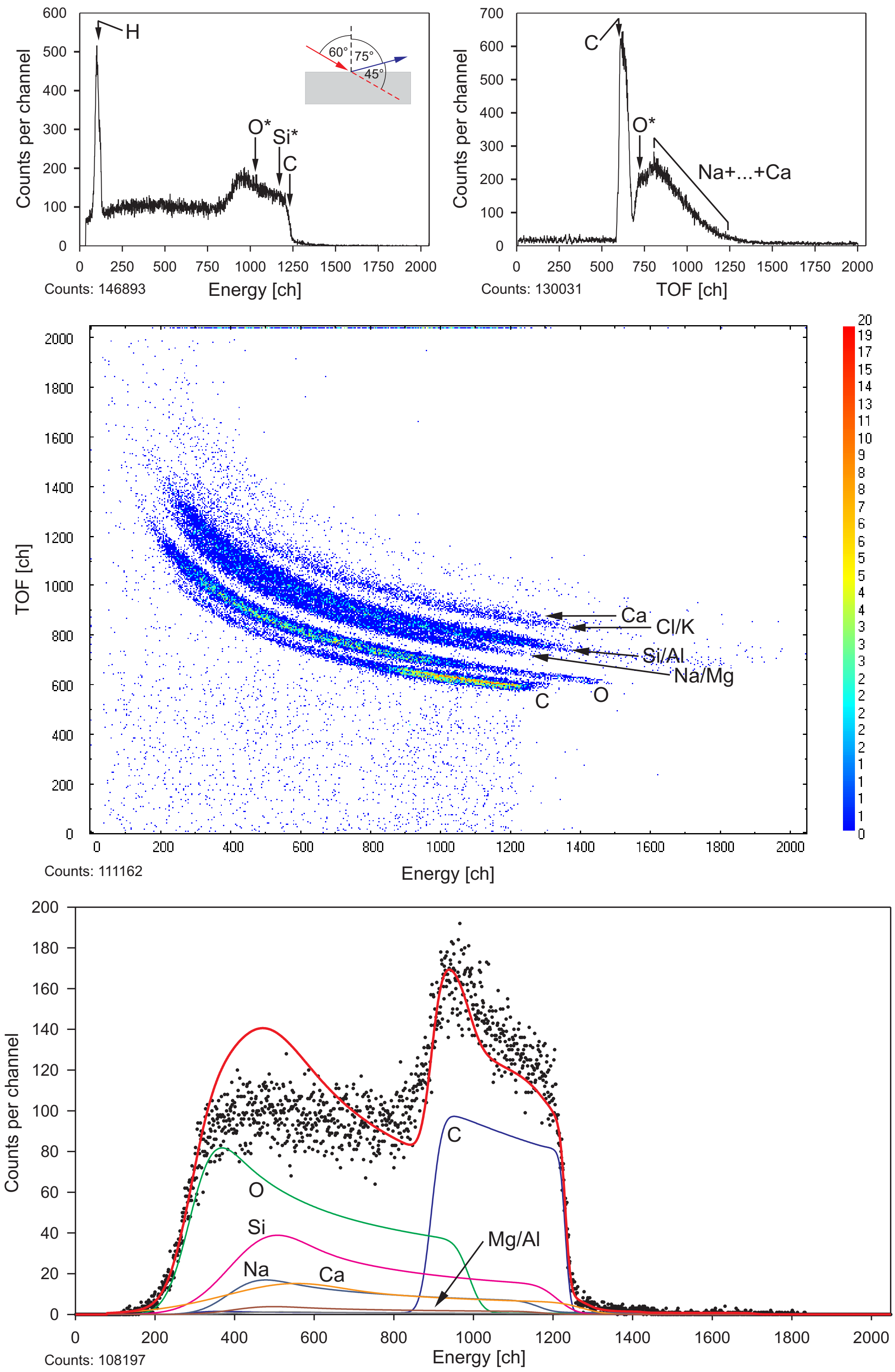

Figure 5.5: The TOF-ERD analysis of the ACF carbon foil on the glass substrate with Cu ions. The high-energy edges of dominant elements are shown in the upper spectra. The asterisk in the upper right index denotes the substrate element.

The energy detector calibration was made via an alternative way. Instead of single element calibration, i.e. recording of energy spectra at several different projectile energies for each element of interest, which is very time consuming, a method allowed by SIMNRA 6.03 code was used. It is based on fitting the position of high energy edges of the single-elemental spectra. These edges correspond to the highest possible recoils energies defined by equation (3.2) reached with the given projectiles, i.e. the energy of the recoils from the first surface layer without sample stopping influence.

However, the real energy calibration is nonlinear and varies for each element. It is caused by the ion detection principle in solid-state detectors. If heavier ion is measured in contrast with protons or He ions/α-particles, it strongly ionizes the detector material along its path and a part of generated electron-hole pairs recombines immediately and does not participate on the further signal generation, a so-called pulse-height defect [47]. Because SIMNRA 6.03 code disallows all but linear fitting, separate linear energy calibrations were used for groups of the main elements of interest. The best energy calibration fits were obtained for element groups Li-C and O-F-Al, and were kept fixed for those elements during analysis of all samples. Remaining elements from the carbon foil substrate glass were fitted additionally during the appropriate spectrum analysis. The resulting calibration coefficients for the elements of each group are listed in the Table 5.2.

Element group	Slope [keV/ch]	Offset [keV]
Li-C	3.147 ± 0.002	51.279 ± 0.586
O-F-Al	3.454 ± 0.002	–262.082 ± 0.449
Na-Mg-Si-Ca	3.450 ± 0.008	–267.643 ± 1.567

Table 5.2: The energy calibration of the TOF-ERDA energy spectrum for the main analyzed elements fitted by SIMNRA 6.03 code [46].

The meaning of the layer thickness and roughness is depicted in the Figure 5.6. The thickness of the layer is taken as a mean distance between the layer surfaces. The roughness of the surface is expressed by the FWHM of a distribution of distances of the real surface elements from the virtual mean ideally flat surface. The roughness was calculated only for the top and bottom sublayers excepting middle sublayers which copy the roughness profiles of the neighbouring ones. The elemental composition of the sample (sub)layers was fitted simultaneously with their thickness.

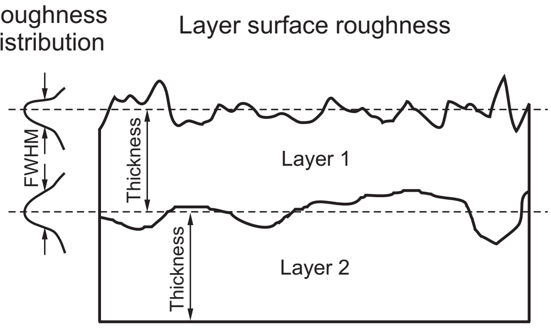

Figure 5.6: The illustrative scheme of the sample thickness and roughness description.

The results of the energy spectra analysis performed by SIMNRA 6.03 are summarized in the Table 5.3 and are shown in the bottom spectra in the Figures 5.2–5.5. The coincidence detection efficiency is taken as the ratio of the number of E-TOF coincident events and the number of events registered by the sole energy detector. The Table 5.3 further provides comparison between the value of the current of the beam impacting on the sample and that measured by the Faraday cup. From the values of the run time and accumulated charge which are listed in first and second columns, respectively, it implies that the beam current mean value, taking into account the charge state of Cu ions, was (347 ± 30) pA. Comparing with the value 3.3 nA obtained by the Faraday cup, it is evident that the 2 mm slit located at the entrance of the target chamber attenuates the initial beam by a factor $(10.5 \pm 0.9) \times 10^{-2}$ which agrees well with the theoretical assumption from the Section 4.4.

Run time [s]	Accumulated charge [nC]	Layer composition			
		Number of (sub)layer	Thickness [10^{15} at. cm^{-2}/nm]	Roughness FWHM [10^{15} at. cm^{-2}/nm]	Relative elemental abundance [at. %]
Bulk glassy carbon sample (Coincidence detection efficiency: 76.85 %)					
2099	133	1.	3526/468.9	765/101.7	C 100
Bulk single-crystal sapphire sample (Coincidence detection efficiency: 73.62 %)					
2111	102	1.	3441/289.6	281/23.7	Al 38; O 62
Evaporated LiF on glassy carbon substrate (Coincidence detection efficiency: 70.14 %)					
2222	154	1.	1522/142.5	$\lesssim$ 10/0.9	Li 34; F 65; C 1
		2.	1693/163.5	–	Li 20; F 72; C 8
		3.	299/29.7	–	Li 26; F 45; C 29
		4.	170/20.6	–	Li 5; F 28; C 67
		5.	40/5.32	301/40.0	C 100
ACF carbon foil on soda-lime glass substrate (Coincidence detection efficiency: 75.68 %)					
2677	140	1.	1340/133.7	315/31.4	C 98.8; O 0.9; Na 0.3
		2.	2011/302.1	98/14.7	Si 23; O 54; Na 11 Ca 8; Mg 2; C 1; Al 1

Table 5.3: The results of the SIMNRA 6.03 [46] analysis of the TOF-ERDA energy spectra of the real samples. The thicknesses in nm are calculated by Gisa 3.99 code [48] for the fitted layer elemental composition (layer density determined by Gisa 3.99 code). The number of the (sub)layer increases with its depth under the sample surface, i.e. the outermost surface layer has number 1.

Next, the 2D coincident E-TOF spectra are converted to so-called energy-mass (left) and mass (right) spectra, see the Figures 5.7 – 5.10. The time scale was converted to the ion mass scale via the equation (3.10). The energy-mass spectra are useful for easy separation of the single-elemental spectra. When the energy-mass spectra are further projected on the mass axis, the mass spectra originate. These serve for evaluation of the mass resolution $\Delta\mathcal{M}/\mathcal{M}$ of the detection system.

The mass resolution is the most important characteristics of the TOF spectrometer as it represents the ability of the TOF-ERDA method to distinguish different elements/isotopes. The better the mass resolution, the thinner the element traces are and more elements can be observed separately. The mass resolution is influenced by numerous effects including the parameters and characteristics of the spectrometer components (detectors, electronics modules), beam properties, experimental setup geometry, and also the combination of the projectile and target ions [4, 29], see the Section 3.1. The theoretical evaluation of $\Delta\mathcal{M}/\mathcal{M}$ is not easy and it is only approximate. The measured mass spectrum allows direct determination of the mass resolution for every single element/isotope with all the contributions included.

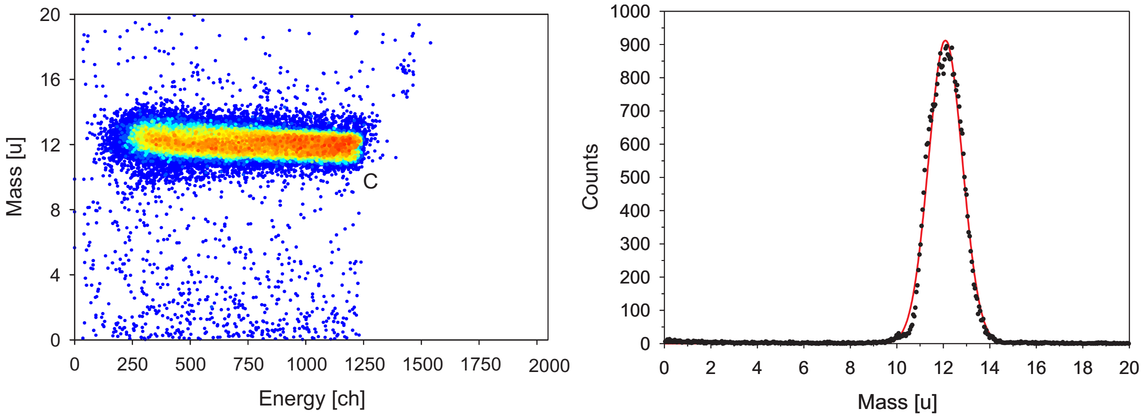

Figure 5.7: The results of analysis of the 2D coincident E-TOF spectrum of the glassy carbon sample. Left: The energy-mass spectrum. Right: The mass spectrum. The ion masses given in the atomic mass units.

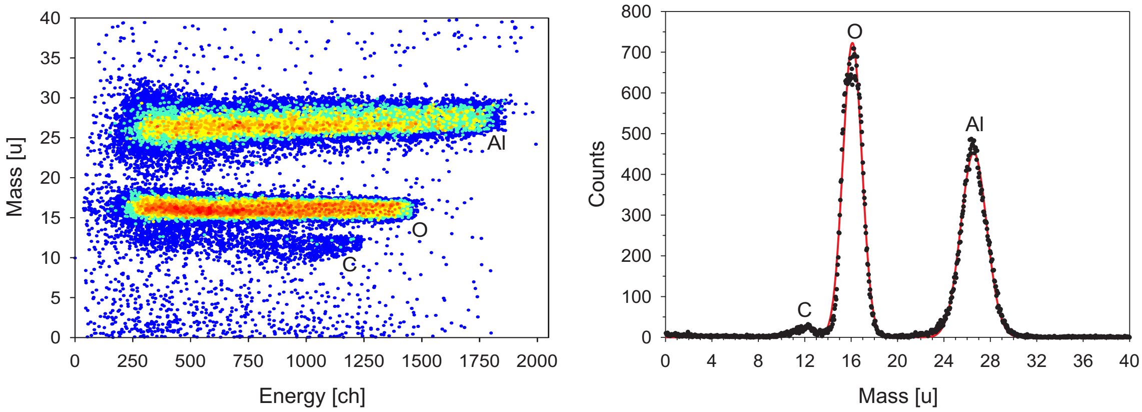

Figure 5.8: The results of analysis of the 2D coincident E-TOF spectrum of the sapphire sample. Left: The energy-mass spectrum. Right: The mass spectrum. The ion masses given in the atomic mass units.

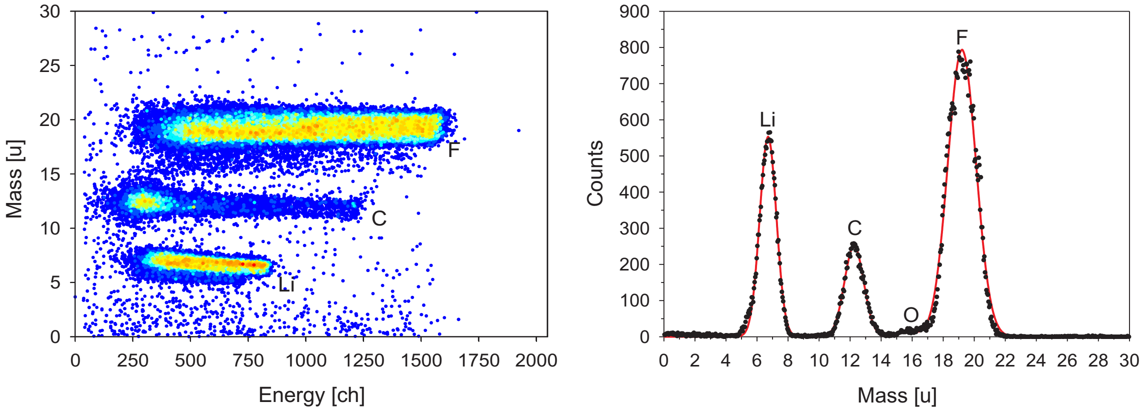

Figure 5.9: The results of analysis of the 2D coincident E-TOF spectrum of the LiF layer on glassy carbon substrate. Left: The energy-mass spectrum. Right: The mass spectrum. The ion masses given in the atomic mass units.

The mass spectrum of each sample was fitted by the sum of Gaussian functions. The fitted parameters and the mass resolution for the elements of interest which are valid for

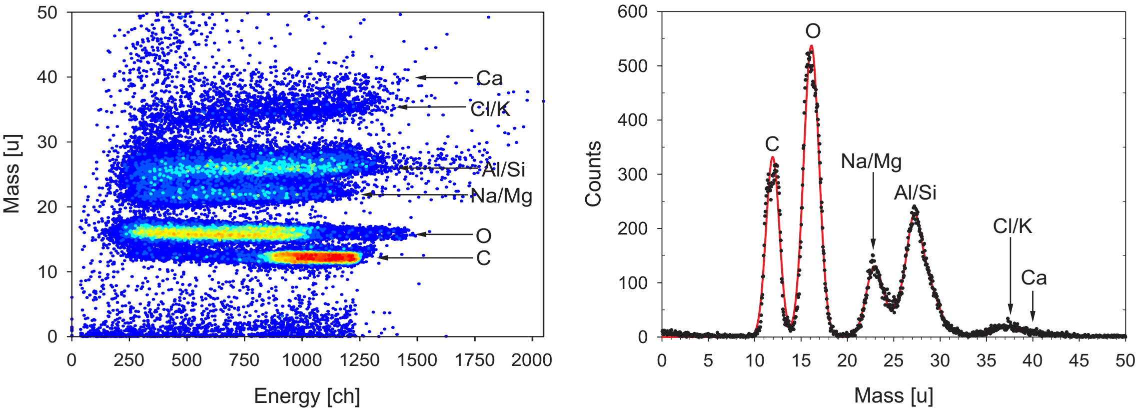

Figure 5.10: The results of analysis of the 2D coincident E-TOF spectrum of the ACF carbon foil on the glass substrate. Left: The energy-mass spectrum. Right: The mass spectrum. The ion masses given in the atomic mass units.

the present TOF telescope setup and 15 MeV Cu ions are listed in the Table 5.4. The first column of this table contains the determined dominant isotope together with its natural abundance and mass (data taken from [49]). The quantities $\mathcal{M}$, $\sigma_{\mathcal{M}}$, $\Delta\mathcal{M}$ and $\Delta\mathcal{M}/\mathcal{M}$ denote the fitted mean isotope mass (centroid of the peak) and its standard deviation, and absolute and relative mass resolutions, respectively. The quantity $\Delta\mathcal{M}$ is taken as the isotope mass peak FWHM. Sample numbers are the following: glassy carbon (1.), sapphire (2.), LiF on glassy carbon (3.) and carbon foil on glass substrate (4.).

Isotope / Abundance / Mass	Sample	$\mathcal{M}$ [u]	$\sigma_{\mathcal{M}}$ [u]	$\Delta\mathcal{M}$ [u]	$\Delta\mathcal{M}/\mathcal{M}$ [%]
^{7}Li / 92.5 % / 7.02 u	3.	6.71 ± 0.01	0.54 ± 0.01	1.26 ± 0.01	18.76 ± 0.14
^{12}C / 98.9 % / 12.00 u	1.	12.09 ± 0.01	0.73 ± 0.01	1.71 ± 0.01	14.14 ± 0.05
	2.	11.92 ± 0.13	0.85 ± 0.13	2.00 ± 0.30	16.81 ± 2.56
	3.	12.26 ± 0.01	0.62 ± 0.01	1.46 ± 0.02	11.95 ± 0.20
	4.	11.94 ± 0.01	0.72 ± 0.01	1.68 ± 0.02	14.10 ± 0.18
^{16}O / 99.8 % / 15.99 u	2.	16.11 ± 0.01	0.82 ± 0.01	1.92 ± 0.01	11.92 ± 0.06
	3.	15.71 ± 0.13	0.53 ± 0.14	1.25 ± 0.33	7.98 ± 2.08
	4.	16.11 ± 0.01	0.83 ± 0.01	1.95 ± 0.01	12.10 ± 0.09
^{19}F / 100.0 % / 19.00 u	3.	19.21 ± 0.01	0.91 ± 0.01	2.14 ± 0.01	11.12 ± 0.05
^{23}Na / 100.0 % / 22.99 u	4.	22.95 ± 0.03	0.94 ± 0.03	2.20 ± 0.07	9.61 ± 0.29
^{27}Al / 100.0 % / 26.98 u	2.	26.57 ± 0.01	1.11 ± 0.01	2.62 ± 0.02	9.87 ± 0.07
^{28}Si / 92.2 % / 27.98 u	4.	27.41 ± 0.02	1.34 ± 0.02	3.16 ± 0.06	11.53 ± 0.21

Table 5.4: The results of the mass spectra analysis.

5.3 Discussion

The previous sections showed that the present TOF-ERDA setup, although without the second time detector and using thicker carbon foil than usual, is able to produce valuable results.

Measurements with the ^{241}Am α-source proved that although the time stop signal is generated by the energy detector which is an order of magnitude slower than the MCP detector, the time resolution of the TOF spectrometer is about 1.6 ns for the

^{241}Am α-particles. The energy resolution of the TOF spectrometer energy detector for the α-particles is about 30 keV FWHM.

Evaluation of the TOF-ERDA spectra is influenced by the factual absence of the suitable analysis software which could evaluate completely the TOF-ERDA spectra. In this regard, the only TOF-ERDA energy spectrum – the sum of energy projections of the single-elemental spectra from the 2D coincident E-TOF spectrum – was analyzed in detail at the moment.

The accessed depths reach from 290 nm for the sapphire sample to 470 nm for the glassy carbon sample. The determined thickness 134 nm of the carbon foil is comparable with the value 110 nm given by the producer. The analyzed piece of carbon foil was exposed to the water for a longer time than the foil used for the time detector front wall. Furthermore, it was stored under the common conditions of the laboratory air (humidity, dust). All these facts could affect the carbon foil properties (thickness, roughness, porosity). Also the thickness of the LiF layer (300 nm) is comparable with the value provided by the producer (200 nm).

The samples mass spectra analysis gives the TOF-spectrometer mass resolution in most cases better than 2 mass units. However, excluding other influences, this characteristics depends mainly on the projectile-target combination and uncertainties in the time and energy measurement. The fitted stoichiometry of the samples is in good agreement with the expected values.

The detection efficiency for the 2D coincident E-TOF spectra taken as the ratio of number of events in the 2D coincident E-TOF spectrum and events in the pure energy spectrum is about 70 %. It is caused by setting of the fast timing amplifier gain (protons produce very weak time signal). As a consequence, signals of elements lighter than Li, i.e. the H signal, are present only in the single energy spectrum but not in the TOF and 2D coincident E-TOF ones. Another measurements of hydrogen-rich samples, which are not published in this work, showed that the region of the hydrogen signal is apparent with the fast timing amplifier gain a factor 3 and more greater than the contemporarily used value. It lies in the TOF interval (500-700) ch and energy interval (50-150) ch at 2048 ch time and energy full-scale ranges. However, the increase of the gain resulted in the significant increase of the background event number.

Conclusion

This master thesis was aimed at development of the nuclear analytical method TOF-ERDA, which is newly available at NPI AS CR, Řež, at the Tandetron accelerator laboratory. It is the extended type of basic ERDA which utilizes the TOF telescope for distinguishing the detected ions. TOF-ERDA provides the non-destructive depth profiling of very thin surface layers composed of elements of almost whole periodic system. Due to the exiguous amount of these elements within the investigated samples, TOF-ERDA together with other IBA methods replaces the conventional non-nuclear analytical methods

The thesis describes development and construction of the TOF telescope preliminary setup. It is equipped with one time and one energy detectors which provide the ion TOF and energy measurement. Although the second time detector is missing, the analysis of real samples proved usability of the device for the TOF-ERDA method.

The whole work on this thesis consists of several steps. The first step included design and production of the time detector and its parts. Excepting purchase of the MCP detector, gold-plated tungsten wire, carbon foils and HV resistors, the detector body, wire harps, supporting structure, vacuum feedthroughs, and time detector completion were made at NPI. The second step was equipment of the TOF telescope with the detectors, electronics and vacuum elements, as well as equipment of the target chamber with the sample holder, sample positioning system, set of slits and chamber monitoring system, all produced at NPI. The final step consisted in design, completion and initialization of the electronics which was crowned by the TOF telescope testing, calibration and successful measurement of the first samples with the consequent TOF-ERDA spectra analysis.

Gaining the important experience with construction and operation of the time detector, future perspectives concerning the TOF telescope are construction of the second time detector and equipment of the both time detectors with carbon foils much thinner than those contemporarily used. These works are planned for the first third of the year 2007.

The steps mentioned above will increase the performance of the telescope in several ways. The fast timing amplifier will be no longer necessary. The time resolution will be well bellow 1 ns, and the total mass resolution much better than one mass unit will be achieved. This will allow to analyze the full 2D coincident E-TOF spectrum or also the separate TOF spectrum instead the energy one as the corresponding resolution of the time measurement is assumed to be better than that of the energy.

Furthermore, a new code for analysis of the TOF-ERDA energy and time spectra is planned to be created during the year 2007. For this purpose, the precise energy and time calibration of the TOF telescope for each element of interest together with possible measurement of certain cross-sections important for the RBS and ERDA which are known with unsatisfactory accuracy will be carried out.

References

[1] S. Rubin *et al.*, Anal. Chem. 29 (1957) 736.

[2] J.R. Tesmer *et al.*, *Handbook of modern ion beam materials analysis*, Material Research Society, Pittsburg, Pennsylvania, 1995.

[3] J. L'Ecuyer *et al.*, J. Appl. Phys. 47 (1976) 381-382.

[4] J. Tirira *et al.*, *Forward recoil spectroscopy: Applications to hydrogen determination in solids*, Plenum Press, New York, 1996.

[5] R. Groleau *et al.*, Nucl. Instr. and Meth. 218 (1983) 11-15.

[6] J.P. Thomas *et al.*, Nucl. Instr. and Meth. 218 (1983) 125-128.

[7] L.C. Feldman, J.W. Mayer, *Fundamentals of surface and thin film analysis*, Elsevier Science Publishing Co., Inc., New York, 1986.

[8] High Voltage Engineering Europa B.V., Particle Accelerator Systems, Amersfoort, The Netherlands, `http://www.highvolteng.com/`.

[9] *Technical Description: Tandetron accelerator systems up to 6.0 MV/TV*, High-Voltage Engineering Documentation No. 1060MT-B-20, Amersfoort, The Netherlands, 2002.

[10] *Model 358 Duoplasmatron ion source*, High-Voltage Engineering Documentation No. A-4-35-090-0002, Amersfoort, The Netherlands, 2002.

[11] D.J.W. Mous *et al.*, Nucl. Instr. and Meth. B 62 (1992) 421-424.

[12] R. Middleton, *A negative ion cookbook*, University of Pennsylvania, Philadelphia, 1989.

[13] R. Middleton, Nucl. Instr. and Meth. 214 (1983) 139-150.

[14] W.-M. Yao *et al.*, J. Phys. G 33 2006. Available at: `http://pdg.lbl.gov/`.

[15] J.F. Ziegler, Rev. Appl. Phys. 85 (1999) 1249-1272.

[16] J.F. Ziegler *et al.*, *SRIM: The stopping and range of ions in matter*, Version SRIM-2003.26. Available at: `http://www.srim.org/`.

[17] F. Besenbacher *et al.*, Nucl. Instr. and Meth. 168 (1980) 1-15.

[18] G. Deconninck, *Introduction to radioanalytical physics*, Akadémiai Kiadó, Budapest, 1978.

[19] C. Tschalär, Nucl. Instr. and Meth. 61 (1968) 141-156.

[20] K.B. Winterbon, Nucl. Instr. and Meth. B 43 (1989) 146-148.

[21] Vakuum Praha spol. s r.o., Prague, Czech Republic, `http://www.vakuum.cz/`.

[22] V. Semián, TOF-ERDA technical documentation, Nuclear Physics Institute, Academy of Sciences, Řež, Czech Republic.

[23] F. Busch *et al.*, Nucl. Instr. and Meth. 171 (1980) 71-74.

[24] J.W. Martin *et al.*, Nucl. Instr. and Meth. B 94 (1994) 277-290.

[25] J. Jokinen *et al.*, Nucl. Instr. and Meth. B 119 (1996) 533-542.

[26] W. Bohne *et al.*, Nucl. Instr. and Meth. B 136-138 (1998) 633-637.

[27] M. Döbeli *et al.*, Nucl. Instr. and Meth. B 142 (1998) 417-424.

[28] H.J. Whitlow *et al.*, Nucl. Instr. and Meth. B 195 (2002) 133-146.

[29] J.K. Kim *et al.*, Nucl. Instr. and Meth. B 140 (1998) 380-388.

[30] A. Razpet *et al.*, Nucl. Instr. and Meth. B 201 (2003) 535-542.

[31] Personal communication: Dr. U. Kreissig, Institute of Ion Beam Physics and Materials Research, Forschungszentrum Dresden-Rossendorf e.V., Germany.

[32] J.O. Stoner, Jr. *et al.*, *ACF-Metals, Product description and technical information*, ACF-Metals, The Arizona Carbon Foil Co., Inc., Tuscon, Arizona, U.S.A., 2005.

[33] K.E. Pferdekämper *et al.*, Z. Physik A 280 (1977) 155-164.

[34] A. Clouvas *et al.*, Phys. Rev. B 43 (1991) 2496-2500.

[35] F. Allegrini *et al.*, Nucl. Instr. and Meth. B 211 (2003) 487-494.

[36] Goodfellow Cambridge Limited, Huntington, England, 2006, `http://www.goodfellow.com/`.

[37] Burle Industries, Inc., *Long-life Micro-Channel Plates*, Lancaster, Philadelphia, U.S.A. Available at: `http://www.burle.com/`.

[38] J.L. Wiza, Nucl. Instr. and Meth. 162 (1979) 587-601.

[39] RS Components Ltd. in representation by Alfatronic s.r.o., Czech Republic, `http://www.rs-components.cz/`.

[40] ORTEC, AMETEK – Advanced Measurement Technology, Inc., Oak Ridge, Tennessee, U.S.A., `http://www.ortec-online.com/`.

[41] Personal communication: Ben Kennedy, Electronics product manager, ORTEC, AMETEK – Advanced Measurement Technology, Inc., Oak Ridge, Tennessee, U.S.A.

[42] National Nuclear Data Center, Brookhaven National Laboratory, Upton, New York, U.S.A, 2006, `http://nndc.bnl.gov/nudat2/`.

[43] Iseg Spezialelektronik GmbH, *NHQ x0xx, Precision NIM High Voltage Supply NHQ STANDARD series*, Radeberg/Rossendorf, Germany. Available at: `http://www.iseg-hv.com/`.

[44] Canberra Industries, Inc., Meriden, Connecticut, U.S.A., `http://www.canberra.com/`.

[45] FAST ComTec Communication Technology GmbH, Oberhaching, Germany, `http://www.fastcomtec.com/`.

[46] M. Mayer, SIMNRA version 6.03, Max-Planck-Institut für Plasmaphysik, Garching, Germany, 2006. Available at: `http://www.rzg.mpg.de/~mam/`.

[47] G.F. Knoll, Radiation detection and measurement, Third edition, John Wiley & Sons, Inc., New York, USA, 2000.

[48] J. Saarilahti, Gisa 3.99, Technical Research Centre, Espoo, Finland, 1994.

[49] R.B. Firestone *et al.*, *WWW Table of Radioactive Isotopes*, Ernest O. Lawrence Berkley National Laboratory, Berkley, USA, 2004. Available at: `http://ie.bnl.gov/toi/`.

[50] W.T. Eadie *et al.*, *Statistical methods in experimental physics*, North-Holland Publishing Company, Amsterdam, 1982.

[51] Maple 6.01, Waterloo Maple Inc., 2000, `http://www.maplesoft.com/`.

Appendix A

Time Detector Electron Optics

The main operation principle of the time detector electron optics is shown in the Figure A.1. Due to magnitudes of potentials applied to equipotential walls, the whole system can be described nonrelativistically. According to the Figure A.1, the carbon foil is kept at the potential U_2 and the accelerating harp at the potential $U_1 > U_2$. The resulting electric field strength between the equipotential walls of the time detector front wall which are located in the mutual distance x_{acc} is:

$$E_{\mathrm{acc}} = \frac{U_1 - U_2}{x_{\mathrm{acc}}} = \frac{U_{\mathrm{acc}}}{x_{\mathrm{acc}}}. \tag{A.1}$$

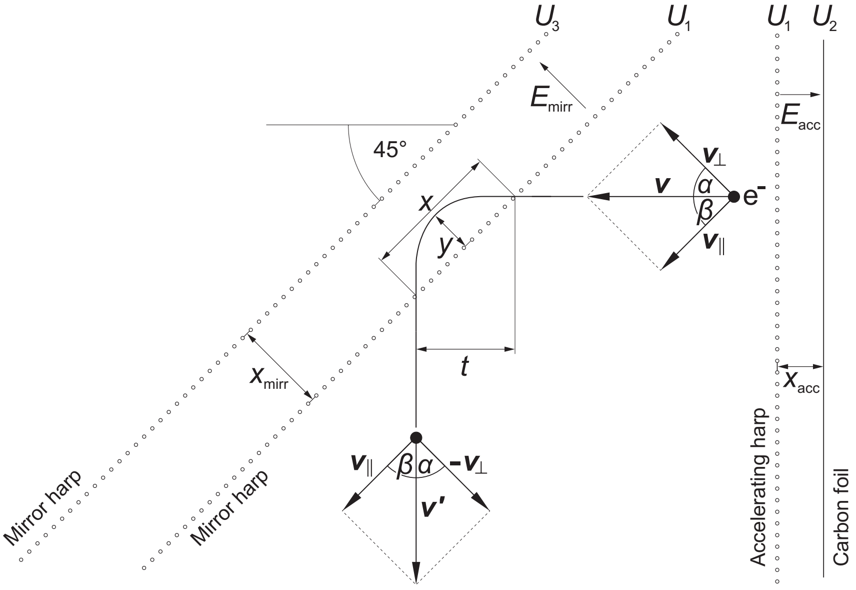

Figure A.1: The principle scheme of the time detector electron optics.

When a secondary electron is knocked out (initial velocity v_0) from the carbon foil into the interior of the time detector front wall by the impact of an incoming ion, the Lorentz force $\vec{F}_{\mathrm{L}}$ acts on this electron which is consequently accelerated by the acceleration $\vec{a}_{\mathrm{acc}}$ towards the accelerating harp:

$$\vec{F}_{\mathrm{L}} = -e\vec{E}_{\mathrm{acc}} = m_{\mathrm{e}}\vec{a}_{\mathrm{acc}} \Rightarrow \vec{a}_{\mathrm{acc}} = -\frac{e}{m_{\mathrm{e}}}\vec{E}_{\mathrm{acc}}. \tag{A.2}$$

During a time t_{acc} spent inside the interior of the front wall, electron gains the velocity $\vec{v}_{\mathrm{acc}}$ in the direction opposite to the electric field $\vec{E}_{\mathrm{acc}}$. When the electron initial velocity v_0 is neglected, for t_{acc} and v_{acc} holds ("|.|" denotes the absolute value):

$$t_{\mathrm{acc}} = \sqrt{\frac{2x_{\mathrm{acc}}}{|a_{\mathrm{acc}}|}} = \sqrt{\frac{2x_{\mathrm{acc}}m_{\mathrm{e}}}{eE_{\mathrm{acc}}}}, \tag{A.3}$$

$$v_{\mathrm{acc}} = |a_{\mathrm{acc}}|t_{\mathrm{acc}} = \sqrt{\frac{2x_{\mathrm{acc}}eE_{\mathrm{acc}}}{m_{\mathrm{e}}}}. \tag{A.4}$$

Entering the field-free region, the electron has the total velocity $\vec{v} \simeq \vec{v}_{\mathrm{acc}}$ ($v_0 \ll v_{\mathrm{acc}}$) and the total kinetic energy approximately eU_{acc}.

To describe the electron path through the electrostatic mirror, the velocity $\vec{v}$ is decomposed to two components – a component perpendicular to the mirror plane $\vec{v}_{\perp}$ and a component parallel with the mirror plane $\vec{v}_{||}$ ($\alpha + \beta = 90°$):

$$v_{\perp} = v\cos\alpha \approx v_{\mathrm{acc}}\cos\alpha, \tag{A.5}$$

$$v_{||} = v\sin\alpha \approx v_{\mathrm{acc}}\sin\alpha. \tag{A.6}$$

When the electron enters the interior of the mirror, the acceleration $\vec{a}_{\mathrm{mirr}}$ in the direction opposite to the mirror electric field $\vec{E}_{\mathrm{mirr}}$ ($U_1 > U_3$) acts on the electron:

$$E_{\mathrm{mirr}} = \frac{U_1 - U_3}{x_{\mathrm{mirr}}} = \frac{U_{\mathrm{mirr}}}{x_{\mathrm{mirr}}} \Rightarrow \vec{a}_{\mathrm{mirr}} = -\frac{e}{m_{\mathrm{e}}}\vec{E}_{\mathrm{mirr}}. \tag{A.7}$$

At the time t_{mirr} the velocity component $v_{\perp}$ is zero and the electron reaches the maximal depth y inside the mirror measured from the entrance mirror harp plane:

$$0 = v_{\perp} - |a_{\mathrm{mirr}}|t_{\mathrm{mirr}} \Rightarrow t_{\mathrm{mirr}} = \frac{v_{\perp}m_{\mathrm{e}}}{eE_{\mathrm{mirr}}}, \tag{A.8}$$

$$y = v_{\perp}t_{\mathrm{mirr}} - \frac{1}{2}|a_{\mathrm{mirr}}|t_{\mathrm{mirr}}^2 \Rightarrow y = \cos^2\alpha\, x_{\mathrm{mirr}}\frac{U_{\mathrm{acc}}}{U_{\mathrm{mirr}}}. \tag{A.9}$$

During the further period t_{mirr}, the electron is accelerated by acceleration $\vec{a}_{\mathrm{mirr}}$ in the direction opposite to the electric field $\vec{E}_{\mathrm{mirr}}$ again. When escaping the mirror, the electron gains velocity $-\vec{v}_{\perp}$ and continues towards the MCP detector through the field-free region. The distances x and t labelled in the Figure A.1 equal the following expressions:

$$x = 2v_{||}t_{\mathrm{mirr}} = 2x_{\mathrm{mirr}}\sin 2\alpha\frac{U_{\mathrm{acc}}}{U_{\mathrm{mirr}}}, \tag{A.10}$$

$$t = x\sin\alpha = 2x_{\mathrm{mirr}}\sin\alpha\sin 2\alpha\frac{U_{\mathrm{acc}}}{U_{\mathrm{mirr}}}. \tag{A.11}$$

The time detector presented in the Section 4.2 is designed in a way that $\alpha = \beta = 45°$. When substituted for α, the following relations for x, y and t are obtained:

$$x = 2x_{\mathrm{mirr}}\frac{U_{\mathrm{acc}}}{U_{\mathrm{mirr}}}, \tag{A.12}$$

$$y = \frac{x_{\mathrm{mirr}}}{2}\frac{U_{\mathrm{acc}}}{U_{\mathrm{mirr}}}, \tag{A.13}$$

$$t = \sqrt{2}x_{\mathrm{mirr}}\frac{U_{\mathrm{acc}}}{U_{\mathrm{mirr}}}. \tag{A.14}$$

Appendix B

ACF Carbon Foil Characteristics

The ACF carbon foil is used as the secondary-electron emitter in the time detector (see the Subsection 4.2.2). Because of its thickness of approximately 20 $\mu\mathrm{g\,cm^{-2}}$ (≈ 100 nm), it changes properties of detected ions which enter the TOF telescope through the time detector. The impact of this foil on ions was studied from the following points of view:

1. the energy straggling of ions with the initial kinetic energy in the range (0.1–10.0) MeV as the consequence of their passage through the foil;
2. the directional straggling of ions with the initial kinetic energy in the range (0.1–10.0) MeV as the consequence of their passage through the foil;
3. the fraction of incoming ions influenced by the directional straggling which can still be detected by the energy detector.

All the effects listed above were studied with the help of SRIM 2003 code [16] in the following way: Ions (10,000 ions per run) with different values of the initial kinetic energy E_0 were let through the carbon foil of the given thickness $t = 100$ nm. For each ion which transmitted the foil (total number denoted as N_{trans}), its remaining energy E' and the coordinates (x, y, z) of its exit point (the entrance point is identical with the coordinate system origin) were recorded, see the Figure B.1.

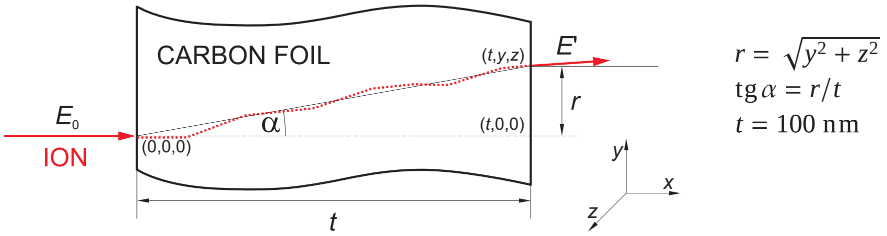

Figure B.1: The evaluation of carbon foil influence on ions.

Both the remaining energy E' and $\mathrm{tg}\,\alpha$ values of the transmitted ions from each run defined in the Figure B.1 were histogrammed to obtain distributions of these quantities. Thanks to the shapes of the remaining energy distribution (difficult treatment of the low-energy tail), the energy E' was converted to the ion energy loss within the foil, $S = E_0 - E'$, which has a meaning of the ion stopping per 100 nm of the foil. After fitting the S distribution by a proper probability density function (PDF) it was converted back to E' distribution.

For fitting these distributions, an attempt to find a suitable functions was done. Finally, the Gamma and Gaussian PDFs were selected. Their shapes do not correspond ideally, but it seems to be a good approach to fit the straggling distributions. The basic properties of the both distributions are listed in the Table B.1. Examples of fitted spectra are shown in the Figure B.2. In practice, the Gaussian PDF was used only for fitting the stopping distributions at higher ion initial energies ($E_0 \geq 1$ MeV) where the influence of the straggling is less significant. For the rest of cases, the Gamma PDF was used.

	Gaussian distribution	Gamma distribution
Probability density function	$f(x;\mu,\sigma) = \frac{1}{\sqrt{2\pi\sigma^2}} \exp\left\{-\frac{(x-\mu)^2}{2\sigma^2}\right\}$	$f(x;k,\theta) = x^{k-1}\frac{e^{-x/\theta}}{\theta^k\Gamma(k)}$ $(x,k,\theta > 0)$
Mean	μ	$k\theta$
Variance	σ^2	$k\theta^2$

Table B.1: The basic properties of the Gaussian and Gamma distributions. Ref. [50].

As mentioned in the Section 3.6, the straggling is expressed as the FWHM of appropriate distribution. When the Gaussian PDF is used for fitting, there is a simple relation between the standard deviation σ and FWHM:

$$\mathrm{FWHM} = \sqrt{4\ln 4}\,\sigma \approx 2.355\,\sigma.$$

For the Gamma distribution no similarly simple formula exists. However, during the simulation data analysis it was found out that when the mean value and standard deviation of the identical distribution is determined from the Gaussian or Gamma PDF parameters, the values of interest differ at most about 30 % in the whole studied energy range, which is sufficient for very rough evaluation. Nevertheless, in the summary Tables B.2–B.4 only the mean values μ and the standard deviations σ for both the energy and directional straggling distributions are summarized.

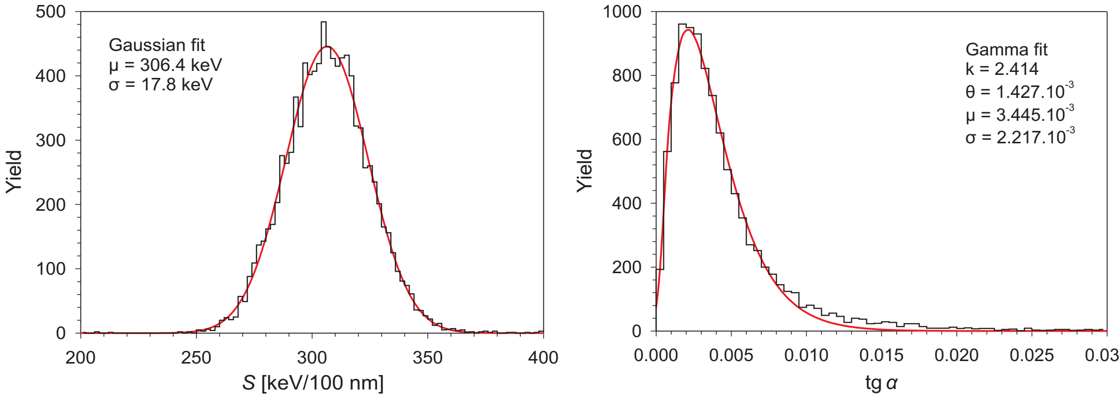

Figure B.2: The energy and directional straggling of 5 MeV Si ions after passing through the time detector carbon foil. Left: The distribution of the ion stopping inside the carbon foil. Right: The directional straggling distribution.

To evaluate a fraction of transmitted ions influenced by the straggling inside the foil, which would still hit the energy detector active area, the tgα distribution was integrated numerically with a help of Maple 6.01 software [51]:

$$\mathcal{I} = \int_0^{\xi} f(x;k,\theta)\,\mathrm{d}x = \int_0^{\xi} \frac{x^{k-1}e^{-x/\theta}}{\theta^k\Gamma(k)}\,\mathrm{d}x$$

Here, k and θ are the fitted Gamma function parameters and $\Gamma(k)$ is the Γ-function. ξ denotes the maximal value of $\operatorname{tg}\alpha$ delimited by red arrows in the Figure below, which is $\xi \approx 18.14 \times 10^{-3}$.

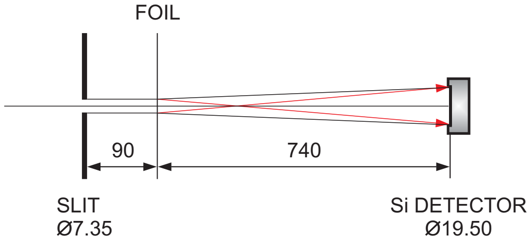

$$\begin{aligned} \xi &= \max(\operatorname{tg}\alpha) = \\ &= \frac{0.50 \times (7.35 + 19.50)}{740.00} \approx \\ &\approx 18.14 \times 10^{-3} \end{aligned}$$

The remaining simulation input parameters are the carbon foil composition: C (94.9 at. %), H (4.0 at. %), O (1.0 at. %) and Na (0.1 at. %), and the foil density: 2.01 g cm^{-3} [32]. All element masses (natural abundance isotope composition) were taken from [14].

Element	E_0 [keV]	N_{trans}	$\mu(\mathrm{E}')$ [keV]	$\sigma(\mathrm{E}')$ [keV]	$\mu(\mathrm{tg}\alpha)$ $\times 1,000$	$\sigma(\mathrm{tg}\alpha)$ $\times 1,000$	$\mathcal{T}$ [%]
H	100	10,000	85.0	1.4	10.27	6.17	89.12
	200	10,000	187.9	1.3	4.76	2.97	99.83
	500	10,000	492.8	1.3	1.93	1.19	100.00
	1,000	10,000	995.3	1.3	0.94	0.58	100.00
	2,000	10,000	1,997.1	1.1	0.47	0.29	100.00
	5,000	10,000	4,998.5	0.8	0.20	0.13	100.00
	10,000	10,000	9,999.2	0.5	0.09	0.06	100.00
He	100	9,998	76.1	2.5	24.87	15.03	0.50
	200	10,000	168.5	2.6	10.37	6.17	2.58
	500	10,000	461.0	2.7	3.45	1.98	17.13
	1,000	10,000	963.1	2.7	1.91	1.17	48.28
	2,000	10,000	1,971.3	2.7	0.92	0.56	87.12
	5,000	10,000	4,983.6	2.7	0.37	0.23	99.95
	10,000	10,000	9,990.2	2.5	0.18	0.12	100.00
Li	100	9,997	75.3	3.7	40.65	26.01	38.55
	200	10,000	167.2	3.8	18.66	11.64	88.93
	500	10,000	447.4	3.9	6.53	4.06	100.00
	1,000	10,000	930.7	4.0	2.85	1.61	100.00
	2,000	10,000	1,929.1	4.1	1.36	0.83	100.00
	5,000	10,000	4,950.2	4.0	0.55	0.35	100.00
	10,000	10,000	9,967.1	4.0	0.27	0.17	100.00
B	100	9,946	57.6	5.8	77.67	49.61	0.37
	200	9,997	150.5	6.5	35.40	22.94	2.26
	500	9,999	428.4	6.3	12.44	7.82	15.48
	1,000	10,000	902.3	6.4	5.82	3.67	46.16
	2,000	10,000	1,883.0	6.7	2.64	1.61	84.95
	5,000	10,000	4,883.9	6.8	0.88	0.48	99.90
	10,000	10,000	9,902.8	6.9	0.37	0.22	100.00
C	100	9,902	55.8	6.0	92.86	60.53	18.72
	200	9,996	145.9	7.5	41.89	26.91	56.45
	500	10,000	421.4	7.7	15.51	9.85	98.47
	1,000	10,000	891.1	7.6	7.29	4.66	100.00
	2,000	10,000	1,861.7	7.9	3.38	2.12	100.00
	5,000	10,000	4,851.4	8.1	1.17	0.70	100.00
	10,000	10,000	9,870.3	8.2	0.50	0.27	100.00
N	100	9,830	51.0	6.6	111.86	72.26	0.40
	200	9,985	142.2	8.3	50.68	33.19	1.95
	500	10,000	417.4	8.8	18.80	12.19	11.91
	1,000	10,000	880.9	8.8	9.18	5.77	40.41
	2,000	10,000	1,844.5	8.9	4.65	3.54	79.69
	5,000	10,000	4,821.6	9.5	1.53	0.92	99.75
	10,000	10,000	9,832.7	9.4	0.64	0.37	100.00
O	100	9,770	52.7	6.9	126.05	82.56	5.41
	200	9,985	141.7	8.1	58.09	37.93	24.11
	500	9,999	421.1	10.0	21.60	14.05	80.00
	1,000	10,000	883.9	10.1	10.63	6.77	99.18
	2,000	10,000	1,832.6	10.4	4.90	3.11	100.00
	5,000	10,000	4,789.1	10.5	1.77	1.10	100.00
	10,000	10,000	9,798.7	10.8	0.77	0.46	100.00
F	100	9,681	53.1	7.7	139.81	91.97	0.44
	200	9,986	142.3	7.8	65.59	42.81	1.61
	500	10,000	413.6	11.1	24.30	15.65	11.47
	1,000	10,000	880.6	11.4	11.69	7.53	35.99
	2,000	10,000	1,826.2	11.5	5.58	3.59	76.77
	5,000	10,000	4,757.9	11.9	2.06	1.32	99.67
	10,000	10,000	9,759.2	12.0	0.93	0.58	100.00
Na	100	9,429	54.4	9.4	158.16	102.16	4.10
	200	9,968	148.5	7.9	80.59	53.31	17.92
	500	10,000	426.4	10.6	29.87	19.34	67.76
	1,000	10,000	891.8	13.7	14.37	9.25	96.96
	2,000	10,000	1,833.4	13.8	6.95	4.55	99.99
	5,000	10,000	4,734.6	14.6	2.59	1.68	100.00
	10,000	10,000	9,694.5	14.3	1.20	0.75	100.00

Table B.2: The SRIM 2003 energy and directional straggling simulation of selected ions with atomic number Z between 1 and 11 as a consequence of the passage through the 100 nm thick time detector carbon foil.

Element	E_0 [keV]	N_{trans}	$\mu(\mathrm{E}')$ [keV]	$\sigma(\mathrm{E}')$ [keV]	$\mu(\mathrm{tg}\,\alpha)$ $\times 1,000$	$\sigma(\mathrm{tg}\,\alpha)$ $\times 1,000$	$\mathcal{I}$ [%]
Mg	100	9,329	52.9	11.1	170.99	110.36	0.46
	200	9,955	151.1	7.7	85.18	55.61	1.43
	500	10,000	428.1	10.3	32.42	20.86	9.85
	1,000	10,000	889.8	14.9	15.69	10.17	32.17
	2,000	10,000	1,827.1	15.3	7.62	4.89	71.57
	5,000	10,000	4,719.6	15.7	2.81	1.78	99.22
	10,000	10,000	9,666.6	15.8	1.35	0.85	100.00
Al	100	8,881	45.1	14.6	180.71	114.65	2.66
	200	9,956	142.0	9.2	93.06	60.25	13.38
	500	9,999	421.4	10.8	35.49	23.05	56.39
	1,000	10,000	888.1	15.0	17.24	11.05	92.19
	2,000	10,000	1,831.5	16.5	8.26	5.30	99.42
	5,000	10,000	4,722.5	16.6	3.24	2.11	100.00
	10,000	10,000	9,651.6	17.0	1.47	0.94	100.00
Si	100	7,566	25.0	16.1	186.60	116.78	0.56
	200	9,909	123.2	11.8	105.45	69.09	1.20
	500	9,999	407.3	12.3	38.81	25.39	8.71
	1,000	10,000	868.1	16.5	18.48	11.86	28.51
	2,000	10,000	1,801.8	17.8	9.04	5.86	67.63
	5,000	10,000	4,693.6	17.8	3.44	2.22	98.63
	10,000	10,000	9,618.4	18.1	1.62	1.03	100.00
P	100	7,323	24.5	18.6	188.37	117.08	2.23
	200	9,876	121.5	12.5	108.63	70.33	10.35
	500	9,998	401.6	13.1	41.76	27.16	48.33
	1,000	10,000	869.7	16.5	19.96	13.24	86.91
	2,000	10,000	1,812.0	19.3	9.70	6.28	99.76
	5,000	10,000	4,707.5	19.4	3.75	2.42	100.00
	10,000	10,000	9,626.7	19.7	1.78	1.17	100.00
S	100	6,128	< 20	–	191.67	116.67	0.50
	200	9,834	119.0	13.6	115.20	74.87	1.20
	500	9,999	400.5	13.3	44.40	29.29	7.92
	1,000	10,000	868.0	17.2	21.59	13.98	27.36
	2,000	10,000	1,809.7	20.5	10.45	6.86	65.05
	5,000	10,000	4,687.2	20.9	3.99	2.56	98.43
	10,000	10,000	9,581.3	20.6	1.94	1.23	100.00
Cl	100	4,106	< 20	–	183.05	106.24	1.85
	200	9,742	101.2	18.5	123.22	80.23	8.22
	500	9,999	400.1	13.3	47.03	30.99	41.53
	1,000	10,000	865.7	16.9	22.46	14.63	82.68
	2,000	10,000	1,805.4	22.0	11.09	7.17	99.31
	5,000	10,000	4,689.6	22.3	4.25	2.78	100.00
	10,000	10,000	9,581.0	21.9	2.04	1.32	100.00
K	100	3,862	< 20	–	186.51	109.95	0.40
	200	9,684	100.6	21.3	131.64	85.59	1.13
	500	9,999	388.2	15.4	53.03	34.28	7.46
	1,000	10,000	865.3	17.4	24.81	15.99	25.39
	2,000	10,000	1,810.7	22.9	12.42	8.05	63.11
	5,000	10,000	4,685.9	24.6	4.79	3.11	97.95
	10,000	10,000	9,566.8	24.4	2.33	1.51	99.99
Ca	100	3,938	< 20	–	193.36	116.31	1.25
	200	9,662	104.3	22.9	135.17	86.08	5.81
	500	10,000	388.9	14.8	55.17	36.13	31.27
	1,000	10,000	861.0	17.7	27.03	17.45	72.09
	2,000	10,000	1,799.1	23.9	13.13	8.63	97.37
	5,000	10,000	4,660.2	25.4	5.04	3.24	100.00
	10,000	10,000	9,537.6	25.9	2.41	1.54	100.00
Ti	100	3,047	< 20	–	188.98	113.40	0.37
	200	9,537	87.8	31.1	141.69	90.05	0.91
	500	9,998	383.8	17.1	60.02	39.33	7.46
	1,000	10,000	872.6	16.4	29.37	19.09	23.45
	2,000	10,000	1,825.5	22.5	14.49	9.45	60.27
	5,000	10,000	4,693.8	28.4	5.57	3.67	97.88
	10,000	10,000	9,559.0	28.7	2.78	1.78	99.99

Table B.3: The SRIM 2003 energy and directional straggling simulation of selected ions with atomic number Z between 12 and 22 as a consequence of the passage through the 100 nm thick time detector carbon foil.

Element	E_0 [keV]	N_{trans}	$\mu(\mathrm{E}')$ [keV]	$\sigma(\mathrm{E}')$ [keV]	$\mu(\mathrm{tg}\,\alpha)$ $\times 1,000$	$\sigma(\mathrm{tg}\,\alpha)$ $\times 1,000$	$\mathcal{I}$ [%]
Cr	100	1,771	< 20	–	177.80	107.38	1.05
	200	9,380	80.0	40.4	146.03	91.34	4.92
	500	9,999	391.7	18.5	64.97	42.90	27.41
	1,000	10,000	881.5	15.7	31.44	20.09	67.07
	2,000	10,000	1,827.0	21.4	15.54	10.07	96.20
	5,000	10,000	4,664.8	30.8	6.14	4.03	100.00
	10,000	10,000	9,512.7	31.6	2.98	1.95	100.00
Mn	100	1,859	< 20	–	184.90	111.48	0.46
	200	9,316	79.2	42.2	148.67	93.60	1.03
	500	9,999	399.1	18.5	68.10	44.90	6.68
	1,000	10,000	881.2	15.8	33.25	22.01	22.84
	2,000	10,000	1,830.3	21.3	16.25	10.63	58.80
	5,000	10,000	4,684.1	32.2	6.38	4.11	97.18
	10,000	10,000	9,526.8	32.6	3.18	2.06	99.98
Fe	100	1,372	< 20	–	184.07	107.98	0.81
	200	9,170	70.6	44.1	151.04	94.80	3.96
	500	9,997	400.9	19.9	69.30	45.35	24.07
	1,000	10,000	887.8	15.7	34.89	23.07	61.48
	2,000	10,000	1,845.2	20.1	16.80	11.05	94.60
	5,000	10,000	4,709.1	33.3	6.62	4.33	99.99
	10,000	10,000	9,534.1	33.8	3.29	2.15	100.00
Co	100	1,383	< 20	–	180.85	104.72	0.36
	200	9,190	68.8	47.2	154.03	94.48	0.95
	500	9,999	402.1	21.6	70.46	46.51	6.02
	1,000	10,000	889.5	16.0	36.36	23.80	21.72
	2,000	10,000	1,854.6	18.8	17.65	11.66	55.92
	5,000	10,000	4,712.2	32.7	6.76	4.34	96.95
	10,000	10,000	9,524.4	34.9	3.36	2.20	99.98
Ni	100	1,718	< 20	–	184.56	110.01	0.67
	200	9,164	70.3	48.0	156.54	98.09	3.24
	500	10,000	406.2	22.1	73.71	48.35	21.09
	1,000	10,000	893.0	16.1	37.06	24.32	57.30
	2,000	10,000	1,888.9	15.5	18.09	11.87	92.18
	5,000	10,000	4,812.9	25.5	7.08	4.61	99.99
	10,000	10,000	9,607.0	35.9	3.54	2.33	100.00
Cu	100	1,143	< 20	–	184.54	107.06	0.38
	200	8,960	56.4	56.2	155.35	95.99	0.77
	500	9,998	399.5	25.5	74.32	47.67	5.65
	1,000	10,000	886.2	18.1	38.46	25.38	20.70
	2,000	10,000	1,849.5	19.4	19.06	12.71	55.15
	5,000	10,000	4,733.3	32.7	7.26	4.67	95.83
	10,000	10,000	9,571.9	37.6	3.61	2.33	99.97
Zn	100	445	< 20	–	169.80	96.82	0.62
	200	8,444	31.7	60.4	155.82	93.85	2.86
	500	9,998	370.5	29.7	76.89	49.39	18.46
	1,000	10,000	858.2	21.6	39.80	26.37	53.20
	2,000	10,000	1,825.3	21.9	19.25	12.64	90.00
	5,000	10,000	4,698.4	35.2	7.66	5.03	99.97
	10,000	10,000	9,534.1	39.1	3.74	2.47	100.00

Table B.4: The SRIM 2003 energy and directional straggling simulation of selected ions with atomic number Z between 24 and 30 as a consequence of the passage through the 100 nm thick time detector carbon foil.